Dissertation

submitted to the

Combined Faculties of the Natural Sciences and Mathematics

of the Ruperto-Carola-University of Heidelberg, Germany

for the degree of

Doctor of Natural Sciences

Put forward by

Xiaona Sun

Born in: Jilin, China

Oral examination: 20.12.2017

Nonthermal Processes of Fast Outflows from Astrophysical Objects

Referees: Prof. Dr. Felix Aharonian
Prof. Dr. Jim Hinton

Zusammenfassung

Plasmaausströmungen sind weitverbreitete Phänomene im Universum, welche sowohl in extragalaktischen wie in galaktischen Objekten häufig beobachtet werden. In dieser Arbeit untersuchen wir drei verschiedene Quellen: Zum Einen analysieren wir Fermi-LAT Daten hochenergetischer Gamma-Emission der großskaligen "Lobes" der Radiogalaxie Centaurus A. Wir verwenden zum ersten Mal die Planck-Beobachtungen, um die Flüsse der "Lobes" abzuleiten. Die spektralen Energieverteilungen über viele Wellenlängenbereiche zeigen einen möglichen lepto+hadronischen Ursprung der nichtthermischen Strahlung. Zum Anderen re-analysieren wir Chandra-Beobachtungen (ingesamt mehr als 1500 Kilosekunden) des Jets aus der Radiogalaxie M87, um dessen Strahlungscharakteristiken im Röntgenbereich näher zu bestimmen. Die Variabilität des Kerngebietes und des inneren Jetknotens HST-1 sowie die Röntgenspektren aller Knoten werden dabei untersucht. Eine Modellierung der spektralen Energieverteilungen (SEDs) vom Radio-zum Röntgenbereich unter der Annahme eines Synchrotron-Ursprungs zeigt, dass ein gebrochenes Potenzgesetz (broken power-law) eine zufriedenstellende Beschreibung dieser SEDs für die meisten Knoten erlaubt, mit Ausnahme der Knoten B, C, und D. Bei letzteren wird eine zusätzliche Emissionskomponente benötigt. Wir diskutieren die Implikationen und schlagen ein stratifiziertes Jetmodell zur Erklärung der Unterschiede vor. Schließlich untersuchen wir die Röntgenemission des jüngsten Supernova-Überrestes (SNR) in unserer Milchstrasse, G1.9+0.3. Wir bestimmen dabei die zugrundeliegende Energieverteilung der Elektronen unter der Annahme einer ausschließlichen Synchrotron-Herkunft der mit Chandra und NuSTAR detektierten Röntgenstrahlung. Ein Vergleich mit der maximalen Beschleunigungsrate an Stoßfronten im nominalen Bohm-Diffusions-Regime zeigt, dass die Beschleunigung der Elektronen in G1.9+0.3 um eine Größenordnung langsamer erfolgt. Wir diskutieren die sich daraus ergebenden Implikationen im Zusammenhang mit dem Beitrag der SNRs zur Galaktischen Kosmischen Strahlung bei PeV-Energien.

Abstract

Outflows are ubiquitous phenomena in the universe. They have been widely observed in both Galactic and extragalactic objects. In this thesis, we analyze three individual sources. Firstly, we re-analyze the high energy γ-ray data of *Fermi*-LAT on the giant lobes of Centaurus A. We utilize for the first time the Planck observations to derive the fluxes of the lobes. The multiwavelength SEDs reveal a possible leptonic+hadronic origin of the non-thermal emission. Secondly, we re-analyze *Chandra* observations of the M87 jet with a total exposure time of 1500 kiloseconds to explore the X-ray emission characteristics along the jet. The variabilities of the nucleus and HST-1, as well as the photon spectra for all knots are investigated. Fitting the radio to X-ray SEDs assuming a synchrotron origin, we show that a broken power-law electron spectrum allows a satisfactory description of the SEDs for most knots except for B, C and D, for which an additional component is needed. We discuss the implications and suggest that a stratified jet model may account for the differences. Finally, we derive the energy distribution of ultrarelativistic electron in G1.9+0.3, which is the youngest known SNR in the Galaxy, under the assumption that the detected X-ray with *Chandra* and NuSTAR are of entirely synchrotron origin. The electron acceleration is found to be an order of magnitude slower than the maximum rate provided by the shock acceleration in the nominal Bohm diffusion regime. We discuss the resultant implications in the context of contribution of SNRs to the Galactic Cosmic Rays at PeV energies.

Contents

List of Figures

List of Tables

1 Introduction

Highly collimated outflows (i.e., jets) and winds are remarkably common phenomena in our universe, and have been widely observed in both Galactic and extragalactic objects. They are generally believed to originate from the accretion processes in active galactic nuclei (AGNs), star-forming regions, and compact binary systems containing compact objects (i.e., white dwarfs, neutron stars, and black holes (Beall, 2015). They also appear to be present in explosive events such as supernovae (SNe) and gamma-ray bursts (GRBs) associated with stellar collapse (Piran, 2000) and in pulsars in the form of e^+e^- wind (Weisskopf et al., 2000a; Pavlov et al., 2003).

The outflow phenomena span a large range of different physical scales in terms of size and energy budget in various classes of astrophysical objects. The jets of young stellar objects (YSOs) only have typical projected lengths of $\leq$ few pcs and luminosities of $(10^3 - 2\times10^4)$ $L_\odot$, emerging from protostars with masses ~ 1 $M_\odot$ (de Gouveia Dal Pino, 2005). While in AGNs, the powerful jets created by supermassive black holes (SMBH) with masses $10^6 - 10^9$ $M_\odot$, have typical sizes of ~ 1 kpc $- 1$ Mpc and luminosities of $\sim 10^9 - 10^{15}$ $L_\odot$. On the other hand, giant radio lobes have been observed in the terminated region of these large scale jets (see, e.g., Blandford & Rees, 1974). Such giant lobes, with the huge volume and enormous energy budget there in, also deserve a detailed study.

The aim of this thesis is to investigate the non-thermal phenomena associated with the astrophysical outflows, in which the large scale (kpc) jet is our prime interest. In this regard M87 is an ideal target to investigate due to its proximity, large angular extension (more than 30″) and high surface brightness. Owing to the accumulative exposure and the recently enhanced software tools of *Chandra*, an improved analysis can now be performed to derive more accurate spectrometric information and to further investigate the radiation mechanism in this region. In this thesis I present the results of a detailed analysis of the *Chandra* data on the M87 nucleus and knots

observed from 2000 to 2016. The giant lobes formed in the termination region of large scale jet also reveal strong non-thermal emission and indicate active particle acceleration process therein. Centaurus A (Cen A), which is the closest radio galaxy, is associated with two giant lobes extending more than 10° (∼ 600 kpc in projection) (Shain, 1958; Burns et al., 1983). It is an unique laboratory to study the spatial and energy distribution of relativistic electrons. Furthermore, by comparing the radio/microwave and γ-ray emissions, we can obtain unambiguous information on the magnetic fields. I present a detailed analysis of the broadband emission of the lobes of Cen A using γ-ray data from *Fermi*-LAT and microwave data from *Planck*.

The relativistic large scale jets are ideal site for particle acceleration but not the only option. The non-relativistic shocks, on the other hand, can also accelerate particles to relativistic energies (see e.g., Blandford & Eichler, 1987). Supernova remnants (SNRs) are believed to be the typical site of shock acceleration (see, e.g., Hillas, 2013; Blasi, 2013). The details of the acceleration in SNRs are still far from being understood. A crucial question is whether such objects can accelerate cosmic ray particles to PeV energy. The X-ray emmission related to the synchrotron radiation of accelerated electrons, namely to the shape of the energy spectrum of radiation in the cutoff region, can serve as a distinct signature of the acceleration mechanism and its efficiency. In this regard, G1.9+0.3, the youngest known SNR in our Galaxy (Reynolds et al., 2008; Green et al., 2008), is a perfect object to explore this unique tool.

This thesis is organized as follows, Chapter 1 is an introduction to the background knowledge, including a brief description of the non-thermal radiation mechanism and particle acceleration processes involved in this study, as well as the introduction to the instruments and corresponding data analysis procedure used in this thesis; in Chapter 2 I present the multiwavelength data analysis results on giant lobes of Cen A; in Chapter 3 I present the detailed *Chandra* data analysis for the large scale jet of M87; in Chapter 4 I derive the relativistic electron spectrum in the young SNR G1.9+0.3 and constrain the acceleration efficiency therein; Chapter 5 is the conclusion.

1.1 Radiation Mechanism

Electromagnetic energy can be emitted when charged particles are accelerated and also during particles decay processes. In astrophysical objects (e.g., AGNs and SNRs), radiative processes from radio to the γ-ray energy band have been studied and described in great detail. In this section, I present the basic concepts and formulae of the synchrotron radiation, inverse compton

(IC) scattering, and pion decay involved in our work, while other high energy radiation mechanism such as electron bremsstrahlung, proton-photon interaction and relativistic electron-photon cascade will be covered briefly.

1.1.1 Synchrotron radiation

Synchrotron is a main nonthermal emission process in astrophysics and occurs when relativistic electrons (or positrons) are centripetally accelerated by a strong magnetic field, and produce high-energy photons. We use the basic formulae reported in the book of Rybicki & Lightman (1986) and references therein.

Synchrotron emission from a single electron
Let's consider the motion of a relativistic electron with mass m_e and charge e. As shown in Figure 1.1, the velocity of the electrons $\mathbf{v}$ has a pitch angle θ with the direction of magnetic field $\mathbf{B}$. The component of velocity $\mathbf{v}_\parallel$ is parallel to $\mathbf{B}$, and the perpendicular component is $\mathbf{v}_\perp$. The electron follows the relativistic equations:

$$\frac{\mathrm{d}}{\mathrm{d}t}(\gamma m_e \mathbf{v}) = \frac{e}{c}\mathbf{v}\times\mathbf{B}, \tag{1.1}$$

$$\frac{\mathrm{d}}{\mathrm{d}t}\left(\gamma m_e c^2\right) = e\mathbf{v}\cdot\mathbf{E}, \tag{1.2}$$

where the last equation equals to zero if we assume zero electric field, in this case we have $\mathrm{d}\gamma/\mathrm{d}t = 0$. Then the first equation follows

$$m_e\gamma\frac{\mathrm{d}\mathbf{v}}{\mathrm{d}t} = \frac{e}{c}\mathbf{v}\times\mathbf{B}. \tag{1.3}$$

Equation 1.3 can be written as:

$$\frac{\mathrm{d}\mathbf{v}_\parallel}{\mathrm{d}t} = 0, \qquad \frac{\mathrm{d}\mathbf{v}_\perp}{\mathrm{d}t} = \frac{e}{\gamma m_e c}\mathbf{v}_\perp\times\mathbf{B}, \tag{1.4}$$

from which we see immediately $\mathbf{v}_\parallel$ is constant, $|\mathbf{v}|$ is constant, so $|\mathbf{v}_\perp|$ = constant. The magnetic force is zero for motion parallel to the field. Thus, the electron spirals around the magnetic field lines forming a helical motion with frequency

$$\nu_\mathrm{B} = \frac{e\mathbf{B}}{2\pi\gamma m_e c} = \frac{\nu_\mathrm{L}}{\gamma}, \tag{1.5}$$

where $\nu_\mathrm{L} = \frac{eB}{2\pi m_e c}\sin\theta = 2.8\times10^6\left(\frac{B}{1\mathrm{G}}\right)\sin\theta$ Hz is the *Larmor frequency*. The *Larmor radius* of the circular motion perpendicular to the magnetic field is

$$r_\mathrm{L} = \frac{m_e c^2}{\mathrm{e}B}\gamma\beta\sin\theta = 1.71\times10^3\gamma B^{-1}(G)\sin\theta\,\mathrm{cm}. \tag{1.6}$$

Here $\beta = \frac{\mathrm{v}}{\mathrm{c}}$, so the Lorentz factor $\gamma = \frac{1}{\sqrt{1-v^2/c^2}} = \frac{1}{\sqrt{1-\beta^2}}$. According to the Larmor formula, the total emitted power is

$$P = \frac{\mathrm{d}W}{\mathrm{d}t} = \frac{2}{3} r_0^2 c \beta^2 \gamma^2 B^2 \sin^2\theta, \tag{1.7}$$

where $r_0 = \frac{e^2}{m_e c^2}$ (in cgs units) is called the classical electron radius and has a value of 2.8×10^{-13} cm. The single electron emitted power averaged over an isotropic distribution of pitch angles becomes

$$P_{\rm iso} = \frac{4}{3}\sigma_{\rm T} c \beta^2 \gamma^2 U_{\rm B} \sim 2.5 \times 10^{-14} \left(\frac{U_{\rm B}}{1 {\rm erg/cm^3}}\right) \gamma^2 \ {\rm erg/s}. \tag{1.8}$$

Here $\sigma_{\rm T} = 8\pi r_0^2/3$ is the Thomson cross section.

$$U_{\rm B} = \frac{B^2}{8\pi} = \frac{10^{-12}}{8\pi} \times \left(\frac{B}{1\mu{\rm G}}\right)^2 {\rm erg/cm^3} = 0.025 \left(\frac{\rm B}{1\mu{\rm G}}\right)^2 {\rm eV/cm^3} \tag{1.9}$$

is the energy density of the magnetic field.

Because of the beaming effect, the observer will see a pulse of radiation confined in a time interval smaller than the Larmor period $(1/\nu_{\rm L})$, hence, the spectrum will spread on a much larger range of frequencies than one order of $\nu_{\rm B}$. In this case, the emitted synchrotron radiation power per unit frequency interval, as a function of frequency ν of the emitted photon, is given by

$$\frac{\mathrm{d}P}{\mathrm{d}\nu} = \frac{\sqrt{3} e^3 B \sin\theta}{m_e c^2} F\left(\frac{\nu}{\nu_c}\right). \tag{1.10}$$

Here ν_c is the synchrotron critical frequency and expressed by

$$\nu_c = \frac{3}{2}\gamma^2 \nu_{\rm L} \sin\theta = 4.2 \left(\frac{B}{1\mu{\rm G}}\right) \gamma^2 \sin\theta \ {\rm Hz}. \tag{1.11}$$

The nondimensional synchrotron spectrum $F\left(\frac{\nu}{\nu_c}\right)$ is defined as

$$F\left(\frac{\nu}{\nu_c}\right) = \left(\frac{\nu}{\nu_c}\right) \int_{\nu/\nu_c}^{\infty} K_{5/3}(x) dx, \tag{1.12}$$

where $K_{5/3}$ is the modified Bessel function of order 5/3. To avoid using the special functions and improve the efficiency of the analytical integration, Aharonian et al. (2010) provide a parametrization of the emissivity function for synchrotron radiation in random magnetic fields:

$$\frac{\mathrm{d}P}{\mathrm{d}\nu} \simeq \frac{\sqrt{3} e^3 B \sin\theta}{m_e c^2} \frac{1.808 x^{1/3}}{\sqrt{1+3.4x^{2/3}}} \frac{1+2.21x^{2/3}+0.347x^{4/3}}{1+1.353x^{2/3}+0.217x^{4/3}} e^{-x}, \tag{1.13}$$

where $x = \frac{\nu}{\nu_c}$. This practical approximation achieves an accuracy better than 0.2% over the entire range of emission energy, and has been applied in our

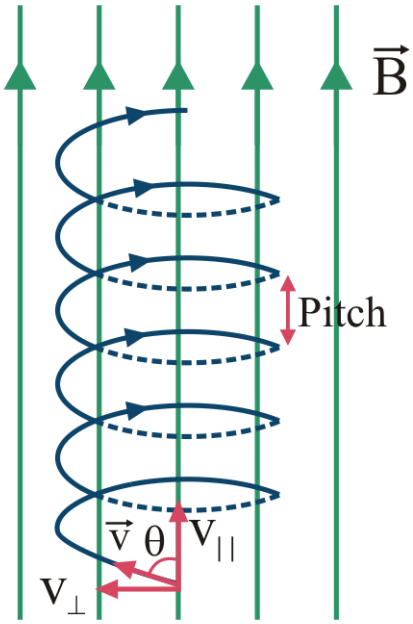

Figure 1.1: An electron spirals around the magnetic field lines forming a helical trajectory. Image taken from http://www.actucation.com/college-physics-2/presence-of-only-magnetic-field.

synchrotron calculations. The frequency at maximum synchrotron emission is

$$\nu_m \simeq 0.29\nu_c = 1.22\left(\frac{B}{1\mu\mathrm{G}}\right)\gamma^2 \sin\theta\,\mathrm{Hz}. \tag{1.14}$$

The cooling time for the single electron is

$$t_c = \frac{E}{P} = \frac{\gamma m_e c^2}{P} \propto \frac{1}{\gamma}. \tag{1.15}$$

In many astrophysical calculations, we generally consider the case that the synchrotron emission comes from an isotropic electrons population with a distribution $N(\gamma)$ which represents the number density of electrons per unit of volume and energy. In this case, the synchrotron emissivity, namely, the total power radiated per unit volume per unit frequency is calculated as

$$j_s(\nu) = \frac{1}{4\pi}\int_{\gamma_{\min}}^{\gamma_{\max}} \frac{\mathrm{d}P}{\mathrm{d}\nu} N(\gamma)\, d\gamma. \tag{1.16}$$

1.1.2 Inverse Compton scattering

One of the major γ-ray production mechanisms in different astrophysical environments is inverse compton (IC) scattering. The IC scattering is a pro-

cess in which the low energy photons are up-scattered to higher energies through collisions with relativistic particles, so that the scattered photons gain energy from the relativistic particles (Blumenthal & Gould, 1970; Rybicki & Lightman, 1979). The relativistic particles usually refer to the electrons. In the rest system of a relativistic electron with Lorentz factor γ, a photon of energy $h\nu$ will appear to be moving with an energy of $\gamma h\nu$.

If the photon energy $\gamma h\nu \ll m_e c^2$:
photons gain energy from relativistic electrons. The electrons lose less part of energy after one time scattering. This is the classical case of Thomson scattering, and the incident photons are approximated as a continuous electromagnetic wave. The cross sections of the scattering is the Thomson cross section σ_T,

$$\sigma_T = \frac{8\pi}{3} r_0^2 = 6.65 \times 10^{-25} \mathrm{cm}^2. \tag{1.17}$$

Based on the conservations of energy and momentum, the frequencies of the photons ν_i and ν are related by

$$\nu = \frac{\nu_\mathrm{i}}{1 + \frac{h\nu_\mathrm{i}}{mc^2}(1 - \cos\theta)}. \tag{1.18}$$

In the observer's frame, the minimum frequency that a photon can acquire is

$$\nu = \frac{\nu_\mathrm{i}}{4\gamma^2}, \tag{1.19}$$

the maximum frequency is

$$\nu = 4\gamma^2 \nu_\mathrm{i}. \tag{1.20}$$

and the mean frequency of the up-scattered photons is

$$< \nu >= \frac{4}{3}\gamma^2 \nu_\mathrm{i} \rightarrow \gamma = \left(\frac{3\nu}{4\nu_\mathrm{i}}\right)^{1/2}. \tag{1.21}$$

The total IC power for an electron in an isotropic distribution of photons is given by

$$P_\mathrm{compt} = \frac{dE_\mathrm{rad}}{dt} = \frac{4}{3}\sigma_\mathrm{T} c \beta^2 \gamma^2 U_\mathrm{ph} \sim 2.6 \times 10^{-14} \left(\frac{U_\mathrm{ph}}{1 \mathrm{erg/cm}^3}\right) \gamma^2 \ (\mathrm{erg/s}), \tag{1.22}$$

where U_ph is the energy density of the radiation before scattering. The cooling time due to the IC process is

$$t_\mathrm{c} = \frac{\gamma \mathrm{m_e c}^2}{P_\mathrm{compt}} \simeq 3 \times 10^7 / (U_\mathrm{ph} \gamma) \ \mathrm{s}. \tag{1.23}$$

Comparing Equation 1.8 with Equation 1.22, we can find that the ratio between the power emitted through synchrotron and IC is given by

$$\frac{P_\mathrm{synch}}{P_\mathrm{compt}} = \frac{U_\mathrm{B}}{U_\mathrm{ph}}. \tag{1.24}$$

If the photon energy $\gamma h\nu \geq m_e c^2$:
photons gain energy from relativistic electrons. In this situation, quantum effects related to the interaction between electrons and photons must be considered. Quantum effects appear in two ways: first, through the kinematics of the scattering mechanism and then, through the modification of the cross section. The scattering will be no longer elastic because of the recoil of the electron.

Accurate formula or the approximate expression of the IC photon spectrum have been given in several works, e.g., by Jones (1968) and Ryder (1996). In this thesis, we select the approximation for the IC photon spectrum calculation in Aharonian & Atoyan (1981), and Khangulyan et al. (2014). In the case of isotropically distributed relativistic electrons, the computation of IC spectrum for nonthermal seed photon fields is

$$\frac{\mathrm{d}N(\omega)}{\mathrm{d}\omega} = \frac{2\pi r_0^2}{\omega_0 E^2}\left[1 + \frac{\mathrm{z}^2}{2(1-\mathrm{z})} + \frac{\mathrm{z}}{\mathrm{b}(1-\mathrm{z})} - \frac{2\mathrm{z}^2}{\mathrm{b}^2(1-\mathrm{z})^2} - \frac{z^3}{2b(1-z)^2} - \frac{2z}{b(1-z)}\ln\frac{b(1-z)}{z}\right], \tag{1.25}$$

where E, ω_0, and ω are the energies of electron, seed photon, and upscattered photon, respectively; $\mathrm{b} = 4\omega_0 E$, $\mathrm{z} = \omega/\mathrm{E}$, $\frac{\omega_0}{E} \ll z \leq \frac{\mathrm{b}}{1+\mathrm{b}} = \frac{\omega_M}{E}$.

If the seed photons for the IC scattering are dominated by black (or grey) body radiation, the IC radiation spectrum for anisotropic interaction is given by

$$\frac{\mathrm{d}N_{\mathrm{ani}}}{\mathrm{d}\omega dt} = \frac{2r_0^2 m_e^3 c^4 \kappa T^2}{\pi\hbar^3 E^2} \times \left[\frac{z^2}{2(1-z)}F_1(x_0) + F_2(x_0)\right], \tag{1.26}$$

where $x_0 = \frac{z}{(1-z)t_\theta}$, $t_\theta = 2ET(1-\cos\theta)$. θ is the initial angle between the relativistic electron and seed photon. T is the seed photon temperature. κ is the dilution factor in the case of grey-body radiation. The functions F_1 and F_2 have the following approximated forms (i=1 or 2):

$$F_i \simeq \left(\frac{\pi^2}{6} + x_0\right)e^{-x_0} \times \left[1 + \frac{a_i x_0^{\alpha_i}}{1 + b_i x_0^{\beta_i}}\right]^{-1} \tag{1.27}$$

with the values:
$a_1 = 0.153, b_1 = 0.254, \alpha_1 = 0.857, \beta_1 = 1.84,$
$a_2 = 1.33, b_2 = 0.534, \alpha_2 = 0.691, \beta_2 = 1.668.$

The IC radiation spectrum for isotropic interaction with a blackbody photon spectrum becomes

$$\frac{\mathrm{d}N_{\rm iso}}{\mathrm{d}\omega dt} = \frac{2r_0^2 m_e^3 c^4 \kappa T^2}{\pi\hbar^3 E^2} \times \left[\frac{z^2}{2(1-z)} F_3(x_0) + F_4(x_0)\right], \tag{1.28}$$

where $x_0 = \frac{z}{(1-z)t}$, $t = 4ET$.
F_3 and F_4 have the following approximations (i=3 or 4):

$$F_i \simeq \frac{\pi^2}{6} \frac{1 + c_i x_0}{1 + \frac{\pi^2 c_i}{6} x_0} e^{-x_0} \times \left[1 + \frac{a_i x_0^{\alpha_i}}{1 + b_i x_0^{\beta_i}}\right]^{-1}, \tag{1.29}$$

with the values:
$a_3 = 0.443, b_3 = 0.54, c_3 = 0.319, \alpha_3 = 0.606, \beta_3 = 1.481,$
$a_4 = 0.726, b_4 = 0.382, c_4 = 6.62, \alpha_4 = 0.461, \beta_4 = 1.457.$

1.1.3 Pion decay

The main high energy γ-ray production channel for relativistic protons are p-p inelastic interactions followed by pion decay, the process for the decay of π^0 mesons into two γ-rays is

$$p + p \rightarrow \pi^0 + X \rightarrow \gamma\gamma + X. \tag{1.30}$$

Here, X represents minor secondary particles. The threshold kinetic energy for a proton to produce a π^0 is given by

$$T_p^{\rm th} = 2m_\pi + m_\pi^2/2m_p \approx 0.28\mathrm{GeV}. \tag{1.31}$$

In natural units (i.e. $\hbar = c = k_B = 1$), $m_p = 0.938272046$ GeV and $m_\pi = 0.1349766$ GeV are the proton and π^0 masses, respectively. At rest, a π^0 will decay to produce a photon with energy $E_\gamma = \frac{1}{2} m_\pi \approx 68$MeV.

By considering public Monte Carlo results and a compilation of published data on p-p interactions from the kinematic threshold to PeV energies, Kafexhiu et al. (2014) developed analytic parametrizations for the p-p total inelastic cross section and the γ differential cross section. The parametrization formula for the p-p total inelastic cross section is

$$\sigma_{\rm inel} = \left[30.7 - 0.96 \log\left(\frac{T_p}{T_p^{\rm th}}\right) + 0.18 \log^2\left(\frac{T_p}{T_p^{\rm th}}\right)\right] \times \left[1 - \left(\frac{T_p^{\rm th}}{T_p}\right)^{1.9}\right]^3 \mathrm{mb}. \tag{1.32}$$

Here, T_p is the proton kinetic energy in the laboratory frame. The parametrization of the γ-ray differential cross section is given by

$$\frac{d\sigma}{dE_\gamma}\left(T_p, E_\gamma\right) = A_{\rm max}(T_p) \times F(T_p, E_\gamma), \tag{1.33}$$

where $A_{\rm max}(T_p)$ is the maximum value of $d\sigma/dE_\gamma$ which is a function of the proton energy T_p. $A_{\rm max}$ is expressed as follows

$$\begin{aligned} A_{\rm max}(T_p) =& b_0 \times \frac{\sigma_\pi(T_p)}{E_\pi^{\rm max}} : \text{ for } T_p^{\rm th} \leq T_p < 1 \text{ GeV}, \\ A_{\rm max}(T_p) =& b_1\, \theta_p^{-b_2}\, \exp\left(b_3\, \log^2(\theta_p)\right) \times \frac{\sigma_\pi(T_p)}{m_p} \\ & : \text{ for } T_p \geq 1 \text{ GeV}, \end{aligned} \tag{1.34}$$

where, $\theta_p = T_p/m_p$, $E_\pi^{\rm max}$ is the maximum total π^0 energy in the laboratory frame, and $\sigma_\pi(T_p)$ is the inclusive π^0 production cross section. Both $E_\pi^{\rm max}$ and $\sigma_\pi(T_p)$ are functions of the proton energy T_p, details are presented in Equation (10) and Section II in Kafexhiu et al. (2014). $b_0 = 5.9$, and $b_1 - b_3$ are given in Table 1.1. $F(T_p, E_\gamma)$ describes the shape of the spectrum and depends on the proton energy T_p and γ-ray energy E_γ,

$$F(T_p, E_\gamma) = \frac{\left(1 - X_\gamma^{\alpha(T_p)}\right)^{\beta(T_p)}}{\left(1 + \frac{X_\gamma}{C}\right)^{\gamma(T_p)}}\,, \tag{1.35}$$

where X_γ and C are defined as follows:

$$\begin{aligned} Y_\gamma =& E_\gamma + \frac{m_\pi^2}{4\,E_\gamma}, \quad Y_\gamma^{\rm max} = E_\gamma^{\rm max} + \frac{m_\pi^2}{4\,E_\gamma^{\rm max}}, \\ X_\gamma =& \frac{Y_\gamma - m_\pi}{Y_\gamma^{\rm max} - m_\pi}, \quad C = \lambda \times m_\pi / Y_\gamma^{\rm max}. \end{aligned} \tag{1.36}$$

Table 1.2 lists the values of λ, $\alpha(T_p)$, $\beta(T_p)$ and $\gamma(T_p)$ for different energies and models.

The γ-ray spectrum produced through p-p interactions with a distribution

Table 1.1: Coefficients $b_1 - b_3$ in eq. (1.34) for Geant 4.10.0, Pythia 8.18, SIBYLL 2.1 and QGSJET-I.

Model	Energy range	b_1	b_2	b_3
Geant 4	$1 \leq T_p < 5$ GeV	9.53	0.52	0.054
Geant 4	$T_p \geq 5$ GeV	9.13	0.35	9.7e-3
Pythia 8	$T_p > 50$ GeV	9.06	0.3795	0.01105
SIBYLL	$T_p > 100$ GeV	10.77	0.412	0.01264
QGSJET	$T_p > 100$ GeV	13.16	0.4419	0.01439

of protons $N(T_p)$ is

$$J_\gamma(E_\gamma) = 4\pi n_{\rm H} \int \frac{d\sigma}{dE_\gamma}(T_p, E_\gamma) N(T_p) dT_p, \tag{1.37}$$

where $n_{\rm H}$ is the density of target protons.

In fact, elements heavier than hydrogen are found in many astrophysical environments. Although the abundances of these elements are small, we shouldn't ignore the γ-ray contribution in their nucleus-nucleus interactions. To correct the γ-ray spectrum for heavier nuclei interactions, the nuclear enhancement factor (ϵ) is expressed as

$$\epsilon(T_p) = 1.37 + 0.39 \times \frac{\sigma_R^{pp} \times \mathcal{G}(T_p)}{\sigma_{\rm inel}(T_p)}. \tag{1.38}$$

Here, $\mathcal{G}(T_p)$ is given by

$$\mathcal{G}(T_p) = 1 + \log\left(\max\left[1, \frac{\sigma_{\rm inel}(T_p)}{\sigma_{\rm inel}(T_p^0)}\right]\right). \tag{1.39}$$

$\sigma_R^{pp} = \pi r_p^2 = 10\pi$ mb is the proton geometrical cross section. $\sigma_{\rm inel}(T_p)$ is the p-p total inelastic cross section given in Equation 1.32. $T_p^0 = 10^3$ GeV. Then the corrected γ-ray spectrum is $\epsilon J_\gamma(E_\gamma)$.

Table 1.2: Functions $\alpha(T_p)$, $\beta(T_p)$, $\gamma(T_p)$ and λ coefficients in eq. (1.35) for Geant 4.10.0, Pythia 8.18, SIBYLL 2.1 and QGSJET-I. Functions $\kappa(T_p) = 3.29 - \frac{1}{5}\,\theta_p^{-3/2}$ and $\mu(T_p) = \frac{5}{4}\,q^{\frac{5}{4}}\,\exp\left(-\frac{5}{4}\,q\right)$, respectively, where $\theta_p = T_p/m_p$.

Model	Energy [GeV]	λ	$\alpha(T_p)$	$\beta(T_p)$	$\gamma(T_p)$
Exp. Data	$T_p^{\rm th} \le T_p \le 1$	–	1.0	κ	0
Geant 4	$1 < T_p \le 4$	3.00	1.0	$\mu + 2.45$	$\mu + 1.45$
Geant 4	$4 < T_p \le 20$	3.00	1.0	$\frac{3}{2}\mu + 4.95$	$\mu + 1.50$
Geant 4	$20 < T_p \le 100$	3.00	0.5	4.2	1
Geant 4	$T_p > 100$	3.00	0.5	4.9	1
Pythia 8	$T_p > 50$	3.50	0.5	4.0	1
SIBYLL 2.1	$T_p > 100$	3.55	0.5	3.6	1
QGSJET-I	$T_p > 100$	3.55	0.5	4.5	1

1.1.4 Electron bremsstrahlung

Comprehensive analysis of features of the cross-sections of bremsstrahlung can be found in Heitler (1954).

The lifetime of electrons due to the bremsstrahlung can be expressed as

$$t_{\rm br} = \frac{E_e}{-dE_e/dt} \sim 4 \times 10^7 (n/1{\rm cm}^{-3})^{-1}{\rm yr}, \tag{1.40}$$

where n is the number density of the ambient gas. We note that the lifetime given by Eq. 1.40 is energy independent. This implies that the bremsstrahlung losses will not change the injected electron spectrum. Thus steady state of electrons $N(E)$ should have the same shape as the injected spectrum

$Q(E)$. The spectrum of bremsstrahlung γ-rays is also power-law with the same power-law index. But in reality we note ionization dominates over the bremsstrahlung below 350 MeV. In fact both the ionization and bremsstrahlung loss rates are proportional to n, thus this condition is independent the ambient gas density. In this case the the steady-state electron spectrum becomes flatter. In the case of a power-law injection spectrum $Q(E) \sim E^{-\Gamma}$, the steady state spectrum will be $N(E) \sim E^{-\Gamma+1}$, thus the bremsstralung γ-ray should also have a very hard spectrum $N(E) \sim E^{-\Gamma+1}$ below several hundred MeV. In many astrophysical scenarios the inverse Compton and synchrotron losses may well dominate over bremsstrahlung, especially at very high energies. In this case $N(E) \sim E^{-\Gamma-1}$ since the lifetime due to synchrotron and inverse Compton loss are inversely proportional to the electron energy.

1.1.5 Proton-gamma interaction

The main processes of proton (hadron)-photon interactions include (i) inverse Compton scattering: $p + \gamma \rightarrow p + \gamma'$, (ii) electron-positron pair production: $p + \gamma \rightarrow p + e^+e^-$, (iii) photodisintegration of nuclei: $A + \gamma \rightarrow A' + kN$, (iv) photomeson production: $N + \gamma \rightarrow N + \pi$. Where A is the nucleus and N is nucleon. In extremely dense radiation fields the secondary $\pi^{\pm}$ mesons may effectively interact with photons before they decay. Except for the inverse Compton scattering, all other processes take place only above certain kinematic thresholds: $\sim$ 1 MeV, 10 MeV, and 140 MeV (in the rest frame of projectile particles) for the pair production, photodisintegration, and pion production, respectively. The process of inverse Compton scattering of protons is identical to the inverse Compton scattering of electrons, but the energy loss rate of protons is suppressed, for the fixed energy of both particles, by a factor of $(m_e/m_{\rm p})^4 \sim 10^{-13}$. Thus this process is always negligible in astrophysical processes.

For pair production, in each interaction only a small fraction of the proton energy is transferred to the secondary electrons (Blumenthal, 1970). Therefore the energy loss rate of protons remains relatively slow. Moreover, the energy region where this process dominates is quite narrow. It is limited by the energy interval of protons $\sim (1-100) \times 10^{15} (\omega_0/1eV)^{-1}$ eV, (ω_0 is the average energy of target photons). When the proton energy exceeds the pion production threshold, the hadronic photomeson interactions well dominate over the pair production (see e.g., Berezinskii & Grigor'eva, 1988; Geddes et al., 1996).

The photodisintegration of nuclei may be important in the formation of the chemical composition of very high energy cosmic rays in both the compact astrophysical objects (Karakula & Tkaczyk, 1993) and the intergalactic

medium (see e.g., Stecker, 1998). But high energy γ-rays cannot be produced in this process.

Photomeson production is the most efficient mechanism to transfer of the kinetic energy of protons into high energy γ-rays. Close to the energy threshold, the process proceeds through single-pion production, while at higher energies, multi-pion production channels begin to dominate. Atoyan & Dermer (2003) suggested a simple approach for approximation of the pion production cross-sections by the sum of two step-functions $\sigma_1(E)$ and $\sigma_2(E)$ for the single-pion and multi-pion channels respectively, with $\sigma_1 = 340\ \mu$b for 200 MeV $\leq$ E$_\gamma$ $\leq$ 500 MeV and $\sigma_2 = 120\ \mu$b for $E \geq 500$ MeV. The inelasticities in these two energy intervals are approximated by $f_{p\gamma} = 0.2$ and 0.6, respectively. Finally, applying the δ-function approximation to calculations of the spectra of secondary particles (assuming $E_\gamma \sim 0.1E_p$ with 2 photons per π^0-decay, and $E_{\gamma,\nu} \sim 0.05E_{\rm p}$, with 1 electron and 3 neutrinos produced in every charged pion decay), this simple approach is accurate enough to calculate the energy spectra and production rate of secondaries.

The cross-sections of interactions of secondary electrons and γ-rays with the ambient photons exceed the photomeson cross-sections by three orders of magnitude. Therefore the electrons and γ-rays cannot leave the source region, but rather initiate electromagnetic cascades in the surrounding photon and magnetic fields. The standard spectra of the low-energy cascade γ-rays that eventually escape the source are not sensitive to the parent spectral distributions, and thus contain information only about the total hadronic power of the source. On the other hand the secondary neutrinos freely escape the production region, and thus carry direct information about the energy spectra of accelerated protons.

1.1.6 Relativistic electron-photon cascades

Relativistic electrons can produce γ-rays in different astrophysical environments with high efficiency through bremsstrahlung, inverse Compton scattering and synchrotron (and/or curvature) radiation, respectively. Each of these γ-rays production mechanisms has its major "counterpart" - a γ-rays absorption mechanism of the same electromagnetic origin - resulting in e^--e^+ pair production in matter (the counterpart of bremsstrahlung), in photon gas (the counterpart of inverse Compton scattering), and in a magnetic field (the counterpart of synchrotron radiation). In many astrophysical scenarios, in particular in compact galactic and extragalactic objects with favourable conditions for particle acceleration, the internal γ-ray absorption becomes unavoidable. If the γ-ray production and absorption is processed in relativistic regimes the problem cannot be reduced to a simple absorption effect.

The secondary electrons produce a new generation of high energy γ-ray, and these photons again produce e^-e^+ pairs, so an electromagnetic cascade develops. Thus according to the γ-ray production and absorption mechanism, the electromagnetic cascades can be investigated in three different scenarios, that is, in matter, in photon fields and in magnetic field.

The theory of electromagnetic cascades in matter can be applied to the interaction cosmic rays with the Earth's atmosphere (see e.g., Rossi & Greisen, 1941; Nishimura, 1969; Ivanenko, 1968), as well as some sources of high energy cosmic radiation, in particular to the "hidden source" scenarios like massive black holes in centers of AGN or young pulsars inside the dense shells of recent supernovae explosions (see e.g., Berezinskii et al., 1990). Also, within the so-called "beam dump" models (see e.g., Halzen & Hooper, 2002), applied to X-ray binaries, *etc*. In such objects, the thickness of the surrounding gas can significantly exceed 100 g/cm^2, thus the protons produced in the central source would initiate (through the production of high energy γ-ray and electrons) electromagnetic showers. These sources perhaps represent the "best hope" of neutrino astronomy, but they are generally considered as less attractive targets for γ-ray astronomy. In photon fields such cascades can be created on almost all astronomical scales, from compact objects like accreting black holes, fireballs in gamma-ray bursts, and sub-pc jets of blazars, to large-scale (up to 100 kpc) AGN jets and larger than 1 Mpc clusters of galaxies. Very high energy γ-rays emitted by astronomical objects can initiate cascade in the whole universe by interacting with the background radiation fields. Such mechanism can make significant contribution to the diffuse extragalactic γ-ray background.

Cascade in a magnetic field is crucial to understand of the physics of pulsar magnetospheres (Sturrock, 1971; Baring & Harding, 2001). Such cascades can also play a role in Earth's geomagnetic field (Anguelov & Vankov, 1999; Plyasheshnikov & Aharonian, 2002), accretion disks of massive black holes (Bednarek, 1997), *etc*. In general, the pair cascades in magnetic fields are effective when the product of the particle (photon or electron) energy and the strength of the B-field becomes close to the "quantum threshold" of about $EB \geq B_{\rm crit} m_e c^2 \sim 2 \times 10^7$ TeV Gauss.

1.2 Acceleration Mechanism

The question of how to accelerate cosmic rays to the observed energies has long been discussed. Italian-American physicist Fermi (1949) for the first time proposed that cosmic rays can be accelerated via diffusion between collisions by the randomly moving interstellar clouds. It was subsequently

realized that shocks or any regions of converging outflows could efficiently accelerate the particles in a similar manner, which is also called first-order Fermi acceleration.

1.2.1 Shock acceleration

The principle of first-order Fermi acceleration is usually applied to the collisionless-shock, where Coulomb scattering is negligible and the energy and momentum transferred between particles and shocks are only mediated by plasma processes. Denoting the velocities of upstream and downstream fluids in the rest frame of the shock front, the velocity of which is u_s in the lab frame, to be $u_{\rm u} = u_s$ and $u_{\rm d}$ respectively, we can find the $u_{\rm d} = u_s/4$ based on the Ranking-Hugoniot condition in the strong shock limit (shock speed $\gg$ sound speed).

Suppose a charged particle with energy E_0 starts off in the upstream side and enter the downstream with a pitch angle θ with respect to the shock normal, we find the energy of the particle viewed in the rest frame of the downstream reads,

$$E_0' = \gamma E_0(1 - \beta\cos\theta) \tag{1.41}$$

where $\beta = u_{\rm u} - u_{\rm d} = 3u_s/4c$ and $\gamma = 1/\sqrt{1-\beta^2}$. The "scattering" between the particle and the fluid is due to the motion in the magnetic field so the "scattering" is elastic. Thus, we have the particle's energy after scattering is $E_1' = E_0'$ in the rest frame of the downstream region. If we transform the particle's energy back to the rest frame of the upstream, we have

$$E_1 = \gamma E_0'(1 + \beta\cos\theta') = \gamma^2 E_0(1 - \beta\cos\theta)(1 + \beta\cos\theta') \tag{1.42}$$

where θ' is the pitch angle relative to the shock normal after the scattering. Assuming the particle move randomly both before and after the scattering, we can average over the pitch angle to get the average energy gain per upstream-downstream-upstream cycle. To do this, we need to bear in mind that the pitch angle distribution of the particle entering the downstream region and returning back to the upstream region are, respectively,

$$\frac{dn}{d\cos\theta} = 2\cos\theta, \quad -1 \le \cos\theta \le 0, \tag{1.43}$$

and

$$\frac{dn}{d\cos\theta'} = 2\cos\theta', \quad 0 \le \cos\theta' \le 1. \tag{1.44}$$

After carrying out the calculation, we obtain the average energy increment of the particle in one upstream-downstream-upstream cycle is

$$\frac{\Delta E}{E} = \frac{E_1 - E_0}{E_0} = \gamma^2\left(1 + \frac{4}{3}\beta + \frac{4}{9}\beta^2\right) \tag{1.45}$$

For non-relativistic shock ($\beta \ll 1$), we have $\frac{\Delta E}{E} \simeq \frac{u_s}{c}$.

Of course, the shock acceleration efficiency also depends on how much time it requires to accomplish one cycle. This is then determined by the way that cosmic ray move in both the upstream and the downstream region, or the way that cosmic rays are scattered. Bell (1978) suggested that cosmic rays can scatter off Alfvén waves generated by themselves and then move in a diffusive way. Thus, shock acceleration is also referred to diffusive shock acceleration (DSA). This process reduces particle's stream speed roughly to Alfvén speed and make it inevitable that the particle is overtaken by the shock. On the other hand, this process provides a certain possibility for particles in the downstream to return back to the upstream instead of convecting away with the downstream fluid. The average residence times of a particle in the upstream region and downstream region can be given by $t_\mathrm{u} = 4\kappa_\mathrm{u}/u_\mathrm{u}c$ and $t_\mathrm{d} = 4\kappa_\mathrm{d}/u_\mathrm{d}c$ respectively, where $\kappa_\mathrm{u} = \lambda_\mathrm{u}c/3$ and $\kappa_\mathrm{d} = \lambda_\mathrm{d}c/3$ are the spatial diffusion coefficient in the upstream and downstream with λ_u and λ_d being the mean free path of wave-particle interaction in the upstream and downstream respectively. The total time to accomplish one cycle is $t_\mathrm{cyc} = t_\mathrm{u} + t_\mathrm{d}$ and we can find the acceleration timescale

$$t_\mathrm{acc} = t_\mathrm{cyc}\left(\frac{E}{\Delta E}\right) = \frac{4}{u_s}\left(\frac{\kappa_\mathrm{u}}{u_\mathrm{u}} + \frac{\kappa_\mathrm{d}}{u_\mathrm{d}}\right) \tag{1.46}$$

In the limit of Bohm diffusion, we have $\kappa_\mathrm{u} = \kappa_\mathrm{d} = r_g c/3$ where $r_g = E/eB$ is the Larmor radius of the particle. We can then get

$$t_\mathrm{acc} = \frac{20}{3}\frac{r_g}{c}\left(\frac{c}{u_s}\right)^2 \tag{1.47}$$

1.2.2 Stochastic acceleration

When particles scatter off MHD waves in the downstream and the upstream, they actually can also gain energy in those scatterings. But the shock velocity is usually much larger than the phase speed of the MHD wave, so the energy gain via scattering off the waves are neglected. In the case that the phase speed of the MHD wave is high, acceleration by MHD waves is also efficient. Similarly to the case of shock acceleration, we consider a particle with energy E_0 in lab frame is scattered by a MHD wave such as Alfvén with phase speed u_A. The energy of the particle viewed in the rest frame of the wave is given by Eq. 1.41 with θ being the angle between the particle velocity and the wave velocity, $\beta = u_A/c$ and $\gamma = 1/\sqrt{1-\beta^2}$ in this case. The scattering in the rest frame of the wave is elastic since the electric field vanishes and the particle's energy after scattering can be given by Eq. 1.42 after being converted back to the lab frame. Next, we also need to average over the pitch angle. For the

emergence angle, if we assume both particles and waves move randomly, the distribution of the pitch angle should be isotropic, i.e., $dn/d\cos\theta' = \text{Constant}$. On the other hand, the probability of a collision is proportional to the relative velocity between the wave and the particle, so we have

$$\frac{dn}{d\cos\theta} = \frac{c - u_A\cos\theta}{2c} \tag{1.48}$$

We can also see that the probability for a "head-on" collision ($\cos\theta < 0$) which will increase the energy of the particle is larger than the "tail-on" collision ($\cos\theta < 0$) which will make the particle lose energy, and hence particle will eventually gain energy after lots of scatterings. But this mechanism will lead to the diffusion of the distribution of particles in the momentum space. After some calculation, the energy increment in one scattering can be obtained by

$$\frac{\Delta E}{E} = \frac{4}{3}\gamma^2\beta^2 \tag{1.49}$$

Given a non-relativistic MHD wave, we have $\Delta E/E = \frac{4}{3}\beta^2$. Since the energy increment is proportional to the square of the speed of the scattering center, this mechanism is called the second-order Fermi acceleration. Because the scattering centers in this case are usually assumed to be moving in random directions, this mechanism is also referred to stochastic acceleration. The average time needed for one scattering is just the time to propagate one mean free path. Thus, we have the stochastic acceleration timescale

$$t_{\text{sto}} = \frac{\lambda}{c}\frac{E}{\Delta E} \tag{1.50}$$

In the limit of Bohm diffusion, we have

$$t_{\text{sto}} = \frac{3}{4}\frac{r_g}{c}\left(\frac{c}{v_A}\right)^2 \tag{1.51}$$

1.2.3 Shear acceleration

Shear acceleration is also a Fermi-type acceleration mechanism. It was firstly proposed by Berezhko and his collaborators in 1980s. In this mechanism, they considered particle propagating in a shearing flow with a velocity gradient inside the flow. Energetic particles could sample the velocity difference while they move across the flow by scattering off MHD waves which are embedded in different layers of the shearing flow with different bulk velocities. Different layers then serve as the scattering center and each scattering is then accompanied by the conversion of bulk kinetic energy of the flows to particle energies. The most considered shearing profile of the flow is a longitudinal shear with linear velocity gradient. More specifically, let's consider a

flow moving along z-axis with velocity $\vec{u} = u(x)\vec{e}_z$ of a shear in the x-axis and $\partial u/\partial x$ =Constant. In one mean free path of wave-particle interaction, the velocity difference of the background flow where a particle locates can be given by

$$\delta u = \frac{\partial u}{\partial x}\lambda \sin\theta \tag{1.52}$$

where θ is the angle between the velocity of the particle and z-axis. Denote the initial energy of the particle by E_0, the energy of the particle viewed in the rest frame of the background flow where the particle arrives at after one mean free path is then

$$E_1 = \gamma E_0(1 - \beta\cos\theta)s \tag{1.53}$$

where $\beta = \delta u/c$ and $\gamma = 1/\sqrt{1-\beta^2}$. Usually, we have $\beta \ll 1$ and $\gamma \simeq 1 + \beta^2/2$, unless we consider an ultra-relativistic shearing flow. Provided that the particle velocity is randomly oriented, one can average over θ and find the energy increment in one scattering is

$$\frac{\Delta E}{E} = \frac{2}{15}\gamma^4\beta^2 \simeq \frac{2}{15}\beta^2. \tag{1.54}$$

From the point of view of the expression for the energy increment, the shear acceleration is a second-order Fermi acceleration mechanism. Indeed, similar to the second-order stochastic acceleration, it can lead to the diffusion of the distribution of particles in the momentum space, since the energy of particle could either increase or decrease in one scattering, depending on the pitch angle. On the other hand, from the point of view of the energy conversion, shear acceleration is similar to shock acceleration since the non-thermal energy of particles is converted from the kinetic energy of the background flow. The acceleration timescale in the limit of Bohm diffusion is then

$$t_{\rm acc} = \frac{\lambda}{c}\frac{E}{\Delta E} = \frac{15}{2}\frac{r_g}{c}\left(\frac{c}{\delta u}\right)^2 \tag{1.55}$$

Note that δu usually increases with the particle's energy. This is because the mean free path usually increases with the particle's energy so that a larger velocity difference of the background flow will be experienced by the particle between two scattering events. This makes the shear acceleration a more efficient mechanism for higher energy particles.

Compare Eqs. 1.47, 1.51 and 1.55, we can see the acceleration timescales of shock, stochastic and shear acceleration have a similar form in spite of the prefactors. Indeed, all these three mechanisms rely on the scattering processes which convert kinetic energy of the scattering centers to particles. The main difference is the geometry of the scattering. Fermi acceleration has been widely applied to the acceleration of energetic particles in various astrophysical objects such as solar flares (Murphy et al., 1987), supernova

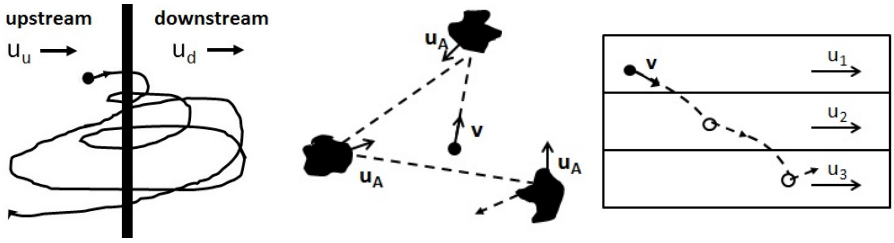

Figure 1.2: **Left panel**: Schematic diagram for the shock acceleration. The filled black circle and the thick vertical solid line shows the initial position of a particle and the shock front respectively. The upstream and downstream fluid move rightward with $u_{\rm u}$ and $u_{\rm d}$ respectively. The thin solid curves show the trajectory of the particle recrossing the shock. **Middle panel**: Schematic diagram for the stochastic acceleration. The black filled irregular regions represent MHD waves (turbulence) or the so-called magnetic clouds with a velocity u_A. The filled circle represent a particle and the dashed line shows its trajectory. The particle will be scattered when it encounters a magnetic cloud (i.e., resonate with a MHD wave), In a single scattering, particle could gain or lose energy, depending on the incidence and emergence angle. But after many scatterings, a net energy gain will be in achieved. **Right panel**: Schematic diagram for the shear acceleration. u_1, u_2, u_3 are the bulk velocities in different parts of a flow. The filled circle shows the initial position of the particle. The dashed line shows the trajectory of the particle in the flow. The particle could be scattered at different parts of the flow (as marked with the open circle) and gain energy from the flow.

remnants (Bell, 1978; Lagage & Cesarsky, 1983; Aharonian et al., 2001; Drury et al., 2001; Aharonian et al., 2004; Vink, 2006), stellar winds (Webb et al., 1985), and pulsar wind termination shocks (Kroon et al., 2016) within the Milky Way; the jets and hot spots from radio galaxies (Begelman & Kirk, 1990), AGN jets (Rieger & Mannheim, 2002; Pogge, 1997), blazars (Stecker et al., 2007), vicinity of supermassive black hole (Liu et al., 2006), and GRBs (Waxman, 1995).

Beside the Fermi acceleration mechanism, magnetic reconnection is also a well discussed mechanism. Charged particles can be accelerated in the large scale electric field generated in the dissipation along the current sheet which is formed when highly conducting plasma inflows encounter each other. A detailed description of this mechanism is beyond the scope of this section and one can refer to Zweibel & Yamada (2009). Note that particles can also gain energy by traveling back and forth several times across the two converging plasma inflows, similar to shock acceleration.

1.3 Statistical Technique and Application

1.3.1 Minimum χ^2 estimation

When we use a model to fit data, we usually expect to get an idea of how good the fit is. χ^2 statistic is one method of measuring the agreement between data and the given model. The statistical function is defined as

$$\chi^2 = \sum_{i=1}^{N} z_i^2 = \sum_{i=1}^{N} \left(\frac{y_i^{\text{pre}} - y_i^{\text{obs}}}{\sigma_i} \right)^2 , \tag{1.56}$$

where y_i^{obs} are the observed data values, y_i^{pre} are the corresponding values predicted by the model, and σ_i are the uncertainties in the measurement. N is the number of degrees of freedom. If the residuals $y_i^{\text{pre}} - y_i^{\text{obs}}$ are typically of the same size as σ_i, then $z_i \sim 1$ and $\chi^2 \sim N$, and this suggests that the model is a reasonable fit to the data. If the residuals are much larger or smaller than σ_i, this suggests a poorer fit.

If z_i have Gaussian independent distributions with mean 0 and variance 1, then χ^2 follows a χ^2 distribution. The probability density function for the χ^2 distribution with N degrees of freedom is shown in Figure 1.3. We can see the higher the number of degrees of freedom, the further to the right is the curve. The central limit theorem[1] tells us that if the degrees of freedom is large enough, the χ^2 distribution is an asymptotically Gaussian distribution.

In general, z_i is not independent. In this case, if we fit a linear model with p parameters (i.e. parameters that are independent) to N independent data points, then the χ^2 distribution has $N - p$ degrees of freedom. Sometimes people use the reduced chi-squared which is simply χ^2 divided by the number of degrees of freedom to measure the agreement between data and the given model.

$$\chi_r^2 = \frac{1}{N-p} \sum_{i=1}^{N} z_i^2 = \frac{1}{N-p} \sum_{i=1}^{N} \left(\frac{y_i^{\text{pre}} - y_i^{\text{obs}}}{\sigma_i} \right)^2 \tag{1.57}$$

If $\chi_r^2 = 1$ suggests that it's a good fit.

However, in some practical applications, the number of observations are low, in which case the probability of measuring y^{obs} given the expected value y_i^{pre} will obey other kind of distributions (e.g., Poisson distribution) rather than Gaussian distribution, so the χ^2 will not follow the χ^2 distribution. In this case, the maximum likelihood estimation can be another optional method to fit the data.

[1] Statement: if y is the sum of N independent random variables, x_i, i = 1,2,...N, each drawn from a distribution with mean μ_i and variance v_i, then the density distribution for y
1. has an expectation value (expected mean) $E[y] = \sum_i \mu_i$;
2. has a variance $\text{Var}(y) = \sum_i \mu_i$;
3. becomes Gaussian in the limit $N \to \infty$. .

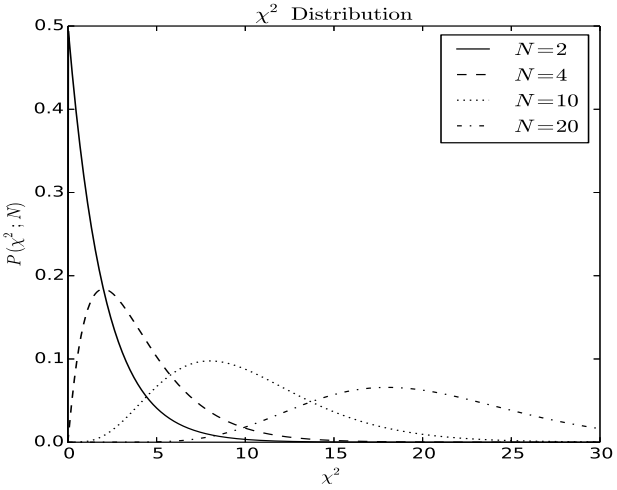

Figure 1.3: The χ^2 distribution for 2, 4, 10, 20 degrees of freedom. The higher the number of degrees of freedom, the further to the right is the curve.

1.3.2 Maximum likelihood estimation

The likelihood $P(D|\theta)$ represents the probability of observing event D given the model hypothesis is true. Maximum likelihood estimation (MLE) is the most common method of estimating the parameter values that maximize the likelihood $P(D|\theta)$. In practice the observed data D are discrete, so we define a one-dimensional set of N values $D = \{d_i\}$ $(i = 1, 2, ..., N)$. Generally the probability of measuring d_i obey some kind of distribution, e.g., the Poisson distribution used in *Fermi*-LAT analysis below, Gaussian distribution used in Section 1.3.5. If each of the N points has been drawn independently from this distribution, then the likelihood of the whole set of data is

$$L(D|\theta) = P(d_1|\theta)P(d_2|\theta)...P(d_N|\theta) = \prod_{i=1}^{N} P(d_i|\theta). \tag{1.58}$$

Generally, it is more convenient to use the logarithmic likelihood form ln $L(D|\theta)$. Because the computation of the product of a large number of small probabilities can easily underflow, and this is resolved by the sum of the log probabilities; in addition, the logarithm is a monotonic function, so that maximization of the log of a function is equivalent to maximization of the function itself. When we use a model to fit the observed data, we hope to obtain the maximum value of the likelihood function (PDF). The first thought to have an extremum is to solve the first-order partial differential equation

of the posterior PDF with respect to θ by setting it to 0. The solution is

$$\frac{\ln L(D|\theta)}{d\theta} = 0. \tag{1.59}$$

However, in most cases the high dimensional parameter space and the complex distribution of the PDF make it impossible to obtain analytic solutions. The only way to solve this problem is the numerical analysis by sampling these model parameters θ directly.

Maximum likelihood estimation and χ^2 estimation

For Gaussian distribution of measurement noise with varying standard deviation, σ_i, the probability of the data set coming from the model parameters is given by

$$L = \prod_{i=1}^{N} \frac{1}{\sqrt{2\pi\sigma_i^2}} \exp\left(-\frac{[y_i^{\rm pre}(\theta) - y_i^{\rm obs}]^2}{2\sigma_i^2}\right) \tag{1.60}$$

$y_i^{\rm pre}(\theta)$ is the given model with parameters θ, and $y_i^{\rm obs}$ is the observational data. Taking the logarithm,

$$\ln L = K - \sum_{i=1}^{N} \frac{[y_i^{\rm pre}(\theta) - y_i^{\rm obs}]^2}{2\sigma_i^2} \tag{1.61}$$

$$-\ln L \propto \sum_{i=1}^{N} \frac{[y_i^{\rm pre}(\theta) - y_i^{\rm obs}]^2}{2\sigma_i^2} \equiv \frac{1}{2}\chi^2 \tag{1.62}$$

The $\ln L$ function is related to the χ^2 parameter, $\chi^2 = -2\ln L$, so the maximization of the $\ln L$ is equivalent to a minimization of χ^2.

Likelihood ratio test

Suppose a null hypothesis [2] and an alternative hypothesis [3]are under consideration, the first model is simpler or more parsimonious than the second one. While the most common situation is to consider "nested" models, where the first model is obtained from the second model by putting some of the parameters to be zero. For instance, the first model describes N point sources, while the second model has N+1 sources. The likelihood ratio (LR) test statistic, also called test statistic (TS), is given by

$$TS = -2\ln\left(\frac{L(\theta_0)}{L(\theta_1)}\right), \tag{1.63}$$

[2]The null hypothesis is a hypothesis which the researcher tries to disprove, reject or nullify.

[3]The alternative hypothesis is a hypothesis which the researcher really thinks is the cause of a phenomenon.

where $L(\theta_0)$ and $L(\theta_1)$ are the two likelihood values. When there are many events, Wilks's theorem[4] states that the TS distribution asymptotically tends to a χ^2 distribution

$$TS = -2\ln\left(\frac{L(\theta_0)}{L(\theta_1)}\right) \sim \chi^2_r, \tag{1.64}$$

where r is the number of parameters characterizing the additional source in the alternative model. As a general rule, the TS value is approximately the square of the significance.

1.3.3 Likelihood application in *Fermi*-LAT fitting

The likelihood technique (Cash, 1979; Mattox et al., 1996) has been applied to the analysis of LAT data. It is performed in counts space. First a likelihood function that is applicable to the LAT data needs to be constructed. If the LAT data are divided into N (time, energy, sky pixel...) bins, the observed number of counts in each bin will be very small. Assume the expected number of counts in the ith bin is m_i which is a function of the source model, then the probability of measuring n_i counts in this bin obeys the Poisson distribution[5], namely,

$$p_i = \frac{e^{-m_i} m_i^{n_i}}{n_i!}. \tag{1.65}$$

In practice, the expected number of counts m_i derived from the model is unknown and the goal is to estimate the value of m_i given n_i. The likelihood L is the product of p_i for each time bin,

$$L = \prod_{i=1}^{N} p_i = e^{-N_{\rm exp}} \prod_{i=1}^{N} \frac{m_i^{n_i}}{n_i!}. \tag{1.66}$$

The logarithmic likelihood is given by

$$\ln L = -N_{\rm exp} + \sum_{i=1}^{N} n_i \ln m_i - \sum_{i=1}^{N} \ln n_i!. \tag{1.67}$$

We can see the first term $N_{\rm exp} = \sum_{i=1}^{N} m_i$, which is the total number of counts that the source model predicts, is purely a function of the spectral model. The second term is a function of both the source model and the data. The last term only depends on the observed data.

For the model fitting, we expect to get the highest probability of detecting one source and obtain the best fit parameters including both the spectrum

[4] https://en.wikipedia.org/wiki/Likelihood-ratio_test#Wilks.27_theorem
[5] https://en.wikipedia.org/wiki/Poisson_distribution

and its location, so we use the TS to fit the data and test the hypothesis. The TS is defined as:

$$TS = -2\ln\left(\frac{L_{max,0}}{L_{max,1}}\right), \tag{1.68}$$

Here $L_{max,0}$ is the maximum likelihood value for a model without an additional source (the null hypothesis) and $L_{max,1}$ is the maximum likelihood value for a model with an additional source (the alternative hypothesis) at a specified location. TS is maximized when the likelihood for the model with the source is maximized. There are five optimizers in *Fermi*-LAT science tools that can be used to maximize the logarithmic likelihood function and determine the best-fit spectral parameters: *DRMNGB, DRMNFB, EWMINUIT, MINUIT* and *LBFGS*. Generally speaking, the best way to find the parameter estimates is to use *DRMNGB* (or *DRMNFB*) to find initial values and then use *MINUIT* (or *NEWMINUIT*) to find more accurate results.

1.3.4 Markov Chain Monte Carlo method

Bayes theorem

Bayes theorem is fundamental in Bayesian inference (e.g. hypothesis testing, model fitting), and it shows the relation between two conditional probabilities that are the reverse of each other. Taking D as some data which we have obtained to test the model with parameters θ, then Bayes theorem is stated mathematically as the following equation:

$$P(\theta|D) = \frac{P(D|\theta)P(\theta)}{P(D)}, \tag{1.69}$$

where the posterior $P(\theta|D)$ is the conditional probability of model parameters given the observing event D is true. The term in the numerator $P(D|\theta)$ is the likelihood and represents the probability of observing event D given that the model hypothesis is true. $P(\theta)$ is the prior and the denominator $P(D)$ is the evidence. $P(D)$ does not depend on the model parameters, we can consider it as an integration constant for the posterior, so that the unnormalized posterior is just the product of the likelihood and prior.

Why use Markov Chain Monte Carlo method

In most cases the posterior PDF is not of a standard distribution form (e.g, highly peaked, multimodal), and it's hard to sample finely and sufficiently. In addition, to determine the posterior by evaluating on a regular, but multi-dimensional parameter grid is far too inefficient. Monte Carlo (MC) method can provide an efficient way to sample from a proposal distribution ($Q(\theta)$) directly rather then define an arbitrary set of grid values of θ at which we then

evaluate the posterior. Unfortunately, the MC method is often inefficient, because the rejection sampling[6] wastes a lot of time drawing samples in regions where the posterior $P(\theta|D)$ is low.

Markov chain Monte Carlo algorithm

In Bayesian statistics, MCMC method is a "smart" method to sample and estimate the posterior PDF over high dimensional parameter space, and find the maximum posteriori estimation. The principle of MCMC method is to set up a random walk over the parameter space θ, and the posterior probability $P(\theta|D)$ improves as a function of the number of steps. The random walk is achieved using a Markov chain, which means that the probability of moving from sample θ_t to θ_{t+1} is defined by a transition probability $Q(\theta_{t+1}|\theta_t)$ which is independent of the step number. In a Markov Chain the next position depends only on the current position. The simplest and most commonly used MCMC algorithm is the Metropolis-Hastings (M-H) algorithm. The iterative procedure (Foreman-Mackey et al., 2013) is as follows:

1. Draw a set of parameter values θ' from the proposal distribution given a current set of parameter values θ_t: $\theta' \sim Q(\theta'|\theta_t)$.
2. Define $\sigma = \frac{P(\theta')Q(\theta_t|\theta')}{P(\theta_t)Q(\theta'|\theta_t)}$.
3. Pick a number from an uniform distribution between 0 and 1: $r \sim U(0,1)$.
4. If $r \leq \sigma$ then
5. Replace the next parameter set with the proposed set and then repeat: $\theta_{t+1} \leftarrow \theta'$
6. else
7. Assign the current parameter set to the next set: $\theta_{t+1} \leftarrow \theta_t$
8. end if

1.3.5 Naima and application of MCMC

Naima (Zabalza, 2015) is an open-source python package for the computation of nonthermal radiative output from relativistic particles. It can infer the properties of the corresponding particle distribution given an output nonthermal spectrum. There are two main components of the package: several radiative models, e.g., synchrotron, inverse compton, nonthermal

[6] https://en.wikipedia.org/wiki/Rejection_sampling

bremsstrahlung, and neutral pion decay , and a set of utility particle distribution functions, e.g., power-law form, exponential cutoff power-law form and *etc*. Users can also define their own particle distribution functions that make it flexible to implement any type of particle cooling, escape, or acceleration physics before computing its radiative output. Naima uses the physical unit module astropy.units in the astropy package[7] to convert the input spectra and parameters in their needed units during the calculations.

Assuming that the probability of the observed flux and uncertainties (F_i, σ_i) in this measurement obeys Gaussian distribution, the likelihood function L is the product of the N times measurements

$$L = \prod_{i=1}^{N} \frac{1}{\sqrt{2\pi\sigma_i^2}} \exp\left(-\frac{(S(\vec{p}, E_i) - F_i)^2}{2\sigma_i^2}\right), \tag{1.70}$$

where $S(\vec{p}, E_i)$ is the spectral model which is a function of the parameter vector $\vec{p}$ and energy E_i. Taking the logarithm,

$$\ln L \propto \sum_{i=1}^{N} \frac{(S(\vec{p}, E_i) - F_i)^2}{\sigma_i^2} \tag{1.71}$$

Then the likelihood function is provided to run an MCMC sampling, and estimate the sampled parameters.

In practical application, we need to provide the observed flux and uncertainties (F_i, σ_i), photon spectral model $S(\vec{p}, E_i)$ derived from the electron spectrum, and a prior likelihood function to the function *run_sampler* to fit the data. The function *run_sampler* will further call the *emcee* module *EnsembleSampler*[8] to execute MCMC sampling. A full explanation of the *emcee* can be found in http://dan.iel.fm/emcee/current/.

How many MCMC iterates are needed can not be firmly answered. The easiest and simplest indicator that the iterations are sufficient is the acceptance fraction, it should be in the 0.2 to 0.5 range; another indicator is when the correlation time is much shorter than the run time by a factor of ~ 10, which will make sure that it has run long enough. (Foreman-Mackey et al., 2013)

[7] http://docs.astropy.org/en/stable/units/
[8] http://dan.iel.fm/emcee/current/api/#emcee.EnsembleSampler

1.4 Instruments and Data Analyses

1.4.1 *Fermi*-LAT and extended sources analysis

Operational principle

The Large Area Telescope (LAT), launched by NASA on June 11, 2008, is the principal scientific instrument on board the *Fermi Gamma-ray Space Telescope* (*Fermi*)[9]. The high-energy γ-rays cannot be refracted by a lens or focused by a mirror, therefore the *Fermi*-LAT is designed as a pair-conversion telescope. The LAT consists of three main detector systems, an thin plastic anti-coincidence detector (ACD), a silicon strip tracker, and a calorimeter. Figure 1.4 shows the principles of LAT operation. Incident γ-rays pass freely through the ACD, the ACD surrounds the tracker and provides rejection of charged cosmic ray (CR) backgrounds and identifies the relatively rare γ-rays. A γ-ray continues until it interacts with an atom in one of the thin tungsten foils, producing two charged particles: e^+ and e^-: $\gamma\,(\mathrm{E}_\gamma > 1.02\,\mathrm{MeV}) \rightarrow \mathrm{e}^+ + \mathrm{e}^-$. They proceed on, creating ions in thin silicon strip tracker. The silicon strips alternate in the X and Y directions, allowing the progress of the particles to be tracked. Finally the particles are stopped by the calorimeter which measures the total energy deposited. The information from the anticoincidence detector, tracker and calorimeter is combined to estimate the energy and direction of the γ-ray.

[9] http://fermi.gsfc.nasa.gov/

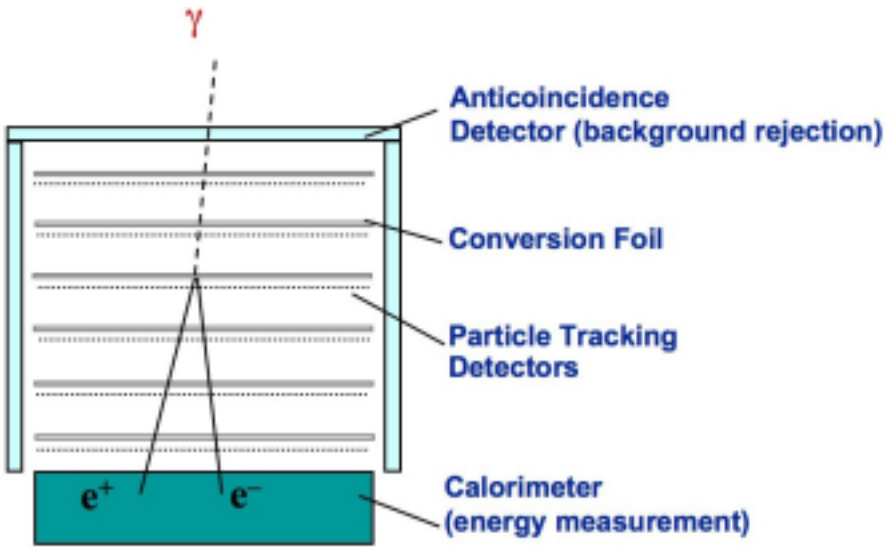

Figure 1.4: Principles of *Fermi*-LAT operation. Image taken from https://www-glast.stanford.edu/instrument.html.

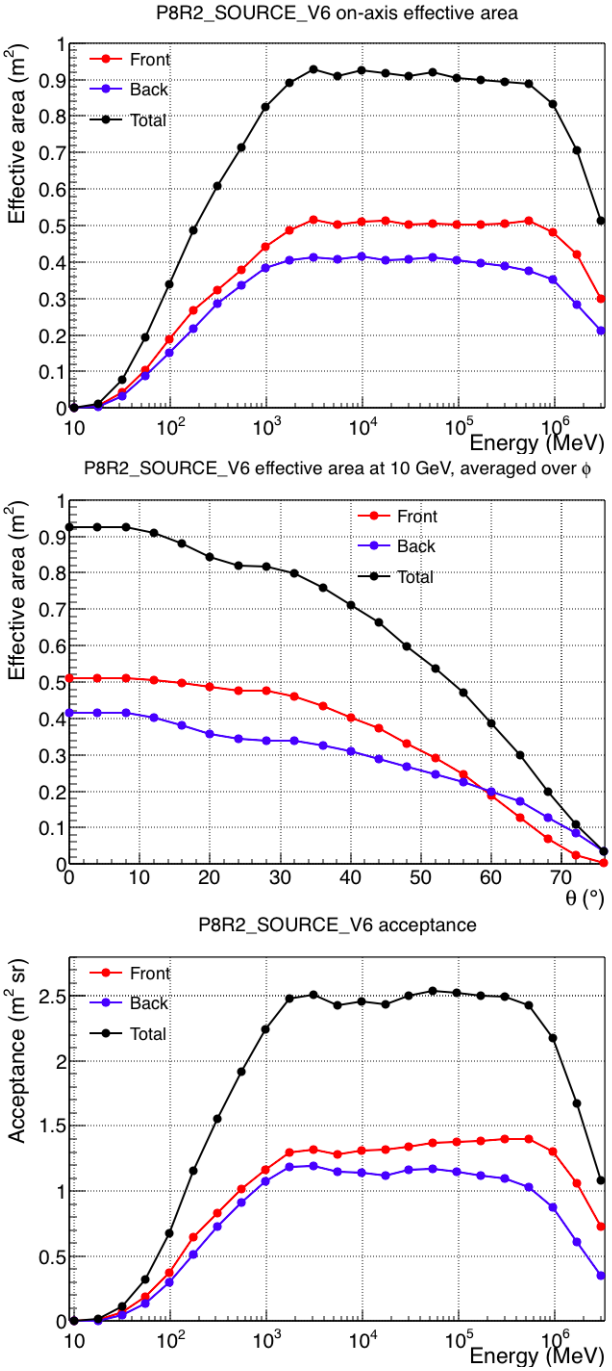

Figure 1.5: The performance of the Pass 8 event class. Images taken from https://www.slac.stanford.edu/exp/glast/groups/canda/lat_Performance.htm.

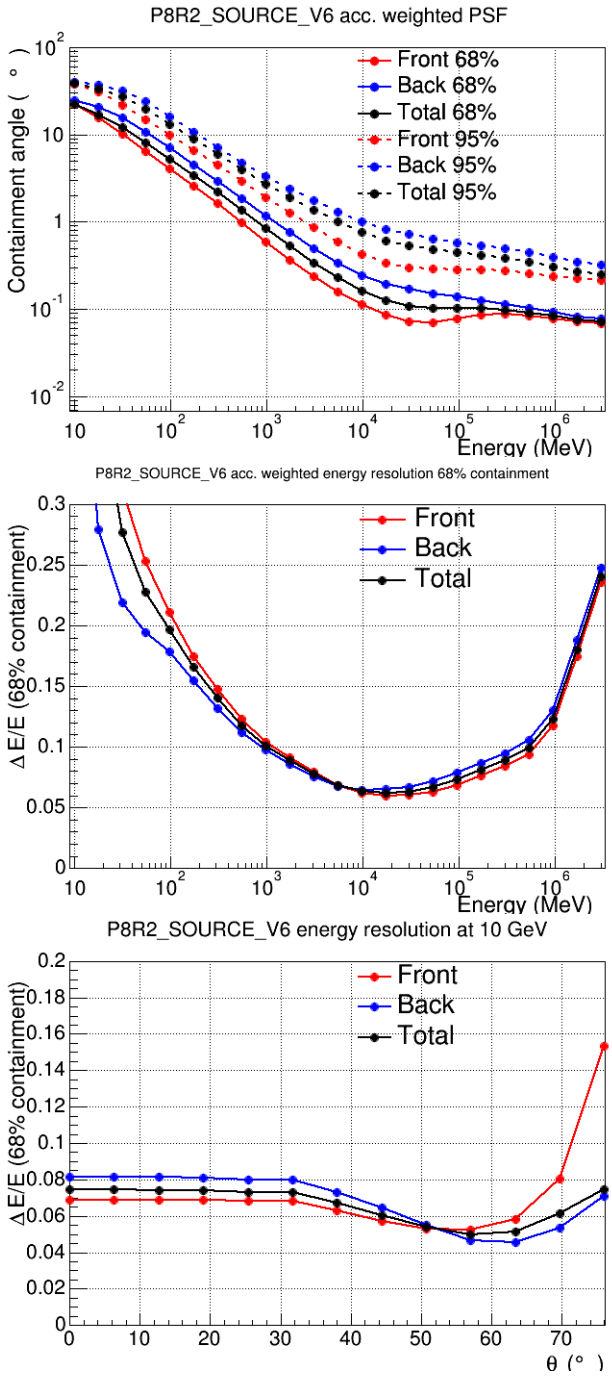

Figure 1.5 — continued

Performance

Fermi-LAT is an imaging, wide field-of-view (FOV), high-energy γ-ray telescope, detecting photons from 20 MeV to more than 300 GeV (Atwood et al., 2009). The FOV covers about 20% (> 2 sr) of the sky. Instrument response

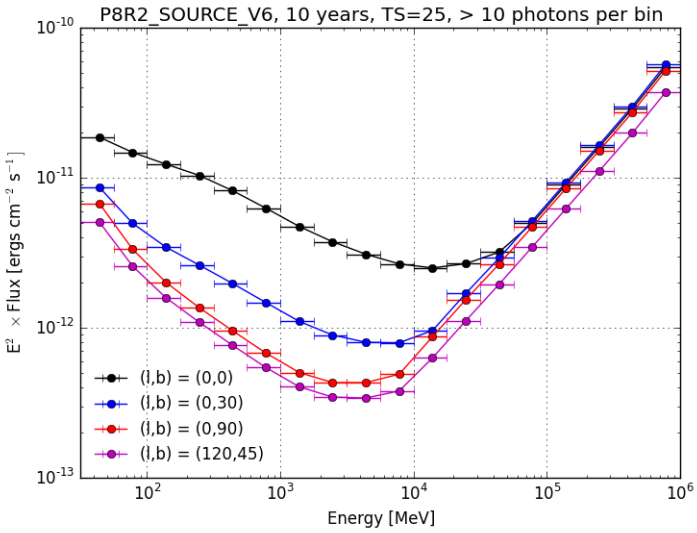

Figure 1.6: Point source differential flux sensitivity between 31.6 MeV and 1 TeV. Image taken from https://www.slac.stanford.edu/exp/glast/groups/canda/lat_Performance.htm.

functions (IRFs), the parameterized representations of *ScienceTools* performance, can be factorized into four parts: the effective area of the detector, acceptance (the integral of the effective area over the solid angle), the angular resolution as given by the point spread function (PSF), and energy dispersion. Detailed information about the associated IRFs are given in Ackermann et al. (2012). Pass 8 data and science tools version *v10r0p5* are the updated versions of previous Pass 7 reprocessed (P7REP) data and science tools version *v9r33p0* correspondingly. The performance of the Pass 8 event class is shown in Figure 1.5. The first two images are the effective collecting area as a function of photon energy and incidence angle. The effective area is larger than 9000 cm^2 at 10 GeV in the center of the FOV. The third image shows the acceptance. 68% and 95% containment radii (angular resolution) of the acceptance weighted PSF as a function of energy are given in the fourth image. The energy resolution depends on the γ-rays energy and its incidence angle are shown in the last two images. Based on the above instrument performance characterizations, the point source flux sensitivity is derived assuming a power-law spectrum with index 2 and is shown in Figure 1.6, the curves are for four different locations in Galactic coordinates: Galactic center, intermediate latitudes, north Galactic pole, and north Celestial pole.

Extended source analysis

The analysis of an extended source is performed using the following steps:

i. Extract event data

The photon event data are extracted from the LAT data server https://fermi.gsfc.nasa.gov/cgi-bin/ssc/LAT/LATDataQuery.cgi. The required search parameters are object name or coordinates, search radius R, time range, and energy range. Equatorial coordinates J2000, mission elapsed time (MET) system, and spacecraft data are selected.

ii. Event selections

gtselect is used to filter the time range, energy range, and event class of the original photon data. It can also filter the zenith angle. Then *gtmktime* is used to pick out the good time intervals (GTI) with valid data based on above filtered photon data and the spacecraft file.

iii. Counts map

The counts map is created by the tool *gtbin* with CMAP option to make out the emission of the extended structures. For binned likelihood analysis, a 3D (binned) counts map with an energy axis, called a counts cube is built by *gtbin* with CCUBE option. The counts map is an internally tangent square region of the extracted circular region, so the region of interest (ROI) is the square with the length for a side $\sqrt{2}R$.

iv. Create spatial template

For consistency, it is often better to build a two dimensional template to describe the extended emission in the model. There are a few things that must be compatible with the *Fermi*-LAT products, (a) the template must be in J2000 coordinates. (b) The background must be set to 0, namely, set all of the points below a certain value to 0. (c) The total flux must be normalized to 1, namely, one needs to integrate over the entire map to get the normalization factor and divide each pixel by this number. Here *pyFits*[10] is used to divide, subtract and normalize the map.

v. Compute livetimes and exposure

To speed up the exposure calculations performed by likelihood, *gtltcube* is used to create a livetime cube which is the livetime as a function of sky position and off-axis angle. Then the *gtexpcube2* tool applies the livetime cube to the ROI, and generates a binned exposure map. Here

[10] http://www.stsci.edu/institute/software_hardware/pyfits

in order to consider the effects of the large PSF of the LAT, an exposure map that includes sources up to 10 degrees outside the ROI should be created.

vi. XML model file

The tool *make3FGLxml.py*[11] is ran to generate a XML model for a given spectral and spatial model from the third year LAT source catalog (3FGL)[12] analysis for each source. Meanwhile the extended source templates, the latest Galactic diffuse emission model *gll_iem_v06.fits*, and the extragalactic isotropic model *iso_P8R2_SOURCE_V6_v06.txt*[13] are loaded into the XML model. The model includes the parameters of the source's spectrum, position, and intensity.

vii. Model counts map

The *gtsrcmaps* tool creates a model counts map for use with the binned likelihood analysis. It multiplies each source spectrum in the XML model by the exposure at the source position, and convolves that exposure with the effective PSF.

viii. Likelihood analysis – parameter optimization

We run *gtlike* to perform the likelihood analysis. In addition, we can also use another more powerful python tool *pyLikelihood* for the likelihood analysis. *pyLikelihood* can not only perform all of the same likelihood analysis like *gtlike*, but can access all of the model parameters. In addition, it can also calculate the upper limits.

1.4.2 *Planck* instrument and flux measurement

Instrument and scientific mission

Planck[14] (Tauber et al., 2010; Planck Collaboration et al., 2011a), launched on May 14, 2009, is the third generation space mission following the Cosmic Background Explorer (COBE) (angular resolution 7°; microwave, infrared; launched in 1989) and WMAP (angular resolution 13′; 23 - 94 GHz; launched in 2001). *Planck* scanned the whole sky twice in one year, with a combination of high sensitivity ($\frac{\Delta T}{T} \sim 2 \times 10^{-6}$ K) and angular resolution from 33′ to 5′. It carried two scientific instruments and executed observations in nine frequency bands, the Low-Frequency Instrument (LFI; Mandolesi et al., 2010;

[11] https://fermi.gsfc.nasa.gov/ssc/data/analysis/user/
[12] https://fermi.gsfc.nasa.gov/ssc/data/access/lat/4yr_catalog/
[13] https://fermi.gsfc.nasa.gov/ssc/data/access/lat/BackgroundModels.html
[14] http://www.esa.int/Planck

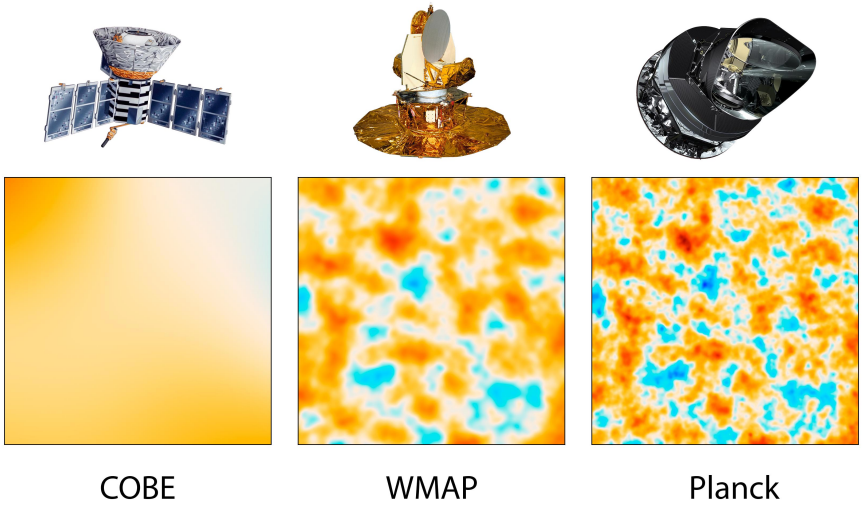

Figure 1.7: The three panels compare $10^\circ \times 10^\circ$ patches of all-sky maps created by COBE, WMAP, and *Planck* capable of detecting the CMB. The colors in the map represent different temperatures: red for warmer and blue for cooler. Image taken from http://photojournal.jpl.nasa.gov/catalog/PIA16874.

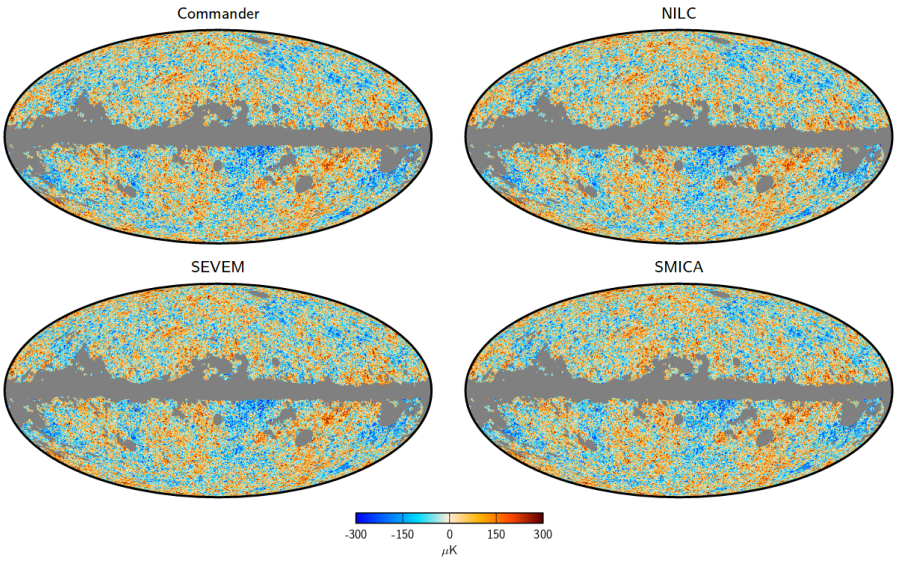

Figure 1.8: Component-separated CMB temperature maps at full resolution, FWHM=5′, $N_{\rm side} = 2048$. The colors in the maps represent different temperatures: red for warmer and blue for cooler. Image taken from Planck Collaboration et al. (2016c).

Bersanelli et al., 2010; Mennella et al., 2011) covers the 30, 44, and 70 GHz bands with amplifiers cooled to 20 K. The High Frequency Instrument (HFI; Lamarre et al., 2010; Planck HFI Core Team et al., 2011) covered the 100, 143, 217, 353, 545, and 857 GHz bands with bolometers cooled to 0.1 K. A combination of radiative cooling and three mechanical coolers produced the temperatures needed for the detectors and optics (Planck Collaboration et al., 2011b). Two data processing centres (DPCs) checked and calibrated the data and made maps of the sky (Planck HFI Core Team et al., 2011; Zacchei et al., 2011).

Planck's sensitivity, angular resolution, and frequency coverage make it a powerful instrument for Galactic and extragalactic astrophysics as well as cosmology (Planck Collaboration et al., 2016d). Details about the scientific operations of the *Planck* instrument can be found in Planck Collaboration et al. (2014b) and Planck Collaboration et al. (2016a). One main objective of *Planck* is designed to measure the oldest light in our universe, imprinted on the sky when the universe was just 380 000 years after the Big Bang, namely, measure the cosmic microwave background (CMB) at microwave and infrared frequencies. The three $10^\circ \times 10^\circ$ patches of all-sky maps in Figure 1.7 compare how much detail can be seen in the observations of COBE (left panel), WMAP (middle panel), and *Planck* (right panel) satellites used to measure the CMB. COBE's poor angular resolution make it impossible to see the small structures less than 7°, WMAP has found strong evidence for the much smaller structures, and *Planck*, with its greater resolution, has revealed the anisotropies of the CMB, e.g., with temperature fluctuation at a level of $\sim 10^{-5}$ K. It is of greatest interest for cosmology to accurately measure the anisotropies in small CMB structures, because this traits then can be used to measure the universe's geometry, content, and evolution; to test the Big Bang model and the cosmic inflation theory. *Planck* collaboration has applied four complementary CMB component separation algorithms (Commander, NILC, SEVEM, and SMICA) to the *Planck* sky maps, and the corresponding anisotropies of the component-separated CMB are shown in Figure 1.8. The colors in the map represent different temperatures: red for warmer and blue for cooler. These tiny temperature fluctuations correspond to regions of slightly different densities, representing the seeds of their all future structures: the stars, galaxies, and galaxy clusters of today.

Data reduction and flux density measurement

Here I summarize the basic steps of the *Planck* data analysis, details will be listed in Section 2.3.

i. Obtain the primary *Planck* all-sky maps, they are in Healpix format.

ii. Degrade or upgrade the resolution of the grid for consistence with other maps, e.g., γ-ray emission map.

iii. Project Healpix data onto two dimensional map.

iv. Temperature units and MJy sr^{-1} are converted to flux density per pixel Jy/pix.

v. Components modelling and separation.

vi. Use the aperture photometry to measure the flux density.

1.4.3 *Chandra* telescope and data processing

Chandra telescope and performance

The *Chandra* X-*ray Observatory* (*CXO*) was launched on July 23, 1999 by the space shuttle *Columbia*. The principle of measuring the photon energy is that an individual X-ray photon liberates multiple electrons in Si through photoelectric interaction, then *Chandra* detectors measure the photon energy according to the number of electrons. *Chandra* provides unprecedented capabilities for subarcsecond angular resolution ($\leq 0.5''$) imaging, and sensitivity $\sim 4\times10^{-15}$erg/cm^2/s. The Science Instrument Module (SIM) holds the two focal plane instruments, the Advanced CCD (charged coupled device) Imaging Spectrometer (ACIS) and the High Resolution Camera (HRC). ACIS has an energy range of 0.08 - 10 keV, and the effective area is about 110 cm^2 at 0.5 keV, 600 cm^2 at 1.5 keV, and 40 cm^2 at 8 keV. It is used for studying the temperature variation across X-ray sources such as vast clouds of hot gas in intergalactic space, or chemical variations across clouds left by supernova explosions. The HRC, with energy range of 0.06 - 10 keV, accurately records the position, number, and energy of X-rays, and is especially useful for imaging hot matter in remnants of exploded stars, and in distant galaxies and clusters of galaxies, and for identifying very faint sources.[15] ACIS include two kinds of CCD layouts: ACIS-I has a FOV of $16.9'\times16.9'$, and ACIS-S has a FOV of $8.3'\times50.6'$. HRC also include two kinds of CCD layouts: HRC-I has a FOV of $30'\times30'$, and HRC-S has a FOV of $6'\times90'$.[16] Because the vast majority of X-rays from the universe are absorbed by earth's atmosphere, *Chandra* must orbit above it, up to an altitude of $\sim$ 140,000 km in space (Weisskopf et al., 2000b, 2002), which is about a third of the distance to the moon. *Chandra* has observed a wide variety of high energy X-ray phenomena in all-encompassing astronomical objects, e.g., the very hot regions of

[15] http://chandra.si.edu/about/science_instruments.html
[16] http://cxc.cfa.harvard.edu/cdo/about_chandra/#ACIS

the universe from the exploded stars, the giant clouds of super hot gas that surround galaxy clusters, and the matter around black holes (Weisskopf et al., 2002).

ACIS imaging processing

The *Chandra* data reduction and spectra extraction are performed using CIAO (*Chandra* Interactive Analysis of Observations; current version 4.9[17]) tool and the *Chandra* Calibration Database (CALDB, current version 4.7.6[18]). We perform the spectral analysis with *Sherpa*[19]. Below is an overview of the *Chandra* spectral analysis, and the practical applications are illustrated in Section 3.2.

i. Use the script *download_chandra_obsid* to download public *Chandra* data by ObsId from the *Chandra* archive.

ii. Reprocess the data with *chandra_repro* to ensure that the latest calibration products have been used.

iii. Astrometric corrections are needed to get best possible source positions in the case of multiple observations.

iv. Use *specextract* to extract source and background spectra and build the proper Response Matrix Files (RMFs) and Ancillary Response Files (ARFs).

v. Fit ACIS spectral data with *Sherpa*.

Pileup is a phenomenon of two or more photon events overlapping in a single detector frame and being read as a single event with the wrong energy. It is inherent to CCD detectors. The observations are not affected by pileup if the source is faint enough and the observation is short enough. For sufficiently bright sources, pileup leads to a visible "hole" in the source image. Thus, the effects of the pileup can lead to the loss of spectral information and are unnegligible. A solution to the pileup problem is proposed in paper Davis (2001), and the pileup model included in *Sherpa* is used to fit the spectra with heavy pileup contamination[20].

[17] http://cxc.harvard.edu/ciao/download/
[18] http://cxc.harvard.edu/ciao/download/caldb.html
[19] http://cxc.harvard.edu/sherpa/threads/index.html
[20] http://cxc.harvard.edu/sherpa/ahelp/jdpileup.html

1.4.4 *NuSTAR* and data processing

NuSTAR telescope and performance

The Nuclear Spectroscopic Telescope Array (*NuSTAR*) mission, launched in June 13, 2012, is the first focusing hard X-ray telescope in orbit (Harrison et al., 2013). *NuSTAR* consists of two co-aligned telescope modules with corresponding focal plane modules termed FPMA and FPMB, both operating in the energy range from 3 to 79 keV. So far, *NuSTAR* has the best angular resolution and sensitivity beyond ~ 10 keV. *NuSTAR* has an angular resolution of 18″(FWHM) and a half-power diameter (diameter of a circle enclosing half of the X-ray counts from a point source) of 58″. The FOV is 10′at 10 keV and 6′at 68 keV. The effective area is about 700 cm^2 at 5 keV, 800 cm^2 at 10 keV, and 60 cm^2 at 79 keV. The flux sensitivity is $2 \times 10^{-15} erg/cm^2/s$ in the 6-10 keV range and $1 \times 10^{-14} erg/cm^2/s$ in the 10-30 keV range.[21] *NuSTAR* is aimed at studying objects such as black holes, supernovae, and extremely active galaxies.[22]

NuSTAR data processing

The *NuSTAR* data reduction and spectra extraction are performed using the HEASoft[23], which includes the *NuSTAR* Data Analysis Software (NuSTARDAS) and corresponding *NuSTAR* CALDB. Generally, the fitting package XSPEC[24] or *Sherpa* is used to perform the spectral analysis. Below are the main processing steps:

i. Download the *NuSTAR* observation(s) from `http://heasarc.gsfc.nasa.gov/FTP/nustar/data/obs/`.

ii. Calibrate and screen the primary event files by running the *nupipeline* script.

iii. Use *nuproducts* to generate the high-level data products, e.g., the energy spectra, the RMF and ARF files for spectral analysis, the corrected source and background light-curves, and the sky images.

iv. Fit the *NuSTAR* spectra using *Sherpa*.

[21] `https://heasarc.gsfc.nasa.gov/docs/nustar/nustar_tech_desc.html`
[22] `https://www.nustar.caltech.edu/page/education_outreach`
[23] `https://heasarc.nasa.gov/lheasoft/download.html`
[24] `https://heasarc.gsfc.nasa.gov/xanadu/xspec/`

2

Giant Lobes of Centaurus A as Seen in Radio and γ-ray Images Obtained with *Fermi*-LAT and *Planck* Satellites

2.1 Introduction and Motivation

Centaurus A (Cen A) is a Fanaroff-Riley type I (FR I) radio galaxy that is hosted by the massive elliptical galaxy NGC 5128 (see Israel, 1998). It is the closest radio galaxy located at a distance of 3.8 ± 0.1 Mpc (Harris et al., 2010, $1' \simeq 1.14$kpc). Cen A contains a central black hole with a mass of $(5.5 \pm 3.0) \times 10^7$ $M_\odot$ (Cappellari et al., 2009). The dynamical age of the galaxy is $\sim 0.5 - 1.5$ Gyr (Wykes et al., 2013, 2014; Eilek, 2014). At radio frequencies, a pair of giant lobes are visible, extending from the core to the north and south with an angular size of $\sim 10^\circ$ (~ 600 kpc in projection) (Shain, 1958; Burns et al., 1983); Because of its unique proximity and complex morphology, the giant lobes have been extensively studied in both radio (e.g. Combi & Romero, 1997; Stefan et al., 2013; Alvarez et al., 2000; Hardcastle et al., 2009; McKinley et al., 2013) and γ-ray bands (e.g. Abdo et al., 2010b; Yang et al., 2012).

The high energy γ-ray emission in the outer lobes is believed to be produced through the inverse Compton (IC) channel, when the relativistic electrons upscatter low energy background photons, including the cosmic microwave background (CMB) and ubiquitous extragalactic background light (EBL), to MeV-GeV energies (Abdo et al., 2010b; Yang et al., 2012). This provides an unique opportunity to map the spatial and energy distribution of relativistic electrons in this source. Furthermore, by comparing the radio/microwave and γ-ray emissions, we can obtain unambiguous information on the magnetic fields.

Owing to the accumulative photon statistics and the recently improved software tools of *Fermi*-LAT, we can extend the original analysis of Yang et al. (2012) to lower and higher energies and investigate the spatial variation of

γ-ray spectra. In such low magnetic field ($\sim$ uG) the electrons that produce GeV γ-rays via IC scattering, have much higher energies than those which produce radio/microwave radiation via synchrotron radiation. The *Planck* satellite provides high sensitivity data with full sky coverage extending from 30 GHz to 853 GHz. These frequencies minimise the energy gap between the two electron populations responsible for radio and γ-rays emissions.

In this chapter, we present a detailed analysis of the broadband emission of the lobes of Cen A using γ-ray data from *Fermi*-LAT and microwave data from *Planck*. In Section 2.2, we perform the analysis of *Fermi*-LAT data. In Section 2.3, we analyse the MHz-range data from radio telescopes and microwave data from *Planck*. In Section 3.3, we fit the broadband spectral energy distributions (SEDs) of the lobes within a pure leptonic and more complex leptonic+hadronic models. We discuss the results in Section 3.4.

2.2 *Fermi*-LAT Data Analysis

The analysis of this section includes the *Fermi*-LAT data from the directions of the two giant radio lobes. We selected observations from August 4, 2008 (MET 239557417) until June 27, 2015 (MET 457063584) and used photons in the energy range between 60 MeV and 30 GeV. A $14^\circ \times 14^\circ$ square region centred at the location of Cen A (RA = $201^\circ 21' 54''$, Dec = $-43^\circ 1' 9''$) was selected as the region of interest (ROI). We selected both the front and back converted photons. To reduce the background contamination from the Earth's albedo, the events from directions $> 90^\circ$ were excluded from the analysis. We adopted the version P8R2_SOURCE_V6 of the instrument response function (IRF) provided by the *Fermi*-LAT collaboration. The binned likelihood analysis implemented in science tool *gtlike* was used to evaluate the spectrum.

To define the initial source list, we use the four-year catalogue (3FGL) (Acero et al., 2015) by running the make3FGLxml script[1]. In the initial list, the spectral parameters of point-like sources within the ROI are left as free parameters. Also, we use the default spatial template for giant lobes provided by the Fermi collaboration. We use the models of Galactic diffuse and isotropic emission provided by the *Fermi* team[2] for the foreground components. In the fitting, the normalisations of both components are left as free parameters.

[1] http://fermi.gsfc.nasa.gov/ssc/data/analysis/user/make3FGLxml.py
[2] http://fermi.gsfc.nasa.gov/ssc/data/access/lat/BackgroundModels.html

Table 2.1: TS value and likelihood value for the three templates used in 2.2.1.

Model	Core	North lobe	South lobe	-log(Likelihood)
T1	7147	459	1591	42104
T2	6195	377	1610	42156
T3	5881	337	1566	42184

2.2.1 Spatial analysis

For morphology studies, we also build our own templates directly from the γ-ray residual maps. We apply *gtlike* with the initial source list and derive a fitted model. Then we produce the residual maps by removing the contributions from the diffuse background and all catalogue sources except the giant lobes. We also mask the inner 1° nucleus of Cen A to prevent the contamination from that region. Finally, we divide the residual maps into north and south lobes. Generally speaking, high energy maps with higher angular resolution are more suitable for the spatial analysis, but low statistics in the higher energy range may prevent any improvement. To address this problem, we apply the procedure described above to the energy range $>$ 1000 MeV and $>$ 100 MeV, respectively. The resulting spatial templates are labelled as T1 ($>$ 1000 MeV) and T2 ($>$ 100 MeV).

We use the residual templates T1 and T2, as well as the default spatial templates provided by the *Fermi* team[3] (T3), to model the giant lobes, and apply *gtlike* to three models in the energy range above 100 MeV. The resulting TS and -log(Likelihood) values are listed in table 2.1. In the case of template T1, the core of Cen A is clearly visible with a test statistic of TS $>$ 7000, corresponding to a detection significance of 84σ. Extended emission to the north and south of the lobes of Cen A is detected with significances of TS $>$ 450 (21σ) and TS $>$ 1500 (39σ), respectively. The -log(Likelihood) for T1 is significantly smaller than that of T2 and T3. Therefore, for our analysis, we select template T1. The *Fermi*-LAT counts map produced for the $>$ 1000 MeV data set, is shown in Figure 2.1(a); the green crosses show the position of point-like sources from the 3FGL catalogue within the ROI. The corresponding residual image (template T1) is shown in Figure 2.1(b). For comparison, the Planck 30 GHz lobe contours (green contours) are also plotted in the image. It can be seen that both the north and south lobes of the HE γ-ray emission extend beyond the radio lobes.

[3] http://fermi.gsfc.nasa.gov/ssc/data/analysis/scitools/extended/extended.html

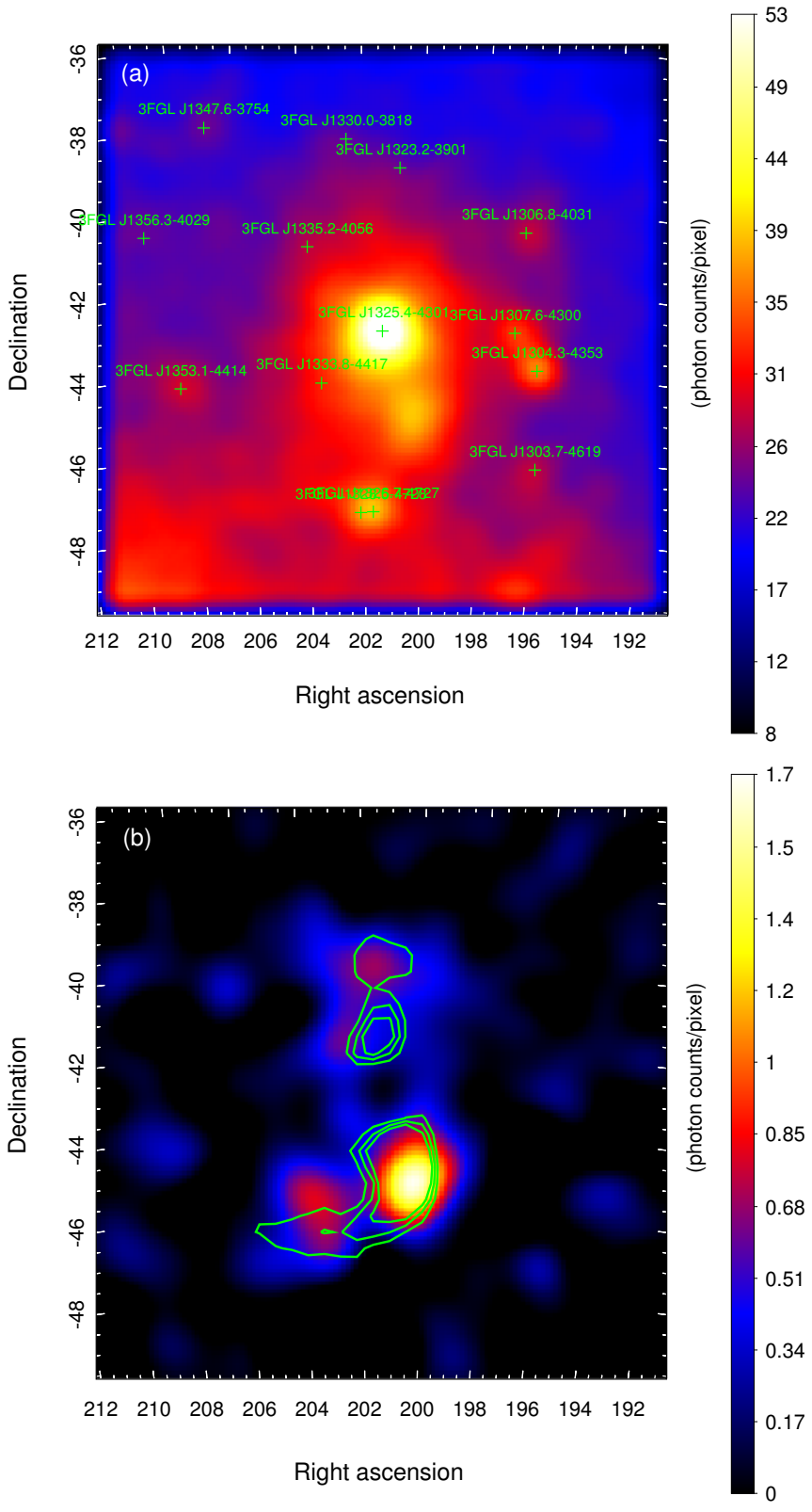

Figure 2.1: (a) LAT counts map of the $14^\circ \times 14^\circ$ ROI. The counts map is smoothed with a Gaussian of kernel 0.7°. The green crosses indicate the position of the point-like sources within 7° of Cen A. (b) Residual maps of lobes after subtracting the diffuse background, the point-like sources, and the Cen A core. The green contours indicate Planck 30 GHz lobe contours.

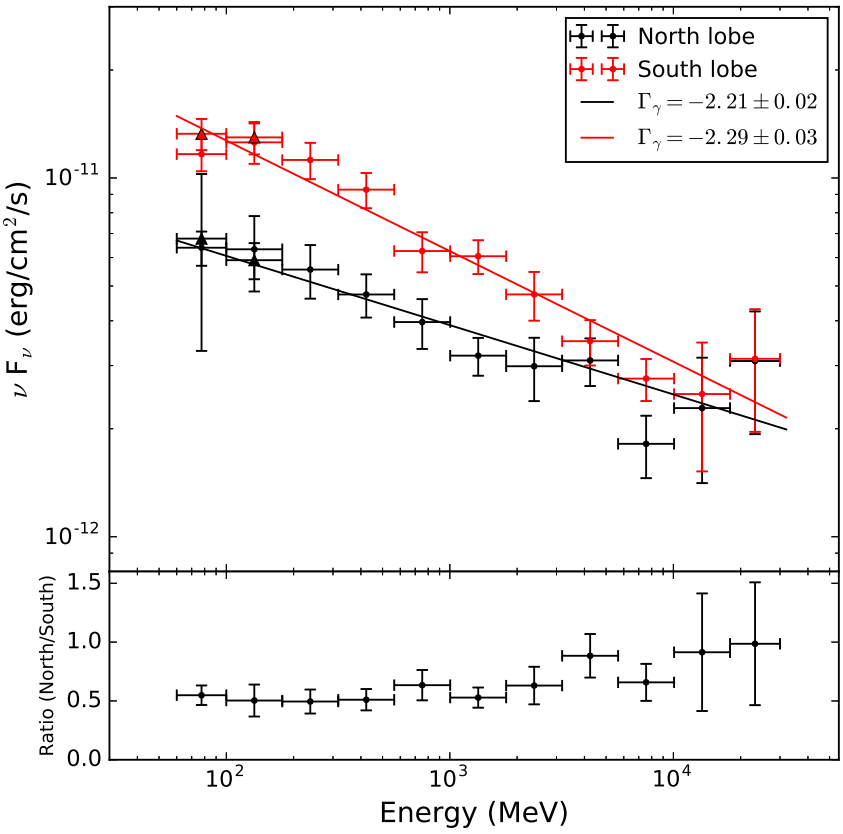

Figure 2.2: Derived SEDs of the north lobe and south lobe, with power-law fits. The corresponding photon indices are Γ_N and Γ_S. The ratio of the north and south fluxes is shown in the bottom panel. For the first two energy bins, the SEDs derived using a larger ROI are also shown as bold triangles.

2.2.2 Spectral analysis

To derive the SED, we divide the energy interval between 100 MeV and 30 GeV into ten equal bins in logarithmic space and use *gtlike* in each bin. To extend the spectral analysis to lower energies, we also include photons with energy between 60 MeV and 100 MeV, and regard these as the first energy bin. We apply energy dispersion correction to this energy bin. The significance of the signal detection in each energy bin exceeds TS = 8 ($\sim 3\sigma$). The SEDs fitted with a power law are shown in Figure 2.2. Correspondingly, the photon indices of the north and south lobes are (2.21 ± 0.02) and (2.29 ± 0.03), respectively. Within uncertainties, the index of the north lobe is consistent with that in Yang et al. (2012), while the index of the south lobe is slightly smaller. The integral flux above 100 MeV is $(0.54 \pm 0.06) \times 10^{-7}$ ph cm^{-2} s^{-1} for

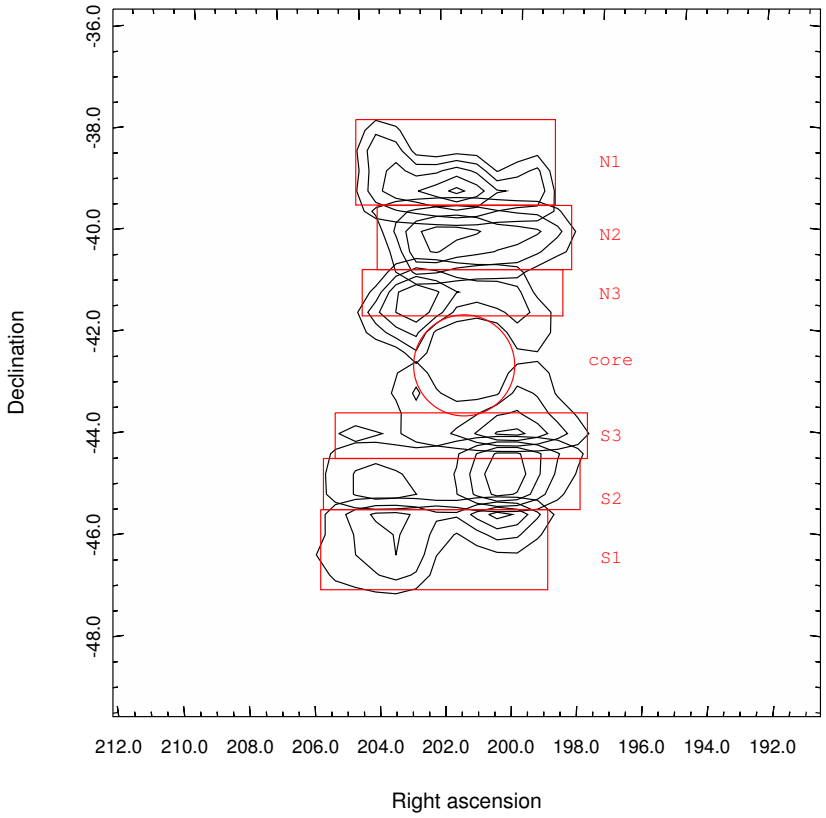

Figure 2.3: Spectral extraction regions used for Figure 2.4. The contour levels correspond to the γ-ray image (>1000 MeV). The red lines indicate the regions of the radio and *Planck* aperture photometry. The contours inside the corresponding regions show the template used for the extraction of the corresponding LAT spectrum. N1, N2, and N3 are the outer, middle, and inner regions of the north lobe, and S1, S2, and S3 are the outer, middle, and inner regions of the south lobe. The circle is the core region.

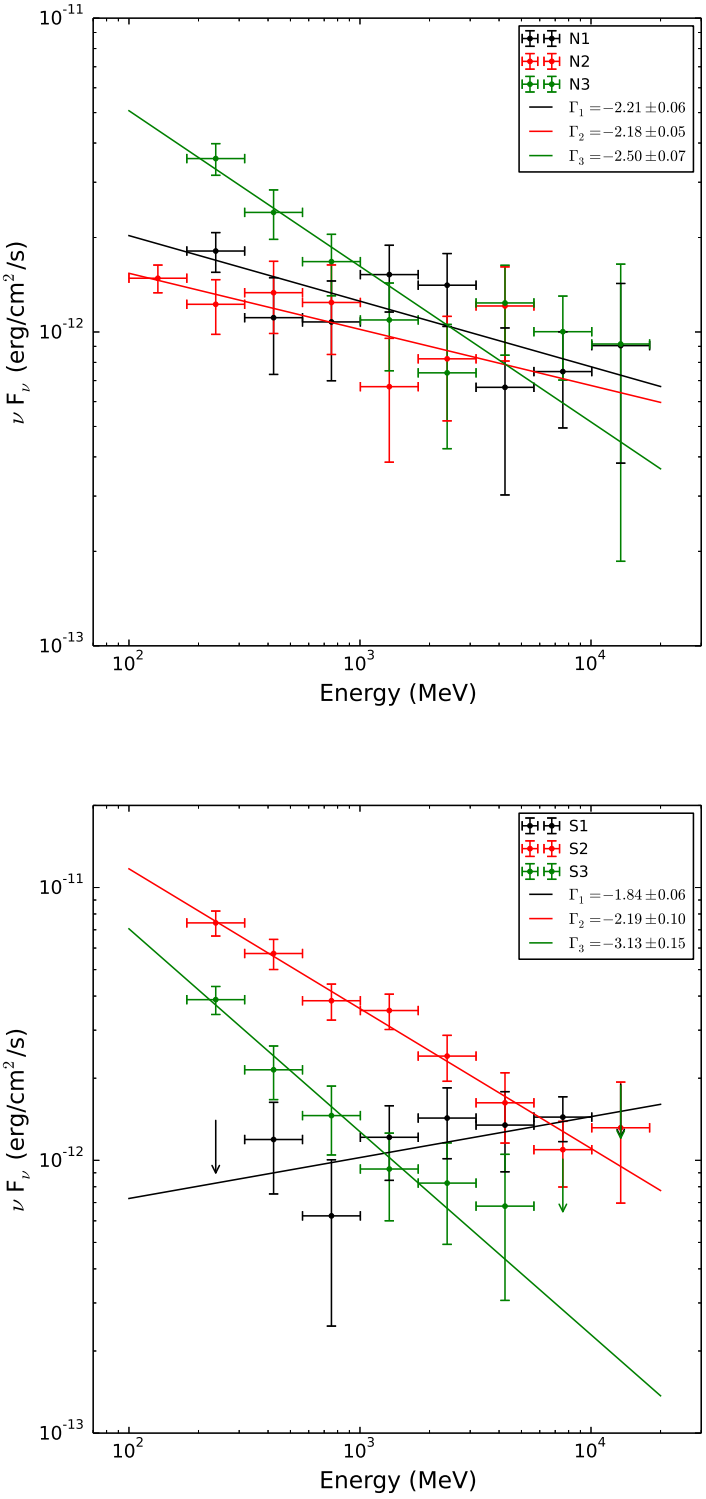

Figure 2.4: Top plot shows the SEDs of the slices in the north lobe. The bottom plot shows the SEDs of the slices in the south lobe. The solid lines indicate the power-law fits. Γ_1, Γ_2, and Γ_3 are the corresponding photon indices.

the north lobe and $(1.22 \pm 0.05) \times 10^{-7}$ ph cm^{-2} s^{-1} for the south lobe.

At low energy, the point spread function (PSF) of Fermi can be as large as 5°, in which case the $14° \times 14°$ ROI used here may be not sufficient. We refit the first two energy bins using a $20° \times 20°$ ROI to see the influence of the limited ROI. These results are also shown in Figure 2.2 and are consistent with those derived from the smaller ROI.

To test the possible spectral variations from the outer regions of the lobes towards the central core, we split each lobe of template T1 into three parts. These regions are shown in Figure 2.3. The contour levels derived from the *Fermi*-LAT γ-ray image (>1000 MeV), are used for the spectral extraction and the red rectangles are used for the radio and Planck data aperture photometry. The outer, middle and inner regions of the north lobe are N1, N2 and N3, respectively, and S1, S2 and S3 are the outer, middle and inner regions of the south lobe, respectively. The circle is the core region.

We derive the SEDs (see Figure 2.4) for every slice and an upper limit is calculated within 3σ confidence level for the signal that is detected with a significance of less than 2σ. We use a power-law function to fit the observed data. The upper limits in SEDs are also used to constrain the parameters of the power-law function. As shown in Figure 2.4, in the north lobe N1 and N2 are consistent with each other within the uncertainties, but N3 is steeper than N1 and N2. In the south lobe, the photon indices for the three slices differ: the spectra become harder moving away from the core.

2.3 Radio and *Planck* Data Reduction

2.3.1 Radio data

We use 118 MHz MWA data (McKinley et al., 2013), 408 MHz Haslem data (Haslam et al., 1982), and 1400 MHz Parkes data (O'Sullivan et al., 2013). The flux densities are measured using aperture photometry over the same subregions as the *Planck* data (red rectangles shown in Figure 2.3). We use a ds9 plug-in *radio flux measurement*[4] to measure the flux densities for each region and frequency. The results are listed in table 2.3.

2.3.2 *Planck* data

We use the *Planck* full-mission maps from Public Data Release 2 (PR2) products, which can be obtained via the *Planck* Legacy Archive (PLA) interface[5]. The *Planck* all-sky maps are in Healpix (Górski et al., 2005) format, with

[4] http://www.extragalactic.info/~mjh/radio-flux.html
[5] http://pla.esac.esa.int/pla

the resolution parameter $N_{\rm side} = 1024$ for LFI 30, 44 and 70 GHz, and 2048 for LFI 70 GHz and HFI 100 – 857 GHz. The data are given in units of CMB thermodynamic temperature ($K_{\rm CMB}$) up to 353 GHz, and in MJy sr^{-1} for 545 and 857 GHz. The temperature units and MJy sr^{-1} are converted to flux density per pixel with multiplication by the factor given in the last column of table 2.2, the derivations of the conversion factors are in Appendix A. For ease of comparison with γ-ray emission, we degrade the resolution of the original Healpix data from 1024 or 2048 into 512 (a pixel size of about 6′), and then project them on to the area with *Fermi*-LAT's sky map using the Healpy package[6] and Astropy package[7]. Both calibration and systematic uncertainties are considered. The zodiacal light level corrections are added to the maps, and the cosmic infrared backgrounds (CIB) are removed from the maps (Planck Collaboration et al., 2016a). The characteristics of *Planck* for each frequency band are listed in table 2.2.

[6] https://healpy.readthedocs.org/en/latest/tutorial.html
[7] http://docs.astropy.org/en/stable/index.html#

Table 2.2: *Planck* characteristics of full mission maps.

Frequency [GHz]	Beam FWHM [arcmin]	Calibration error [%]	Systematic error [μK_{CMB}]	CIB correction [MJy/sr]	Zodiacal light correction [MJy/sr]	Units factor [Jy/pix]
30	32.29	0.35	0.19	-	-	107.90
44	27.00	0.26	0.39	-	-	226.02
70	13.21	0.20	0.40	-	-	530.61
100	9.68	0.09	-	0.003	1.03e-4	953.87
143	7.30	0.07	-	0.0079	3.57e-4	1518.00
217	5.02	0.16	-	0.033	1.84e-3	1933.37
353	4.94	0.78	-	0.13	0.01	1187.18
545	4.83	5.00	-	0.35	0.04	3.99
857	4.64	5.00	-	0.64	0.12	3.99

The beams and the values used for *Planck* original data corrections are all taken from Planck Collaboration et al. (2016a).

Table 2.3: Flux density measurements of the regions of Cen A at low frequencies. Blanks indicate the signal that was not detected in that region.

Frequency	Flux density [Jy]						
[GHz]	N1	N2	N3	core	S1	S2	S3
0.118[a]	362.65±48.26	517.63±61.86	620.58±70.84	2877.38±295.91	479.99±60.31	849.74±95.37	764.29±86.30
0.408[a]	165.07±18.78	265.98±28.95	291.83±31.21	1103.06±112.19	368.12±39.64	495.86±52.01	382.24±40.48
1.4[b]	72.25±1.55	97.56±2.04	107.22±2.22	483.45±9.74	81.13±1.73	163.92±3.37	162.55±3.34
30	9.63±0.01	11.19±0.01	12.41±0.01	82.48±0.01	9.29±0.01	19.26±0.01	24.36±0.01
44	5.43±0.03	8.03±0.03	8.67±0.02	55.09±0.02	-	10.82±0.03	16.63±0.02
70	2.37±0.07	11.70±0.06	7.92±0.05	39.89±0.05	-	15.67±0.06	12.58±0.05
100	-	4.45±0.05	-	23.21±0.03	-	9.11±0.04	-
143	-	-	-	9.16±0.04	-	3.92±0.04	-

[a] 10% of the flux is considered as systematic error.
[b] 2% of the flux is considered as systematic error.

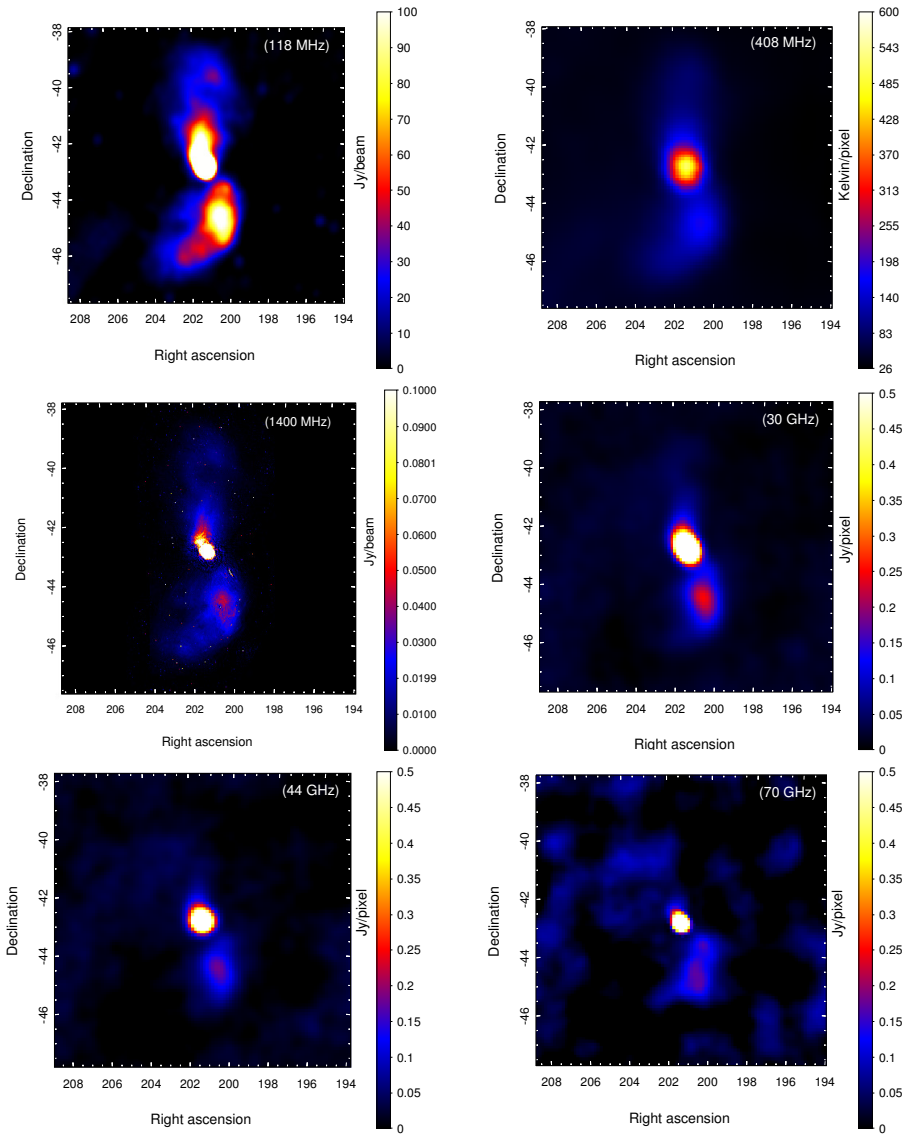

Figure 2.5: From top left to bottom right: radio/microwave images of the Cen A and surrounding field at 118, 408, 1400 MHz, 30, 44, 70, 100, and 143 GHz. The *Planck* maps are *cleaned maps*, which are used to measure the flux densities (see subsection 2.3.3 in details). These images are smoothed using a Gaussian kernel 0.3°.

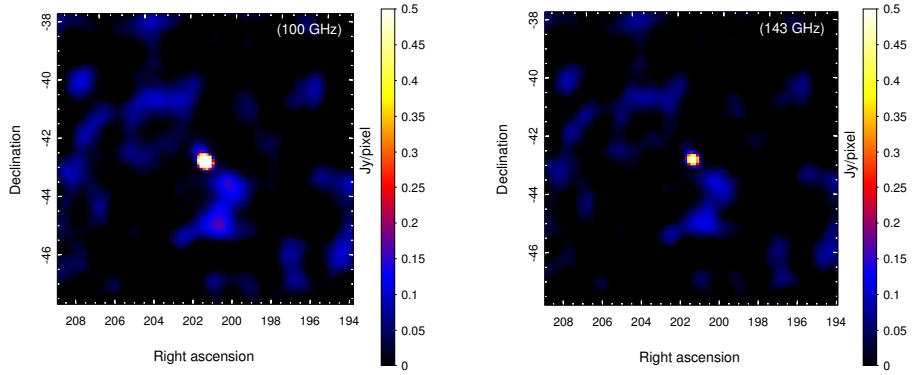

Figure 2.5 — continued

2.3.3 Thermal dust and CMB components separation

In our ROI, synchrotron radiation dominates in the low frequency band. However, in the high frequency bands (> 100 GHz) CMB and thermal dust emission begin to overwhelm the non-thermal emission (Planck Collaboration et al., 2016b). It is possible to use higher frequency maps to derive accurate information on CMB anisotropy and thermal dust emission, with which we can get more robust non-thermal spectra in lower frequency than a simple aperture photometry method.

Thermal emission from dust grains dominates the radiation mechanism in the far-infrared (FIR) to millimetre range (e.g. Draine (2003); Draine & Li (2007); Compiègne et al. (2011)), and is the main foreground hampering the study of Cen A at *Planck* frequencies. We selected a modified blackbody (MBB) (Planck Collaboration et al., 2014a) to fit the thermal dust component empirically, that is

$$I_{\rm d} = A_{\rm d} B_\nu (T_{\rm obs}) \left(\frac{\nu}{\nu_0}\right)^{\beta_{\rm obs}}, \tag{2.1}$$

where $\nu_0 = 353$ GHz is the reference frequency. There are three parameters in this model: the dimensionless amplitude parameter $A_{\rm d}$, temperature $T_{\rm obs}$, and the spectral index $\beta_{\rm obs}$. Because there are only a few frequency bands available, in the fitting we leave $A_{\rm d}$ and $T_{\rm obs}$ to be free and fix the index $\beta_{\rm obs}$ to be the value in the Planck all-sky model of thermal dust emission (Planck Collaboration et al., 2014a) from PLA.

Another foreground is the CMB. A blackbody with the $T_{\rm CMB} = 2.7255$ K (Fixsen, 2009) is selected to fit the CMB component

$$I_{\rm CMB} = A_{\rm CMB} B_\nu (T_{\rm CMB}), \tag{2.2}$$

where $A_{\rm CMB}$ is a dimensionless amplitude parameter.

In order to derive the emission signals of Cen A in the low energy band from 30 to 143 GHz accurately, we use the *Planck* 217, 353, 545, and 857 GHz, and IRAS 3000 GHz (100 μm) data to constrain the parameters $A_{\rm d}$, $T_{\rm obs}$, and $A_{\rm CMB}$ at each pixel using a chi-squared (χ^2) minimisation, and then extrapolate the two models to low energy. Here we manipulate the 100 μm data following the method described in Planck Collaboration et al. (2014a).

Considering the effects of both the parameter uncertainties of the models (CMB and thermal dust) and the errors of the observed *Planck* data, we perform the following steps in deriving the microwave flux and errors of the lobes. (1) For any pixel within the ROI, we draw 50 groups of random samples from a normal (Gaussian) distribution for the free parameter set ($A_{\rm CMB}$, $A_{\rm d}$, and $T_{\rm obs}$) according to the best-fitted value and fitted uncertainties. The same procedure is also applied to the observed *Planck* data in each pixel. The observed uncertainties should obey a Poisson distribution rather than a Gaussian, but the large counts of the Planck maps makes Gaussian statistics a reasonable assumption. (2) For each group of samples, we calculate the thermal dust and CMB components based on equation 2.1 and equation 2.2, respectively. The thermal dust and CMB maps are both smoothed to the *Planck* original angular resolution (listed in Table table 2.2) to obtain a matched resolution map. Then we remove the CMB and thermal dust component to derive the *background subtracted* value of this pixel in each sample. (3) We choose the average and standard deviation of the 50 sampled *background subtracted* values as the final *cleaned* value and corresponding errors in this pixel. (4) We repeat steps (1) to (3) at each pixel within the ROI, and finally derive the CMB and dust emission subtracted *cleaned* maps and corresponding error maps, which are used to measure the integral flux densities in the following. The derived *cleaned* maps from 30 GHz to 143 GHz are shown in Figure 2.5.

2.3.4 Flux density measurements

We use the standard aperture photometry, with the aperture size (red rectangles) shown in Figure 2.3, to measure the integral flux densities of the *Planck* 30, 44, 70, 100, and 143 GHz maps. The measurements of flux density for each region and frequency, together with errors within 1σ confidence level, are listed in Table 3. The errors are derived from the error maps described above using error propagation.[8] The flux densities of the core are consistent

[8] Let function $y_2 = \frac{y_0}{y_1}$, y_0 and y_1 are two independent variables with the corresponding errors σ_0 and σ_1. Then the uncertainty σ_2 of the function y_2 depends on σ_0 and σ_1: $\sigma_2 = \sqrt{\left(\frac{\partial y_2}{\partial y_0}\right)^2 \sigma_0^2 + \left(\frac{\partial y_2}{\partial y_1}\right)^2 \sigma_1^2} = \sqrt{\left(\frac{\sigma_0}{y_1}\right)^2 + \left(\frac{y_0 \sigma_1}{y_1^2}\right)^2}$

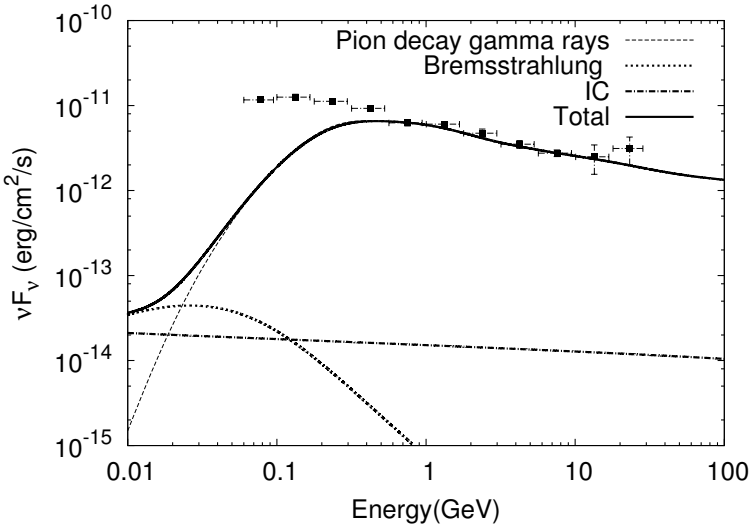

Figure 2.6: γ-rays from hadronic interactions of cosmic rays in different channels. Also shown is the SED of the south lobe. The primary proton spectra are assumed to be a power-law function with an index of 2.3 to fit the high energy part of the SED of the south lobe.

with their corresponding values of region 3 in Hardcastle et al. (2009), which confirm that our model selection and method are reasonable.

2.4 Modelling the Spectral Energy Distributions

To fit the derived spectral distributions, we use the software package *Naima*[9]. We find that the power-law shape of the spectrum extends down to 100 MeV. This does not agree with the spectrum of low energy γ-rays from hadronic interactions of cosmic rays. The latter has a standard shape, which is dictated by the kinematics of the π^0 decay rather than the spectrum of cosmic rays. The region of sharp decline of the SED of π^0-decay γ-rays below 1 GeV is partly "filled" by photons generated by secondary electrons (through the IC scattering and Bremsstrahlung), that are the products of the charged $\pi^\pm$-meson decays. However, these components do not appear to sufficiently compensate the deficit even in the most optimistic case of a "thick target" when the production of secondaries is saturated. This is demonstrated in Fig.2.6, which shows the three channels of γ-ray production initiated by pp interactions and the SED of south lobe. It is assumed that the density of the ambient gas n is sufficiently high that the lifetimes of relativistic protons, $t_{\rm pp} \sim 10^{15} \left(\frac{n}{1\ {\rm cm}^{-3}}\right)^{-1}$ s, as well as secondary electrons, are shorter than the confinement time of cosmic rays. Under this condition, the steady-state

[9] http://naima.readthedocs.org/en/latest/index.html#

solutions shown in Figure 2.6 apparently do not depend on the density n. The relative contribution of γ-rays from secondary electrons does not strongly depend on the spectrum of cosmic rays. We can safely conclude that the low energy γ-rays from both lobes are not contributed by cosmic ray protons and nuclei.

Thus, the spectral measurements presented in this work remove the uncertainty of the previous study, Yang et al. (2012), regarding the origin of γ-rays. It is clear that γ-rays are produced, at least in the energy band below 1 GeV, by directly accelerated electrons. Because of the low gas density in the lobes, the γ-ray production is dominated by the IC scatterings of photons of the 2.7 K CMB radiation, with possible contribution from photons of the EBL by relativistic electrons. Although the energy density of the EBL is much lower than the energy density of the CMB, the role of the EBL photons can be noticeable in the formation of the spectrum at the highest γ-ray energies, especially in the case of a cutoff in the electron spectrum below a few TeV. The photons from the host galaxy of Cen A are also potential seed photons for IC scattering. As calculated in Abdo et al. (2010b), however, the IC gamma rays from the photon fields produced by the host galaxy are negligible compared with those from the CMB and EBL.

For different parts of the lobes, the distributions of electrons and the strength of the magnetic fields can be derived from the fit of the *Planck*, radio, and *Fermi*-LAT γ-ray data by synchrotron and IC components, respectively. We use the formalism of Aharonian et al. (2010) for the calculations of synchrotron radiation and the formalism proposed in Khangulyan et al. (2014) for IC scattering. The temperature $T_{\rm CMB} = 2.7255$ K and energy density $n_{\rm CMB} = 0.261$ eV cm^{-3} are adopted for the CMB photon field. We use the model of Franceschini et al. (2008) for the EBL.

For the energy distribution of electrons, we assume the following general form:

$$N(E) = A \left(\frac{E}{E_0}\right)^{-\alpha} \exp(-\left(\frac{E}{E_{\rm cutoff}}\right)^{\beta}). \tag{2.3}$$

Here $E_0 = 1$ GeV is the reference energy. In calculations, the parameters A, α, $E_{\rm cutoff}$, and β, characterising the electron spectrum, and the strength of the magnetic field B, are left as free parameters. The minimum electron energy is set to $E_{\rm emin} = 1$ MeV. Figure 2.7 shows the SED results obtained for the subregions from Figure 2.3. The derived model parameters $E_{\rm cutoff}$, β, B, and the corresponding errors with 1σ confidence level, as well as the total energy of electrons $W_{\rm e}$, are presented in table 2.4 for the regions N1,N2, N3 and S1, S2, S3. It should be mentioned that for N2, N3, S2, and S3, the *Planck* data points above 70 GHz are significantly above the model predicted value and we omit these points in the fit. The reason may be a poor understanding of

Table 2.4: Summary of SED best-fitting model parameters for the power-law electron distribution with cutoff.

Model components	N1	N2	N3	S1	S2	S3
W_e [$\times 10^{57}$ erg]	0.98±0.08	1.8±0.3	$0.67^{+0.07}_{-0.05}$	0.18±0.03	2.5±1.5	$1.0^{+0.3}_{-0.2}$
α	1.65±0.03	$2.02^{+0.06}_{-0.07}$	1.79±0.04	2.42±0.02	$1.96^{+0.07}_{-0.14}$	1.78±0.07
$E_{\rm cutoff}$ [GeV]	65.5±1.8	59±6	21.2±1.9	-	5.0±0.4	$38.9^{+3.0}_{-1.8}$
β	20±2	1.9±0.2	0.68±0.02	-	$0.42^{+0.05}_{-0.02}$	$1.02^{+0.07}_{-0.05}$
B [μG]	0.70±0.04	1.26±0.08	$1.78^{+0.07}_{-0.11}$	13.4±0.8	$2.29^{+0.17}_{-0.12}$	1.74±0.07

Table 2.5: Summary of SED best-fit model parameters for a broken power-law electron distribution.

Model components	N1	N2	N3	S1	S2	S3
W_e [$\times 10^{57}$ erg]	0.63±0.07	$2.7^{+0.8}_{-0.5}$	0.55±0.07	0.18±0.03	$2.8^{+2.0}_{-0.9}$	$1.2^{+0.7}_{-0.4}$
α_1	1.54±0.06	$2.13^{+0.06}_{-0.08}$	$1.92^{+0.05}_{-0.08}$	2.42±0.02	2.08±0.10	1.77±0.14
α_2	$8.5^{+2.0}_{-1.4}$	9±3	3.9±0.2	-	4.18±0.16	$5.5^{+0.4}_{-0.3}$
$E_{\rm break}$ [GeV]	51±4	59^{+8}_{-12}	32±3	-	36±3	44±4
B [μG]	0.79±0.06	1.14±0.09	1.79±0.12	13.4±0.8	1.37±0.08	1.23±0.09

Table 2.6: Summary of SED best-fit parameters in the leptonic+hadronic model.

Model components	N1	N2	N3	S1	S2	S3
W_p [$\times 10^{60}$ erg]	1.04±0.12	0.78±0.11	0.42±0.19	$1.4^{+0.7}_{-0.4}$	$0.19^{+0.14}_{-0.08}$	0.61±0.10
α	2.59±0.12	2.7±0.2	$2.16^{+0.20}_{-0.11}$	2.05±0.12	$2.7^{+0.4}_{-0.3}$	$2.48^{+0.08}_{-0.06}$

the high frequency background in this band. Meanwhile, for N2 and N3 the high Fermi points are significantly above the model curve; this is caused by the fact that the weighting of these high energy points in MCMC fitting is relatively small owing to their larger error bars.

We should note that in this study we find, in contrast to the statement in the paper Yang et al. (2012), that the EBL photons appear important (except for the region S1), as target photons for the IC scattering, to fit the γ-ray data. The reason is that now the additional Planck data provide stringent constraints on the cutoff regions of the electron spectrum.

For all regions, except for S1, the γ-ray spectra correspond to electrons from the post-cutoff region. Meanwhile the radio data are produced by electrons from the pre-cutoff region. This follows from the essentially different indices of the radio and γ-ray spectra. The region S1 is of special interest because of lack of any indication for a cut off in both the radio and γ-ray spectra. In this region, the γ-ray and radio data points can be fitted with a pure power-law electron spectrum up to 1 TeV. Another special feature of this region is that the derived magnetic field is about 10 μG, which is much higher than in other regions. This value exceeds by an order of magnitude the strength of the magnetic field typically assumed for the radio lobes (see e.g. McKinley et al., 2015).

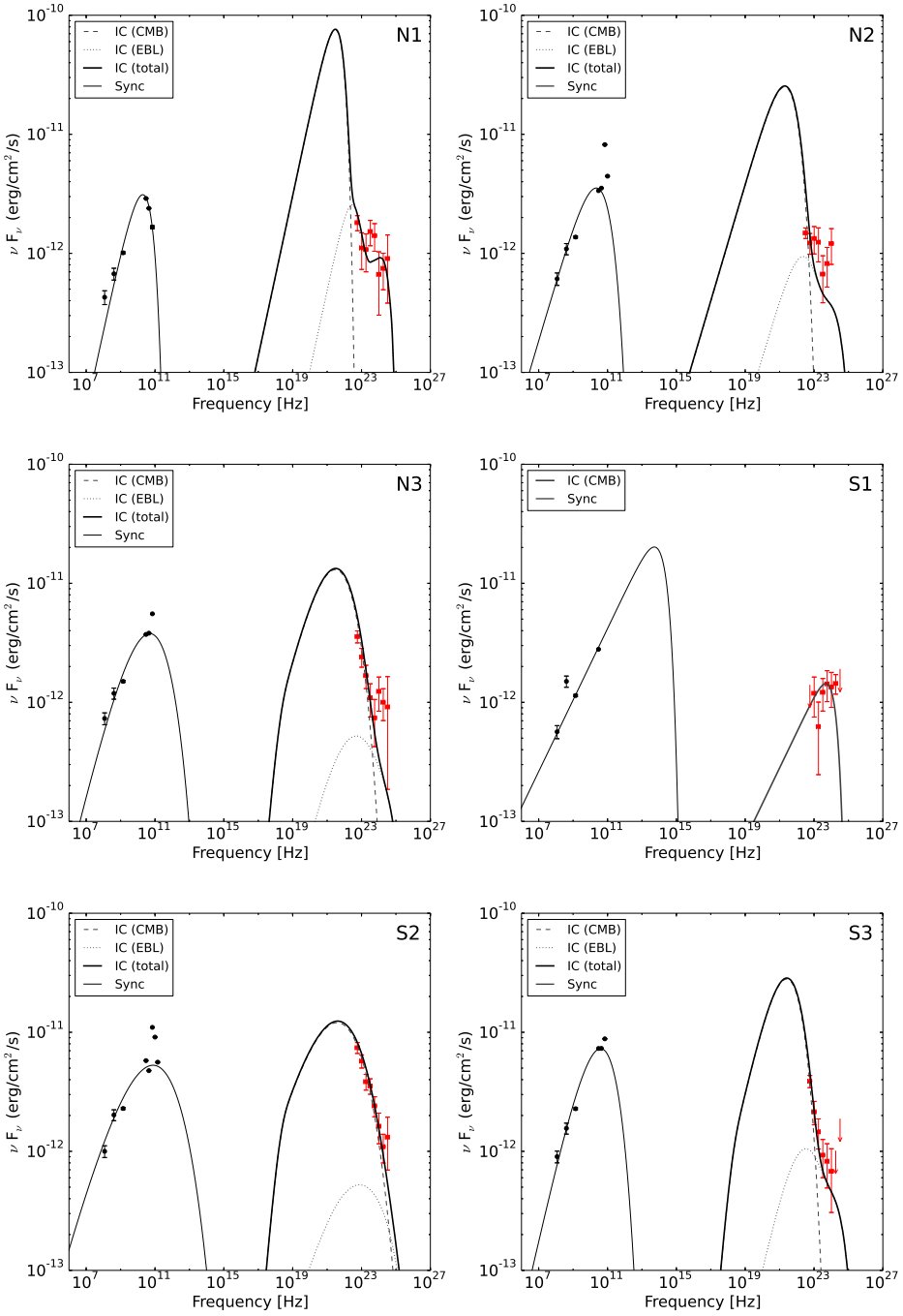

Figure 2.7: Broadband SEDs for each region shown in Figure 2.3. Observed radio and *Planck* data (black dots with error bars) are fitted with a synchrotron model. Observed *Fermi*-LAT data (red dots with error bars) are fitted with the inverse-Compton (IC) scatterings of the CMB and EBL photon fields except for S1, which only requires the seed photon contribution from the CMB. The upper limits are calculated within a 3σ confidence level.

The dynamical ranges of both the radio and γ-ray data points are relatively small, therefore the power-law electron spectrum with a cutoff is not an unique explanation of the data. For example, the broken power-law function, given in the form

$$N(E) = A\,(\frac{E}{E_0})^{-\alpha_1},\ E < E_{\rm break}$$
$$N(E) = A\,(\frac{E}{E_0})^{-\alpha_2}\,(\frac{E_0}{E_{\rm break}})^{\alpha_1-\alpha_2},\ E < E_{\rm break}, \tag{2.4}$$

can fit the radio and γ-ray data equally well. The results are shown in Figure 2.8. The best-fit parameters are summarised in Table 2.5. We don't apply this electron distribution to the region S1 since the latter is explained by a pure power-law spectrum. The differences in the indices before and after the break are significantly larger than 1. This implies that the break cannot be a result of radiative cooling, but rather is a characteristic feature of the acceleration spectrum.

As mentioned above, at low energies, $E \leq 1$ GeV, the γ-ray data can be explained only by directly accelerated electrons. However, we cannot exclude a significant contribution by a hadronic component to the overall γ-ray emission. Moreover, an additional hadronic component helps us to improve the fit of γ-ray spectra. In particular, the hadronic γ-ray emission could be considered as an alternative to the IC scattering on the EBL photons. Such an attempt to fit the radio and γ-ray SEDs successfully, with an involvement of an additional hadronic component, is demonstrated in Figure 2.9. In this case IC scattering from CMB contributes to the low energy part of γ-rays, while the π^0 decays contribute to the high energy tail. This is similar, to some extent, to the modelling of the radio lobes of Fornax A in McKinley et al. (2015), where the X-ray flux is due to the IC scattering, and γ-rays are from the π^0-decays.

To reduce the number of free parameters, in the "IC+π^0" model we fix the magnetic field and electron spectrum to the best-fit values from the pure leptonic models described above. The only exception is the peculiar S1 region, for which we fix the magnetic field to the value of 1μG, i.e. by a factor of 10 smaller than in the pure IC scenarios. We adopt the parametrisation of neutral pion decay described in Kafexhiu et al. (2014) in the π^0 model calculation. We also fix the gas density, $n = 10^{-4}$ cm^{-3}. Then, the remaining two free parameters are the spectral index α, and the total energy in protons, $W_{\rm p}$. The derived values of these parameters are presented in Table 2.6. The power-law indices of the proton spectra in the different regions are similar with an average value close to 2.5. The only exception is the region S1, where the photon spectrum is very hard with $\alpha \sim 2$. The total energy in relativistic

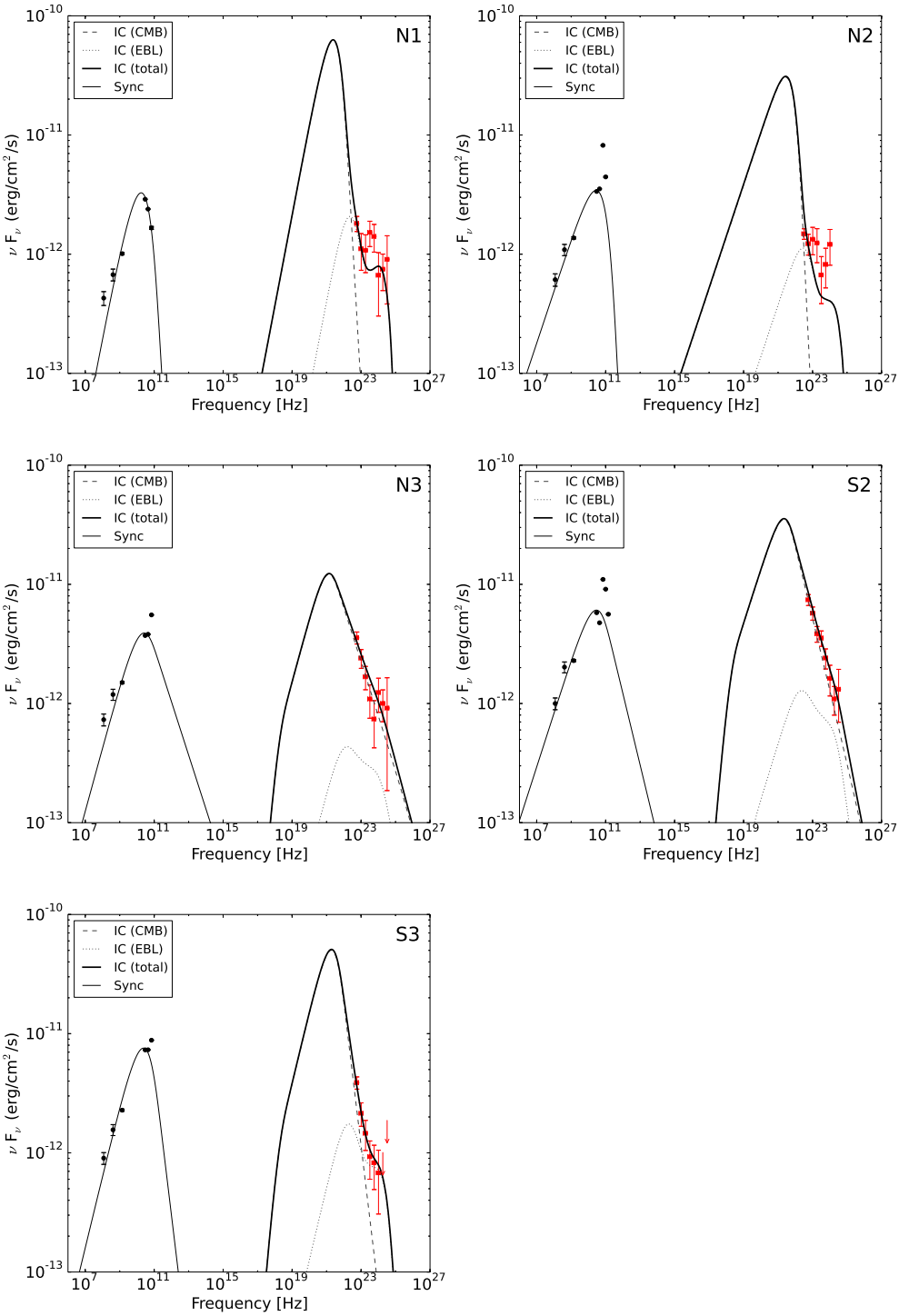

Figure 2.8: Same as Figure 2.7 but for broken power-law electron distributions.

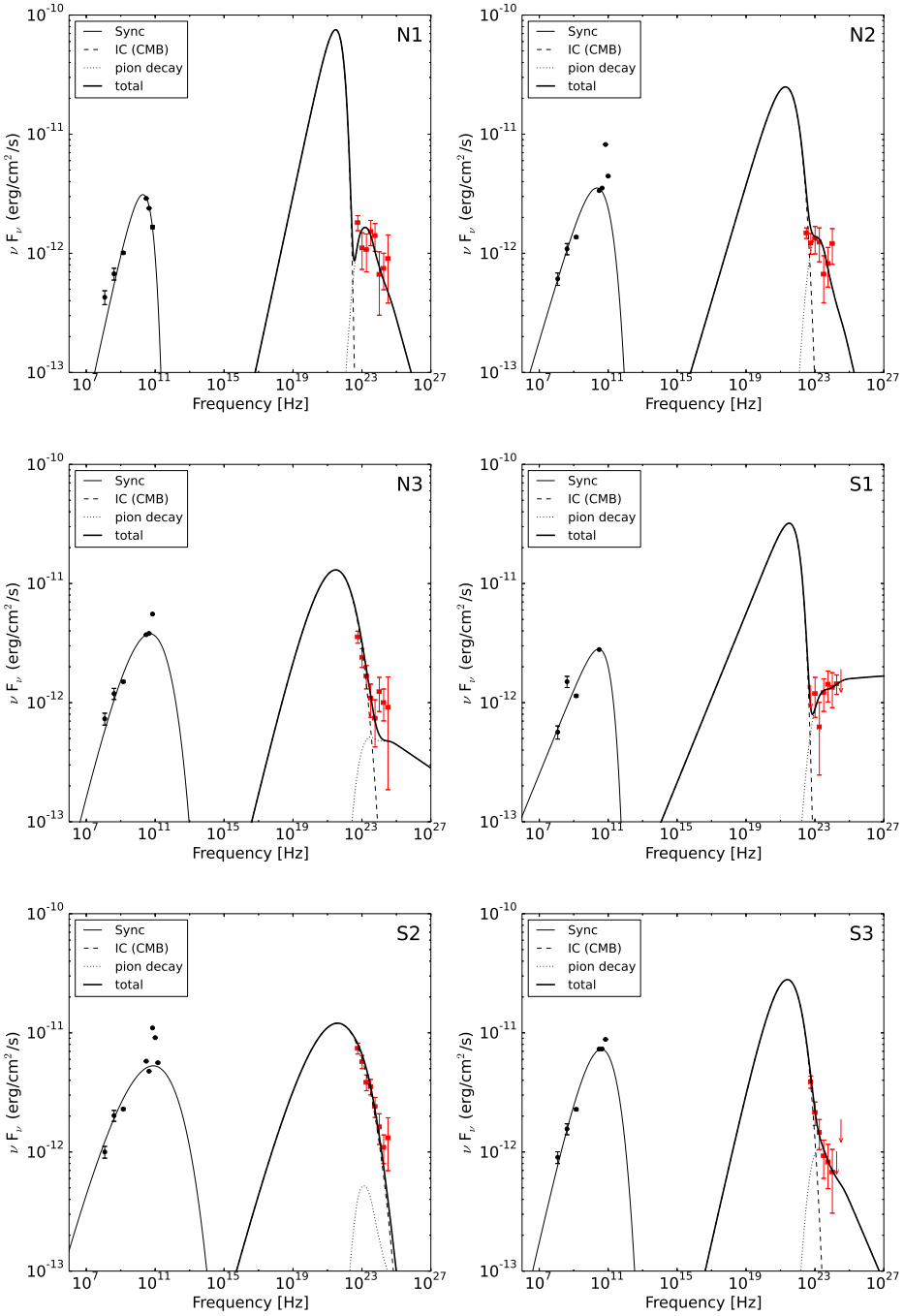

Figure 2.9: Same as Figure 2.7 but for a hybrid model in which both leptonic and hadronic process contribute.

protons in S1 is also different; it is significantly higher than in other regions. On the other hand, the additional hadronic component permits the reduction of the magnetic field to a nominal value of about 1μG. Finally, in the south lobe we see a hardening of the proton spectrum. Interestingly, such an effect has also been seen in Fermi bubbles (Su et al., 2010; Ackermann et al., 2014; Yang et al., 2014), which are two giant, ~ 10 kpc scale, γ-ray structures belonging to our Galaxy.

2.5 Conclusion and Discussion

We have analysed the SEDs of the giant lobes of Cen A across a wide range of energies. The presented results increase the significance of the γ-ray detections reported before, and, more importantly, significantly extend the γ-ray spectrum down to 60 MeV and up to 30 GeV. This allows us to make rather robust conclusions regarding the origin of different components of the γ-ray emission.

We confirm the different morphologies of the giant lobes in γ-rays and radio frequencies. This can be explained by the fact that the morphology of synchrotron radiation is strongly affected by the spatial distribution of the magnetic field. Also, the electrons responsible for γ-ray emission have higher energies than the electrons producing synchrotron emission in the lobes. To minimise the energy gap between the electrons responsible for the IC and synchrotron electrons, we further analyze the high frequency *Planck* data.

We divided both lobes into three regions and found significant spectral variations between regions. The power-law shape of the SED down to 100 MeV provides evidence against the hadronic origin of the emission. On the other hand, the extension of γ-ray emission well beyond 10 GeV, and the inclusion of the *Planck* data permits more comprehensive spectral studies and broadband modelling of the SEDs. All regions in the south and north lobes, except for the region S1, can be naturally explained within a pure leptonic model in which the γ-rays are produced because of the IC scattering of electrons on the CMB photons with a non-negligible contribution from the EBL photons. The magnetic field and the total energy in relativistic electrons in the lobes, which are derived from a comparison of the SED modelling and the *Fermi*-LAT and *Planck* data, are about 1 μG and $W_e \approx 6 \times 10^{57}$erg.

The region S1 has very different radiation characteristics compared to the other regions. This is the only region where the radio and γ-ray components have the same spectral index, and a single power-law electron spectrum is required without a break or cutoff up to energies of 1 TeV. Although the

SED of the region S1 can also be explained within a simple leptonic model, it however requires an unusually large magnetic field, $B \simeq 13\mu$G, which is an order of magnitude larger than the average field in the lobes. On the other hand, the total energy of electrons in S1 is much smaller than in other regions, by a factor of 3 to 15. Thus, the ratio of pressures due to the magnetic field and relativistic electrons in S1 differs by 2 to 3 orders of magnitude from the average value in the lobes.

An alternative explanation for the peculiar features of S1 could be the effect of a non-negligible contribution of a new radiation component, presumably of hadronic origin. This contribution, on the top of the IC component, should become significant only at high energies, therefore does not contradict the above claim that γ-rays below 1 GeV should be dominated by the IC scattering of electrons.

Indeed if we ignore the IC component from EBL, which is poorly constrained, the γ-ray spectra in all regions can be interpreted as a combination of two components: IC scattering on CMB photons and hadronic γ-rays from the pion decays. The derived total proton energy budget is of the order of 5×10^{60}erg, which is consistent with the estimation in Yang et al. (2012). Such energy could only be accumulated on a timescale as long as 10^9 yrs, assuming an injection rate of the order of 10^{44} erg/s. The diffusion coefficient of cosmic rays in this case can be estimated from the condition of their propagation to distances of order of 100 kpc: $D \sim R^2/t \sim 3 \times 10^{30} \frac{R}{100\ \mathrm{kpc}}\ \mathrm{cm}^2/\mathrm{s}$. The hardening of the spectrum of cosmic rays in the south lobe is similar to the spectral hardening towards the edge of Fermi bubbles (Su et al., 2010; Ackermann et al., 2014; Yang et al., 2014), which may be related to the energy dependent propagation of cosmic rays.

A possible problem of the leptonic+hadronic model applied to the lobes of Cen A is the huge overall energy required in relativistic protons. It exceeds the total energy in the magnetic field by two orders of magnitude. This problem, however, can be reduced if we assume that the γ-ray production at p-p collisions takes place primarily in the filamentary structures of the lobes. This is similar to the idea in Crocker et al. (2014), who propose that the collapse of thermally unstable plasma inside Fermi bubbles can lead to an accumulation of cosmic rays and magnetic field into localised filamentary condensations of higher density gas. If this is the case in the giant radio lobes of Cen A as well, the required energy budget in CRs can significantly reduce the required cosmic ray energy budget.

Concerning the relativistic electrons, their origin remains a mystery. The huge size of the giant lobes makes it impossible to transport the relativistic electrons from the core of Cen A. More specifically, the SED fitting results show that we need uncooled electrons of energy up to 50 GeV in

the north lobe. The cooling time of 50 GeV electrons can be estimated as $t_{\rm cool} \sim \frac{2\times10^{19}}{w\gamma}$ s ~ 25 Myr, where w is the energy density of the ambient radiation and magnetic fields in unit of eV cm^{-3} and γ is the Lorentz factor of the electrons. The propagation length of electrons during the cooling time is then $l \sim 30\,{\rm kpc}(\frac{\rm D}{10^{29}\ {\rm cm^2/s}})^{0.5}$, i.e. far less than the size of the lobe. The only solution is the *in situ* acceleration of the electrons, such as the stochastic acceleration in a turbulent magnetic field.

3

The Energy Distribution of Relativistic Electrons in the Kilo-Parsec Scale Jet of M87 with *Chandra*

3.1 Introduction

M87 (Virgo A, NGC 4486, 3C 274), the giant elliptical galaxy located in the Virgo cluster at a distance of 16.7 ± 0.6 Mpc (1″ = 78 pc), is one of the closest radio galaxies (Blakeslee et al., 2009; Jordán et al., 2005). It is known to host a central black hole with a mass of $\simeq (3-6)\times 10^9$ $M_\odot$ (Macchetto et al., 1997; Gebhardt et al., 2011; Walsh et al., 2013) and a one-sided ~ 30″scales jet (Marshall et al., 2002; Harris et al., 2003). The jet is characterized by a viewing angle between 10° – 25° and reveals superluminal motion of optical components of (4 – 6)c within 6″of the nucleus based on HST observations (Biretta et al., 1999). Its jet power P_j is somewhat uncertain with estimates ranging from a few times 10^{43} erg s^{-1} up to 10^{45} erg s^{-1} (e.g., Reynolds et al., 1996; de Gasperin et al., 2012; Mościbrodzka et al., 2016; Levinson & Globus, 2017). Owing to its proximity and high surface brightness at radio wavelengths and above, M87 has become a key laboratory to investigate the property of relativistic jets (e.g., Doeleman et al., 2012; Hada et al., 2016; Mertens et al., 2016; Britzen et al., 2017).

Both the nucleus and several bright jet knots have been detected at radio, optical, and X-ray wavelengths. Their broadband SEDs have been extensively studied (e.g., Biretta et al., 1991; Sparks et al., 1996; Perlman et al., 2001). The high-resolution observations performed by *Chandra* in the X-ray band make it possible to investigate the SEDs of the jet substructures in or close to the spectral cutoff regions, imposing important constraints on radiation models (e.g., Marshall et al., 2002; Wilson & Yang, 2002; Waters & Zepf, 2005; Zhang et al., 2010).

Owing to the accumulative exposure and the recently enhanced software tools of *Chandra*, an improved analysis can now be performed to derive

more accurate spectrometric information and to further investigate radiation mechanism in this region. In this chapter we present the results of a detailed analysis of the *Chandra* data on the M87 nucleus and knots observed from 2000 to 2016. This chapter is structured as follows. In Section 3.2, we describe details of the *Chandra* data reduction process, light curve analysis, and spectral analysis. In Section 3.3, we construct the radio to X-ray SEDs of the substructures (knots) in M87 and provide model fits to infer the spectral distributions of the parent particles. We discuss the consequences in Section 3.4.

3.2 *Chandra* Data Analysis

Details about *CXO* please see Section 1.4.3. In this chapter, the *Chandra* data reduction and spectra extraction are performed using CIAO (v4.8) tool and the *Chandra* Calibration Database (CALDB, v4.7.2). We perform the spectral analysis with *Sherpa*.

3.2.1 Data preparation

We collected the *Chandra* ACIS timed exposure (TE) mode observations from April 15 (ObsID 517), 2000 until June 12, 2016 (ObsID 18856) to perform a detailed analysis of the M87 jet and nucleus. In Table 3.1 we list all the observations, including 99 observations with a 0.4 s frame time and 13 observations with a 3.2/3.1 s frame time. The total exposure time is over 1460 kiloseconds.

Figure 3.1 provides an exemplary case, showing the ObsID 1808 X-ray image binned into 0.123″ per pixel and smoothed with a Gaussian of FWHM=0.3".

To avoid pileup (i.e., two or more photons arriving at the same pixel during a single frame time, thus mimicking a single event with the sum of the energies; see e.g., Davis, 2001), we generally selected the observations with frame time of 0.4 s for all substructures analyses. However, because the knots E, F, I, B, and C, as shown in Figure 3.1, are much fainter than the nucleus, HST-1, knot D, and knot A, we also included the observations with frame time of 3.2/3.1 s in the analysis of these knots.

To reduce uncertainties caused by the position offsets of different observations, we perform the astrometric corrections as follows. In order to obtain more reliable source localisation during the process of astrometric correction, the effect of broadband energy on the exposure map needs to be avoided. Thus we first produce the exposure-corrected image, the weighted exposure map, and the weighted PSF map. Finally, we perform *wcs_match* and *wcs_update* to match all selected *Chandra* observations with a reference

Table 3.1: *Chandra* Observations of M87.

ObsID	Frame Time (s)	Exp Time (ks)	Start Date (YYY-MM-DD)	ObsID	Frame Time (s)	Exp Time (ks)	Start Date (YYY-MM-DD)
1808	0.4	12.85	2000-07-30	8578	0.4	4.71	2008-04-01
3085	0.4	4.89	2002-01-16	8579	0.4	4.71	2008-05-15
3084	0.4	4.65	2002-02-12	8580	0.4	4.7	2008-06-24
3086	0.4	4.62	2002-03-30	8581	0.4	4.66	2008-08-07
3087	0.4	4.97	2002-06-08	10282	0.4	4.7	2008-11-17
3088	0.4	4.71	2002-07-24	10283	0.4	4.7	2009-01-07
3975	0.4	5.29	2002-11-17	10284	0.4	4.7	2009-02-20
3976	0.4	4.79	2002-12-29	10285	0.4	4.66	2009-04-01
3977	0.4	5.28	2003-02-04	10286	0.4	4.68	2009-05-13
3978	0.4	4.85	2003-03-09	10287	0.4	4.7	2009-06-22
3979	0.4	4.49	2003-04-14	10288	0.4	4.68	2009-12-15
3980	0.4	4.79	2003-05-18	11512	0.4	4.7	2010-04-11
3981	0.4	4.68	2003-07-03	11513	0.4	4.7	2010-04-13
3982	0.4	4.84	2003-08-08	11514	0.4	4.53	2010-04-15
4917	0.4	5.03	2003-11-11	11515	0.4	4.7	2010-04-17
4918	0.4	4.68	2003-12-29	11516	0.4	4.71	2010-04-20
4919	0.4	4.7	2004-02-12	11517	0.4	4.7	2010-05-05
4921	0.4	5.25	2004-05-13	11518	0.4	4.4	2010-05-09
4922	0.4	4.54	2004-06-23	11519	0.4	4.71	2010-05-11
4923	0.4	4.63	2004-08-05	11520	0.4	4.6	2010-05-14
5737	0.4	4.21	2004-11-26	13964	0.4	4.54	2011-12-04
5738	0.4	4.67	2005-01-24	13965	0.4	4.6	2012-02-25
5739	0.4	5.15	2005-02-14	14974	0.4	4.6	2012-12-12
5740	0.4	4.7	2005-04-22	14973	0.4	4.4	2013-03-12
5744	0.4	4.7	2005-04-28	16042	0.4	4.62	2013-12-26
5745	0.4	4.7	2005-05-04	16043	0.4	4.6	2014-04-02
5746	0.4	5.14	2005-05-13	17056	0.4	4.6	2014-12-17
5747	0.4	4.7	2005-05-22	17057	0.4	4.6	2015-03-19
5748	0.4	4.7	2005-05-30	18233	0.4	37.25	2016-02-23
5741	0.4	4.7	2005-06-03	18781	0.4	39.51	2016-02-24
5742	0.4	4.7	2005-06-21	18782	0.4	34.07	2016-02-26
5743	0.4	4.67	2005-08-06	18809	0.4	4.52	2016-03-12
6299	0.4	4.65	2005-11-29	18810	0.4	4.6	2016-03-13
6300	0.4	4.66	2006-01-05	18811	0.4	4.6	2016-03-14
6301	0.4	4.34	2006-02-19	18812	0.4	4.4	2016-03-16
6302	0.4	4.7	2006-03-30	18813	0.4	4.6	2016-03-17
6303	0.4	4.7	2006-05-21	18783	0.4	36.11	2016-04-20
6304	0.4	4.68	2006-06-28	18232	0.4	18.2	2016-04-27
6305	0.4	4.65	2006-08-02	18836	0.4	38.91	2016-04-28
7348	0.4	4.54	2006-11-13	18837	0.4	13.67	2016-04-30
7349	0.4	4.68	2007-01-04	18838	0.4	56.29	2016-05-28
7350	0.4	4.66	2007-02-13	18856	0.4	25.46	2016-06-12
8510	0.4	4.7	2007-02-15	517	3.2	6.99	2000-04-15
8511	0.4	4.7	2007-02-18	241	3.2	38.04	2000-07-17
8512	0.4	4.7	2007-02-21	352	3.2	37.68	2000-07-29
8513	0.4	4.7	2007-02-24	3717	3.2	20.56	2002-07-05
8514	0.4	4.47	2007-03-12	2707	3.2	98.66	2002-07-06
8515	0.4	4.7	2007-03-14	6186	3.2	51.55	2005-01-31
8516	0.4	4.68	2007-03-19	7212	3.1	65.25	2005-11-14
8517	0.4	4.67	2007-03-22	7210	3.1	30.71	2005-11-16
7351	0.4	4.68	2007-03-24	7211	3.1	16.62	2005-11-16
7352	0.4	4.59	2007-05-15	5828	3.1	32.99	2005-11-17
7353	0.4	4.54	2007-06-25	6186	3.1	51.55	2005-01-31
7354	0.4	4.71	2007-07-31	5827	3.1	156.2	2005-05-05
8575	0.4	4.68	2007-11-25	5826	3.1	126.76	2005-03-03
8576	0.4	4.69	2008-01-04				
8577	0.4	4.66	2008-02-16				

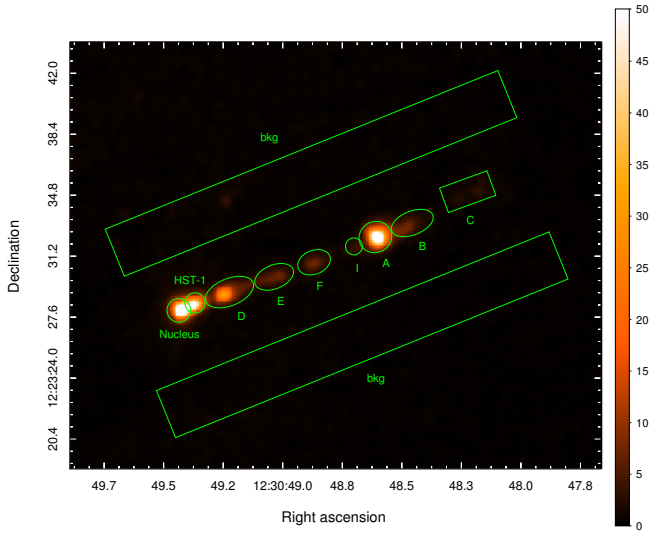

Figure 3.1: Image from the observation on 2000 July 30 (ObsID 1808) in the 0.2-10 keV, binned in 0.123″ per pixel and smoothed with a Gaussian of FWHM=0.3″. The source and background regions are indicated by green shapes. Units of right ascension are hours:minutes:seconds, and units of declination are degrees:arcminutes:arcseconds.

observation ObsID 1808 separately. We choose ObsID 1808 as a reference because it has the longest exposure time among the observations with frame time of 0.4 s, thus it has the best statistics to ensure an accurate positioning. We define the source region of each knot based on the X-ray positions in table 1 of Perlman & Wilson (2005). The source and background regions are shown in Figure 3.1.

3.2.2 Time variability

To study the time variabilities, we extract the flux for each observation in the 0.3-7 keV energy band and build the light curves for each region.

Nucleus

The nucleus reveals significant variabilities as shown in the top panel of Figure 3.2. We define five flaring periods, marked with "1", "2", "3", "4", and "5" and present zoomed-in light curves in Figure 3.2. To investigate the characteristic time scales of these flares in more detail, we fit the light curves with an exponential function of the form

$$\Phi = \Phi_0 \times e^{-|t-t_0|/\Delta\tau} \tag{3.1}$$

Here $\Delta\tau = \tau_d/\ln(2)$, τ_d is the characteristic timescales of each flare. We freeze t_0 to the time of the highest data point for each flare. Φ_0 and τ_d are free

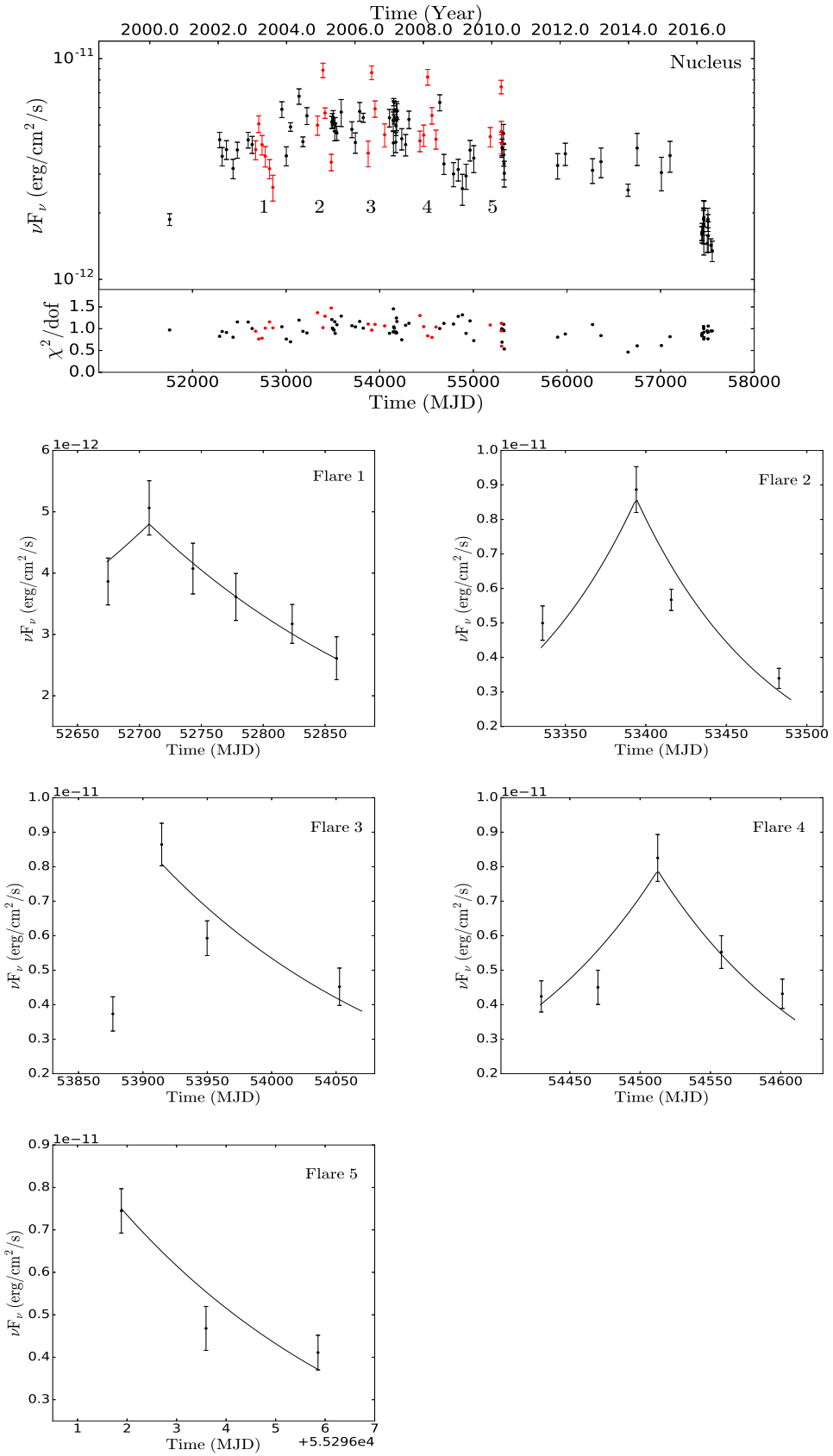

Figure 3.2: Top: The *Chandra* 0.3-7 keV light curve for the nucleus from July 29, 2000 (MJD 51754) until March 17, 2016 (MJD 57464). Five flares (red data points, labeled as "1", "2", "3", "4", and "5") are selected for further analyses in the following. Bottom: Zoomed-in light curve of the five flares. The solid lines show the fitting results by using Eq. 1.

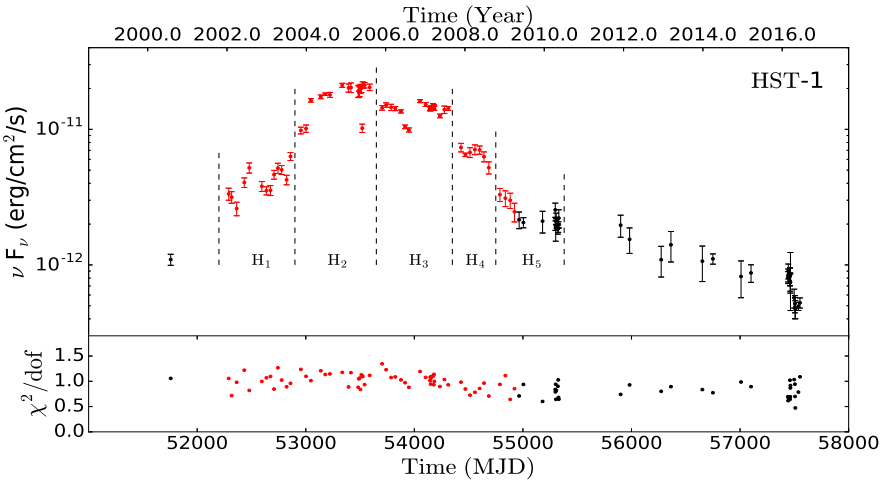

Figure 3.3: The *Chandra* 0.3-7 keV light curve for HST-1 during the same time interval as in Figure 3.2. The black points are considered to belong to the low state (L). The dashed lines, on the other hand, separate the high state from January 16 (MJD 52290), 2002 until May 14, 2010 (MJD 55330)) into five subsections, that are labeled as H_1, H_2, H_3, H_4, and H_5. The data from April 01, 2009 to May 14, 2010 belong to a transition period between high and low state, and have thus been included in both, L and H_5 calculations.

parameters. In principle the rising and decay timescale can be different. The current data set, however, prevents us from deriving difference of the two timescales due to the limited time coverage, especially in the rising stage. Thus for the flares 1, 2, and 4 we perform fits assuming that both the rising and decaying stage have the same τ_d. For the flares 3 and 5 we only fit the decaying stage. The corresponding values of Φ_0, τ_d, and t_0 are listed in Table 3.2. The characteristic timescale for flare 5 is shortest with $\tau_d = 3.9 \pm 1.7$ days. This flare is contemporaneous to the rapid TeV γ-ray flare seen on April 9-10, 2010 (MJD 55296) (see e.g., Abramowski et al., 2012; Harris et al., 2011). The day-scale activity seen at X-ray and TeV energies in this context favours a common physical origin of this emission (Abramowski et al., 2012; Aliu et al., 2012).

HST-1

HST-1 shows significant variability over time, revealing flux variations much larger than those of the nucleus. During the period from 2002 to 2010 the total X-ray energy flux varied by one order of magnitude, reaching an extreme high state in 2005 (see Fig. 3.3).

The 2005 X-ray high state of HTS-1 seemingly correlates with a high state of M87 at TeV energies exhibiting rapid day-scale activity (Aharonian et al., 2006). Early models thus assumed a common physical origin, while the

Table 3.2: The fitting parameters for the selected flares of the nucleus using a symmetric exponential function.

Flare	Time Range (MJD)	τ_d (days)	t_0 (frozen) (MJD)	Φ_0 ($\times 10^{-12}$ erg/cm^2/s)
Flare 1	52675-52859	171.27±23.07	52708	4.80±0.17
Flare 2	53336-53483	66.36±16.32	53394	8.35±0.75
Flare 3	53877-54053	143.38±64.76	53915	8.08±0.97
Flare 4	54430-54601	85.11±18.95	54512	7.89±0.68
Flare 5	55181-55302	3.91±1.70	55298	7.23±0.96

All errors are 1σ confidence level.

apparent absence of such a correlation for the subsequent TeV high state in 2010 has been taken as disfavouring it. We note that there are several reasons why day-scale TeV activity related to HST-1 now appears disfavoured (see Rieger & Aharonian, 2012, for review and discussion). The presence or absence of a possible X-ray-TeV correlation, however, seems rather less conclusive in this regard as changes in the magnetic field and radiating particle number in a synchrotron (X-ray) and inverse Compton (TeV) approach could well allow to accommodate both of them.

The X-ray flux of HST-1 seems to be continuously decreasing since 2007 with a characteristic decay timescale of $\sim (0.5-1)$ yr. This supports previous indications (Harris et al., 2009), and while dominant IC cooling is not excluded (e.g., Perlman et al., 2011), seems compatible with the synchrotron cooling timescale of electrons producing ~ 1 keV photons in a ~milligauss magnetic field, $t_{\rm syn} \lesssim 1.5\,(2\times10^7/\gamma')(1\ {\rm mG/B'})^2\delta^{-1}$ yr. This could be taken as providing additional evidence for a synchrotron origin of the X-ray emission.

For the analysis of the spectral variations of HST-1 presented in Section 3.2.3, we divide the high activity period from January 16, 2002 (MJD 52290) until May 14, 2010 (MJD 55330) into five sections denoted by H_1, H_2, H_3, H_4, and H_5. The observation on July 30, 2000 (ObsID 1808) and the observations after May 13, 2009 (ObsID 10286) are treated as low state (L). The observations from April 01, 2009 to May 14, 2010, on the other hand, belong to a transition period between the high and the low state, and have thus been included in the following in both, L and H_5 spectral calculations. For a bright source pile-up could lead to distortions in the energy spectrum. Using the *pileup_map* tool, we estimated the pileup fraction and found that for H2, H3 and H4 the fraction is larger than 10%, even though we have only selected observations with frame time of 0.4 s to avoid pileup. Thus for the following spectral analysis we only include H1, H5 and L for HST-1.

Other knots

Knot D and knot A show no significant variability. The flux variations lie within the statistic errors of the flux determination, which is 15% for knot D and 5% for knot A. The fluxes derived for the knots E, F, I, B, and C have significant uncertainties due to the limited statistics of the observations. We do not find any hint for variability even after re-binning the observations. With exception of HST-1, we thus combined all observations for the following spectral analysis of the knots.

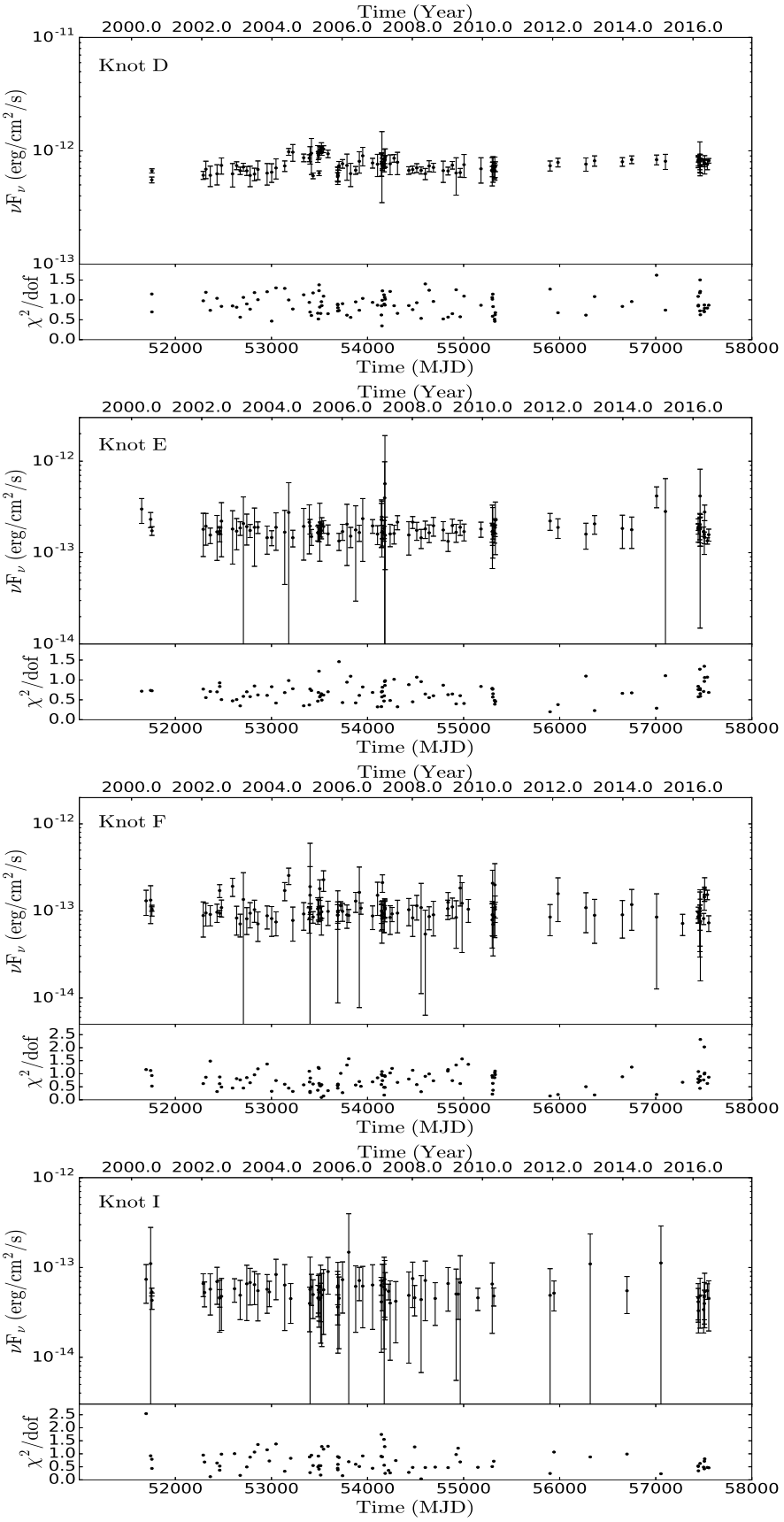

Figure 3.4: *Chandra* 0.3-7 keV light curves for the knots D, E, F, I, A, B, and C during the same time interval as in Figure 3.2.

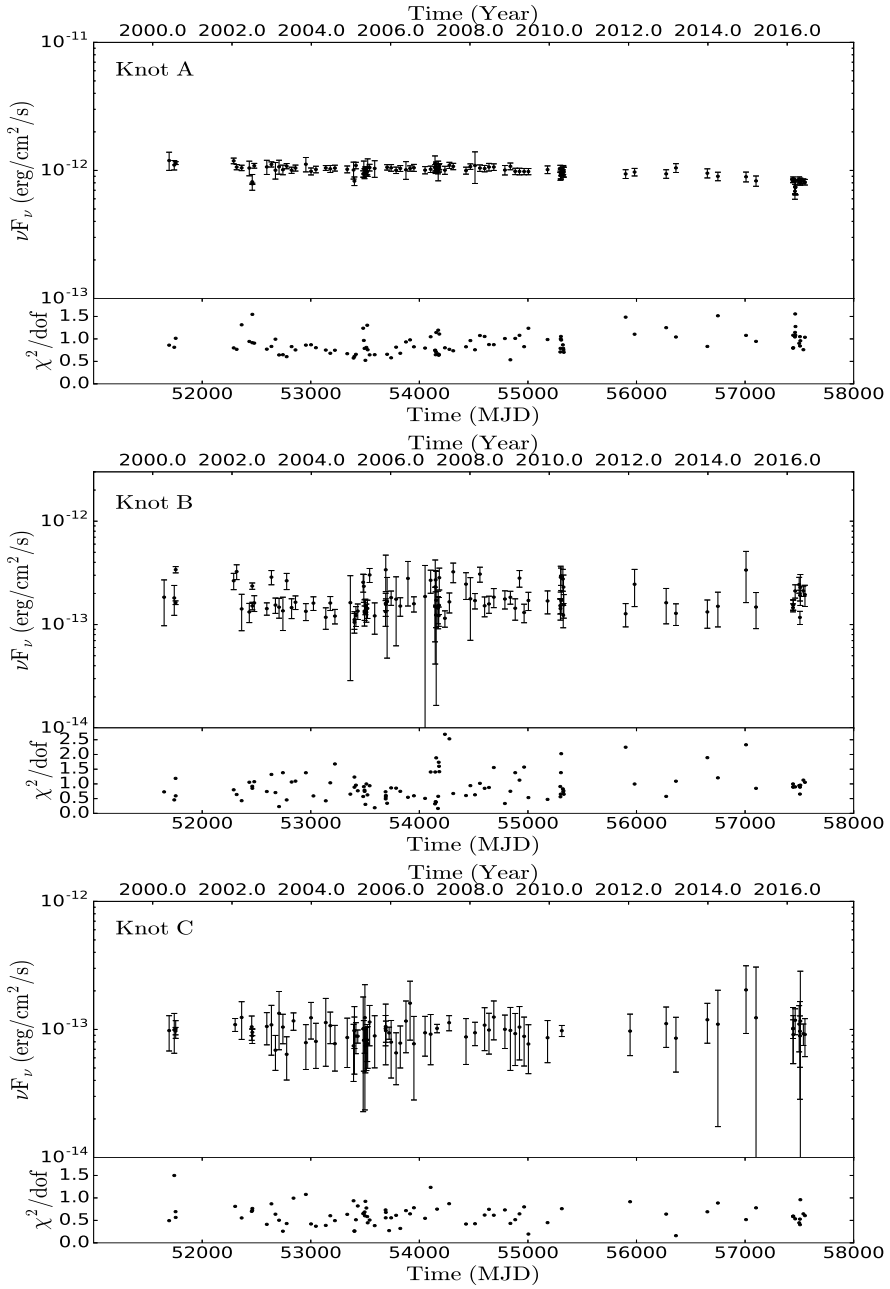

Figure 3.4 — continued

3.2.3 Spectral analysis

For the spectral analysis we perform an aperture photometry using *specextract* on the nucleus and each knot. The source and background regions are defined as in Figure 3.1.

Nucleus and HST-1 in early 2010

The nucleus is highly variable and suffers from pile-up even for observations with frame time of 0.4 s, which could affect the inherent spectral energy distribution (e.g., lead to spectral hardening). Thus we don't combine any observation. Instead, we focus only on an analysis of those observations contemporaneous to the 2010 TeV flare. In 2010 HST-1 was back to a state comparable with the pre-2004 time, during which pile-up was found to be fairly mild (Harris & Krawczynski, 2006; Russell et al., 2015). We fit the spectra in each observation using a single power-law plus Galactic absorption model. To suitably deal with the pile-up we add an additional pileup model *jdpileup* to the spectral fit. The fitted indices for the nucleus are shown in Tab. 3.3 along with those for HST-1. The photon indices for the nucleus are on average close to $\Gamma \sim 2.1 - 2.2$, which seems compatible with earlier (non-flaring) results (Wilson & Yang, 2002; Perlman & Wilson, 2005). A hint for spectral variations might be seen in the nucleus, while the HST-1 spectrum appears stable, though the short exposures limit definitive inferences. Our values for the nucleus are similar to that in Harris et al. (2011). Our values for the nucleus are similar to that in Harris et al. (2011). Our results for HST-1, however, are harder than those reported in Harris et al. (2011), yet still compatible within the 1σ error bars. We note that in our analysis the error bars are much larger due to the additional free parameters in the pileup model that has been included in our analysis. For sources closer than an arcsec, such as the nucleus and HST-1 (which are separated by 0.86"), an "eat-thy-neighor" effect may in principle occur (Harris & Krawczynski, 2006; Harris et al., 2009), where photons arriving within the same frame time and 3×3 pixel grid are registered as a single event at the location of the pixel with the larger energy. As suggested by Harris et al. (2009) this effect is however not expected to cause serious problems below a (detector-based) intensity limit of 4 keV/s (e.g., for the pre-2004 and post-2006 time for HST-1).

The X-ray photon indices for the nucleus are in principle in the range of those achievable by Comptonization in a hot accretion flow. Early models in fact assumed that the (quiescent) nuclear X-ray emission in M87 is produced by an ADAF (e.g., Reynolds et al., 1996; Di Matteo et al., 2003). The similarities of the nuclear spectrum to that of the jet and its knots, and the strong brightness increase towards the nucleus (cf. Figure 3.5), however, suggest that this "nuclear" emission is instead dominated by the jet (Wilson & Yang, 2002). This is supported by the fact that the luminosity of a hot accretion flow at low accretion rates $\dot{M}$ roughly scales with $\dot{M}^2$, i.e. $L_{ADAF} \propto \dot{M}^2$, while that of the jet with $L_j \propto \dot{M}$, so that for low $\dot{M}$ the jet starts to dominate (Yuan & Narayan, 2014; Feng & Wu, 2017). The evidence for strong nuclear activity

Table 3.3: X-ray photon indices for the nucleus and HST-1 during the 2010 TeV flare.

ObsID	$\Gamma_{\rm Nucleus}$	$\Gamma_{\rm HST-1}$
11512	1.97 ± 0.1	$2.17^{+0.24}_{-0.21}$
11513	$2.14^{+0.15}_{-0.14}$	$2.20^{+0.27}_{-0.12}$
11514	$1.98^{+0.16}_{-0.15}$	$2.33^{+0.31}_{-0.16}$
11515	$2.10^{+0.17}_{-0.16}$	$2.23^{+0.18}_{-0.11}$
11516	$1.84^{+0.16}_{-0.13}$	$2.24^{+0.26}_{-0.13}$
11517	$2.26^{+0.16}_{-0.15}$	$2.23^{+0.28}_{-0.12}$
11518	$2.16^{+0.20}_{-0.18}$	$2.28^{+0.18}_{-0.14}$
11519	$2.19^{+0.19}_{-0.14}$	$2.22^{+0.21}_{-0.11}$
11520	$2.24^{+0.21}_{-0.18}$	$2.33^{+0.29}_{-0.11}$

All errors are 90% confidence level.

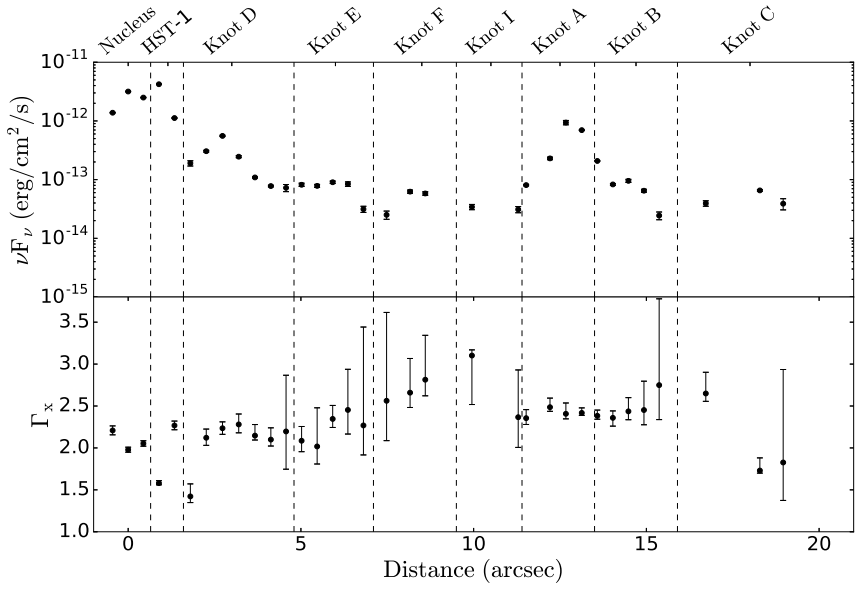

Figure 3.5: Flux density (top panel) and power-law photon index (bottom panel) in the X-ray 0.3-7 keV band along the jet. The source regions are separated by the dashed lines. For this representation all observations with frame time 0.4 s have been used for the nucleus, while for HST-1 only "HST-1 L" data have been employed.

over time fits well into this.

Combined X-ray spectra of the knots

For all knots, except HST-1, we fit multiple observations simultaneously. For HST-1 we exclude observations during H_2, H_3, and H_4 in the spectral analysis due to significant pile-up.

Table 3.4: Results for the X-ray spectral fitting of the knots.

Component	Γ^{a}	$N_{\rm H}$ [b] ($\times10^{20}$/cm^2)	K^{c} ($\times10^{-5}$photons/keV/s)	νF_ν [d] ($\times10^{-13}$erg/cm^2/s)	reduced χ^2	dof
HST-1 H_1	2.25±0.05	$4.74^{+0.78}_{-0.75}$	$94.88^{+3.20}_{-3.10}$	44.73±0.62	0.98	2174
HST-1 H_5	2.31±0.06	$1.21^{+1.15}_{-1.10}$	$50.59^{+2.45}_{-2.16}$	23.62±0.59	0.93	1293
HST-1 L	$2.27^{+0.06}_{-0.04}$	<1.21	$14.53^{+0.69}_{-0.35}$	6.86±0.15	1.08	1801
D	2.11±0.02	2.58±0.45	$15.32^{+0.29}_{-0.28}$	7.45±0.10	0.94	6805
E	2.35±0.05	$2.34^{+0.86}_{-0.83}$	$4.10^{+0.16}_{-0.15}$	1.91±0.04	0.70	2726
F	$2.61^{+0.07}_{-0.02}$	<0.46	$2.15^{+0.06}_{-0.05}$	1.00±0.01	0.74	1720
I	$2.50^{+0.04}_{-0.11}$	<0.57	$1.20^{+0.02}_{-0.08}$	0.56±0.04	1.02	576
A	2.41±0.02	<0.10	$21.22^{+0.13}_{-0.36}$	9.85±0.02	0.90	4811
B	$2.35^{+0.06}_{-0.02}$	<0.8	$3.49^{+0.13}_{-0.06}$	1.63±0.02	0.89	2480
C	$1.89^{+0.09}_{-0.03}$	<0.85	$1.78^{+0.12}_{-0.04}$	0.94±0.02	0.64	2145
F	2.79±0.04	2.4 (frozen)	2.36±0.05	1.13±0.02	0.75	1721
I	2.60±0.04	2.4 (frozen)	1.28±0.03	0.60±0.01	1.04	577
A	2.55±0.01	2.4 (frozen)	23.10±0.2	10.74±0.05	0.96	4812
B	2.49±0.03	2.4 (frozen)	3.85±0.06	1.79±0.02	0.90	2481
C	2.01±0.04	2.4 (frozen)	1.99±0.05	1.0±0.02	0.65	2146

All errors are 90% confidence level.
[a] Photon index.
[b] Equivalent hydrogen-absorbing column density.
[c] Amplitude of power-law model.
[d] Total integrated energy flux over 0.3-7 keV.
The bottom part provides the results if N_H is frozen to the Galactic value.

In the X-ray band all knots can in principle be well fitted with a single power-law plus Galactic absorption model, none seems to require an obvious break or additional component within the X-ray band itself (but see below). Table 3.4 lists the best-fit parameter values and the reduced χ^2 value. The reduced χ^2 values reveal that all fits are acceptable at 90% confidence level. Leaving the absorption column density N_H free in the fit yields values deviating significantly from the Galactic one (Perlman & Wilson, 2005). Harris & Krawczynski (2006) have reported a mutual dependence between N_H and α in the fitting process, leading to some uncertainty. For comparison we thus also provide results with N_H frozen to the Galactic value. We do not find evidence for a significant deviation (Osone, 2017) from a pure power-law in the X-ray band for knot A if N_H is kept frozen.

The derived photon indices for different knots are significantly different, ranging from $\simeq$ 1.89 (knot C) to $\simeq$ 2.61 (knot F). The results roughly match those obtained by Wilson & Yang (2002, 2004) and Perlman & Wilson (2005). In Figure 3.5 we plot the profiles of the flux density and photon index $\alpha_{\rm x}$ along

the jet by dividing the knots into small strips. We again use the single power-law plus Galactic absorption model to fit each region. Finally, we use the best fit model to simulate the energy flux of the de-convolved non-thermal emission. In this process we divide the X-ray energy interval between 0.3 keV and 7 keV into 4 bins in logarithmic space. The derived X-ray data points are listed in Tab. 3.5. With the exemption of the outermost knot C, the X-ray photon index along the jet exhibits a trend similar to that reported in Perlman & Wilson (2005), with slight but significant index variations ranging from $\simeq 2.1-2.2$ (e.g. in knot D) to $\simeq 2.4-2.6$ (in knots F, A, and B). There is little evidence for the inter-knot regions to have significantly steeper spectra than the adjacent knots reinforcing the need for a distributed acceleration mechanism.

3.3 SED Modeling

In order to gain further insights we construct the radio to X-ray SEDs of the knots and provide model fits to infer the characteristics of the parent particle distribution. We select contemporaneous multi-wavelength data to ensure an adequate reconstruction. The optical to X-ray spectra of the H_1, H_5, and L state of knot HST-1 are taken from the 2002 December, 2003 February, and 2003 April HST observations in Perlman et al. (2003), respectively. The radio data are from Giroletti et al. (2012) based on observations between 2006 and 2010 with the Very Long Baseline Array (VLBA) at 1.7 GHz for H_1, and between 2009 and 2011 with the European VLBI Network (EVN) at 5 GHz for the statuses H_5 and L. We further use the published optical-near-infrared data from Perlman et al. (2001), and the ultraviolet data from Waters & Zepf (2005) for the knots D, E, F, I, A, B, and C. The black points in the radio energy band are from Perlman et al. (2001). We don't include the radio data points of Biretta et al. (1991) in the spectral fitting, yet regard them as a reference for the radio spectral indices because of the uncertainties with regard to these measurements (see e.g., Perlman & Wilson, 2005). It should also be noted that although our region C could be further divided into the sub-regions C1 and C2, we only include the ultraviolet fluxes for C1. This simplification appears justified considering the much lower ultraviolet flux from C2. For comparison, we also plot the X-ray flux density from Marshall et al. (2002) with grey symbols in Figure 3.6.

There are in principle several possible non-thermal scenarios for the origin of large-scale X-ray emission, such as inverse Compton upscattering (IC) of either synchrotron (synchrotron self-Compton; IC-SSC) or cosmic microwave background (IC-CMB) photons, or direct synchrotron emission of

Table 3.5: Deconvolved X-ray flux densities of the knots for different energy bands.

Energy [keV]	0.3 – 0.7	0.7 – 1.4	1.4 – 3.2	3.2 – 7.0
Component	Flux density [$\times 10^{-14}$erg/cm^2/s]			
HST-1 H_1	159.06±3.23	106.78±1.47	104.89±2.10	81.78±2.64
HST-1 H_5	89.26±3.11	56.74±1.29	53.78±1.68	39.83±2.33
HST-1 L	24.58±0.97	16.40±0.40	15.92±0.66	12.14±0.97
D	23.03±0.33	17.22±0.17	18.71±0.24	16.10±0.33
E	7.47±0.20	4.61±0.10	4.21±0.12	3.02±0.14
F	4.82±0.11	2.44±0.03	1.83±0.04	1.05±0.04
I	2.48±0.26	1.36±0.09	1.12±0.13	0.69±0.12
A	40.38±0.19	23.94±0.06	20.86±0.09	14.19±0.12
B	6.33±0.10	3.93±0.05	3.58±0.10	2.56±0.05
C	2.25±0.04	2.00±0.03	2.59±0.06	2.67±0.10

relativistic electrons or protons (e.g., Aharonian, 2002; Harris & Krawczynski, 2002; Georganopoulos et al., 2016). As discussed in Wilson & Yang (2002), to account for the keV X-ray flux by means of leptonic IC-SSC processes, the magnetic field has to be substantially lower than equipartition. In the case of IC-CMB it is possible to boost the X-ray flux by relativistic bulk motion, but this requires high Doppler factors $\delta \simeq (10 - 40)$ and very small angles $\theta \simeq (1.2° - 4.7°)$ between the jet and the line of sight (Harris & Krawczynski, 2002). Though HST observations indicate that moderate superluminal motion in M87 could persist out to knot C (Meyer et al., 2013), such values remain highly unlikely. Moreover, IC radiation by a power-law electron distribution in the Thomson regime is expected to exhibit a spectral index similar to the one for synchrotron radiation, yet the observed X-ray spectra of the knots are all significantly steeper than the radio spectra (exhibiting spectral indices $\alpha_{rr} \sim 0.5$, e.g. Biretta et al., 1991). An IC origin of the X-ray emission in M87 thus appears disfavoured (see also Biretta et al., 1991; Meisenheimer et al., 1996; Wilson & Yang, 2002; Perlman & Wilson, 2005), and we therefore only consider an electron synchrotron origin in the following.

We use the Markov Chain Monte Carlo (MCMC) code *Naima* (Zabalza, 2015) to explore the characteristics of the radiating particle distribution. The code allows to implement different functional and includes tools to perform MCMC fitting of non-thermal radiative processes to the data. Given the radio to X-ray data of the knots in M87, the simplest functional form to take into account is a broken power-law,

$$N(E) = \begin{cases} AE^{-\alpha_1} & E \leq E_{\mathrm{break}} \\ AE_{\mathrm{break}}^{(\alpha_2-\alpha_1)}\, E^{-\alpha_2} & E > E_{\mathrm{break}}\,. \end{cases} \tag{3.2}$$

For the fitting process, the parameters A, α_1, $E_{\rm break}$, α_2 are left as free parameters and we assume non-relativistic motion for the entire jet. Our results (cf. Table 3.6) show that the SEDs of the knots E, F, I and A could in principle be satisfactorily described by synchrotron emission of a broken power-law electron distribution with an index $\alpha_1 \simeq 2.3$ resembling that of particle acceleration at highly relativistic shocks (e.g., Achterberg et al., 2001). The second index α_2 for these knots deviates from that of a classical cooling break. This is interesting, but could possibly be accounted for by deviations from a homogeneous one-zone approach and/or some additional re-acceleration (e.g., Liu & Shen, 2007; Sahayanathan, 2008; Liu et al., 2017). Diffusive synchrotron radiation from random small-scale magnetic field could offer an alternative explanation (Fleishman, 2006), although the observed high radio and optical polarisation (e.g., Avachat et al., 2016) may complicate this interpretation. We note that comparison of the fit results for a broken power-law and a log-parabola model (cf. Massaro et al., 2004; Tramacere et al., 2007) shows the first to be preferred over the second one.

The SEDs of the knots D, B, and C, on the other hand, cannot be well-fitted assuming a homogeneous source region and the broken power-law form Eq. (3.2). In principle, this should not come as a surprise given the morphological complexity of the knots and the evidence for internal jet stratification (e.g., Perlman & Wilson, 2005; Avachat et al., 2016). The findings are nevertheless quite interesting by providing a first indication that the X-ray emission of large-scale AGN jets might reveal some excess above a simple power-law extension from the optical fluxes, and in fact consist of multiple contributions. To explore this in more details, we add an additional electron component to fit the X-ray data. For simplicity we choose two exponential cutoff power-law models

$$N(E) = A_1\, E^{-\alpha_1}\, \exp\left[-\left(\frac{E}{E_{\rm cutoff1}}\right)^{\beta}\right] + A_2\, E^{-\alpha_2}\, \exp\left[-\left(\frac{E}{E_{\rm cutoff2}}\right)^{\beta}\right], \qquad (3.3)$$

treating again A_1, α_1, $E_{\rm cutoff1}$, A_2, α_2, and $E_{\rm cutoff2}$ as free parameters for the fit. We note that alternative descriptions (e.g., two broken power-laws with exponential cut-off) are in principle possible, yet require to fix some additional parameters. In our phenomenological fit the two components are treated as independent. We note, though, that the correlation between the X-ray flux maxima and the synchrotron break frequencies (e.g. Perlman & Wilson, 2005) suggest that the X-ray emitting particles are not completely independent from those at lower energies. The results should thus be treated as a first guide only. To reduce the free parameters in our fit (cf. eq. 3.3), we fixed the parameter β to 1 and 2, corresponding to the escaping and cooling-dominated regime, respectively. We assume a magnetic field strength of

$B = 300\,\mu$G (Heinz & Begelman, 1997; Marshall et al., 2002) as reference value in all our calculations. This is certainly a simplification as the magnetic field strength is expected to be different for different regions, e.g. to vary by a factor of ~ 2 when different knots are compared (e.g., Biretta et al., 1991; Meisenheimer et al., 1996). We note however, that in the fitting procedure B scales as $E_{\rm cutoff}^{-2}$ and $A^{-0.5}$, so that a different B only affects the best-fit value of the break or cutoff energy, and the absolute normalization.

The derived model parameters as well as the total energy in non-thermal electrons, $W_{\rm e}$, with 1σ errors are listed in Table 3.6. Figure 3.6 shows the corresponding synchrotron model fits for the observed SEDs of the knots. The curves represent the SED models with the maximum likelihood. For the knots D, B, and C, the dashed curves and the dot-dashed curves are derived from two exponential cutoff power-law components, respectively, as noted above. The derived values for the required energy in non-thermal electrons range up to $W_{\rm e} \simeq 10^{53}$ erg (knot A) and imply a jet kinetic power $P_{\rm j} \gtrsim 10^{43}$ erg/s, compatible with other estimates for the general jet power (see introduction). The energy density in electrons, u_e, is typically comparable to (or somewhat) less than the one in magnetic fields, $u_B = B^2/(8\pi)$, ensuring efficient confinement.

Our findings provide indications that for the knot regions D, B and C an additional X-ray emitting component is needed to achieve a satisfactory SED description. The indications are strongest in the case of knot C where the X-ray emission seems particularly hard, and less strong in the case of knot D. It is worth noting that radio and optical observations show that the knot D region, located approximately between 2 and 5 arcsec, reveals extended structures and can be further divided into sub-regions D-East, D-Middle and D-West, each with additional sub-components (e.g. Perlman & Wilson, 2005; Avachat et al., 2016). Similarly, knot B, located approximately between 13 and 16 arcsec, can be divided into the sub-components B1 (broader and brighter) and B2, while the knot C region, located approximately between 17 and 19 arcsec, can be divided into the subregions C1 and C2 (Perlman & Wilson, 2005; Avachat et al., 2016). It seems thus conceivable that the inferred two-component electron distribution can in principle be accounted for by a superposition of electrons from different sub-regions. Moreover, the features seen in the optical tend to be slightly narrower than those seen in radio, suggesting that the radiating particles, although co-located, may not necessarily have to be truly co-spatial. We note that we have incorporated only the simplest broken power-law function to fit the SED of the knots (except for B,C and D) and formally cannot rule out the possibility that the SEDs of these knots are produced by more than one electron component as well. Noting these caveats, the respective parent electrons distributions

are shown in Figure 3.7. As can be seen, for the considered normalization of the magnetic field strength the electron distribution tends to show a break at energies around one TeV ($\gamma_b \sim 2 \times 10^6$) and needs to extend up to multi-TeV energies ($\gamma \sim 10^8$). These high-energy electrons cannot travel more than a few parsecs before exhausting their energies due to synchrotron cooling. A synchrotron origin thus requires an efficient and continuous in-situ acceleration of electrons along the jet.

Inverse Compton (IC) up-scattering of cosmic microwave background (CMB) photons ($h\nu_{\rm CMB}$) by these relativistic electrons will result in γ-ray emission extending up to $\sim 10\,(\gamma/10^8)^2$ TeV. The characteristic energy flux levels νF_ν at TeV energies are, however, a factor of $\sim u_{CMB}/u_B \sim 10^{-3}$ smaller than those seen at X-ray energies ($\nu F_\nu \lesssim 10^{-12}$ erg/cm/s). This TeV emission would thus be below the flux sensitivity limit of current γ-ray instruments.

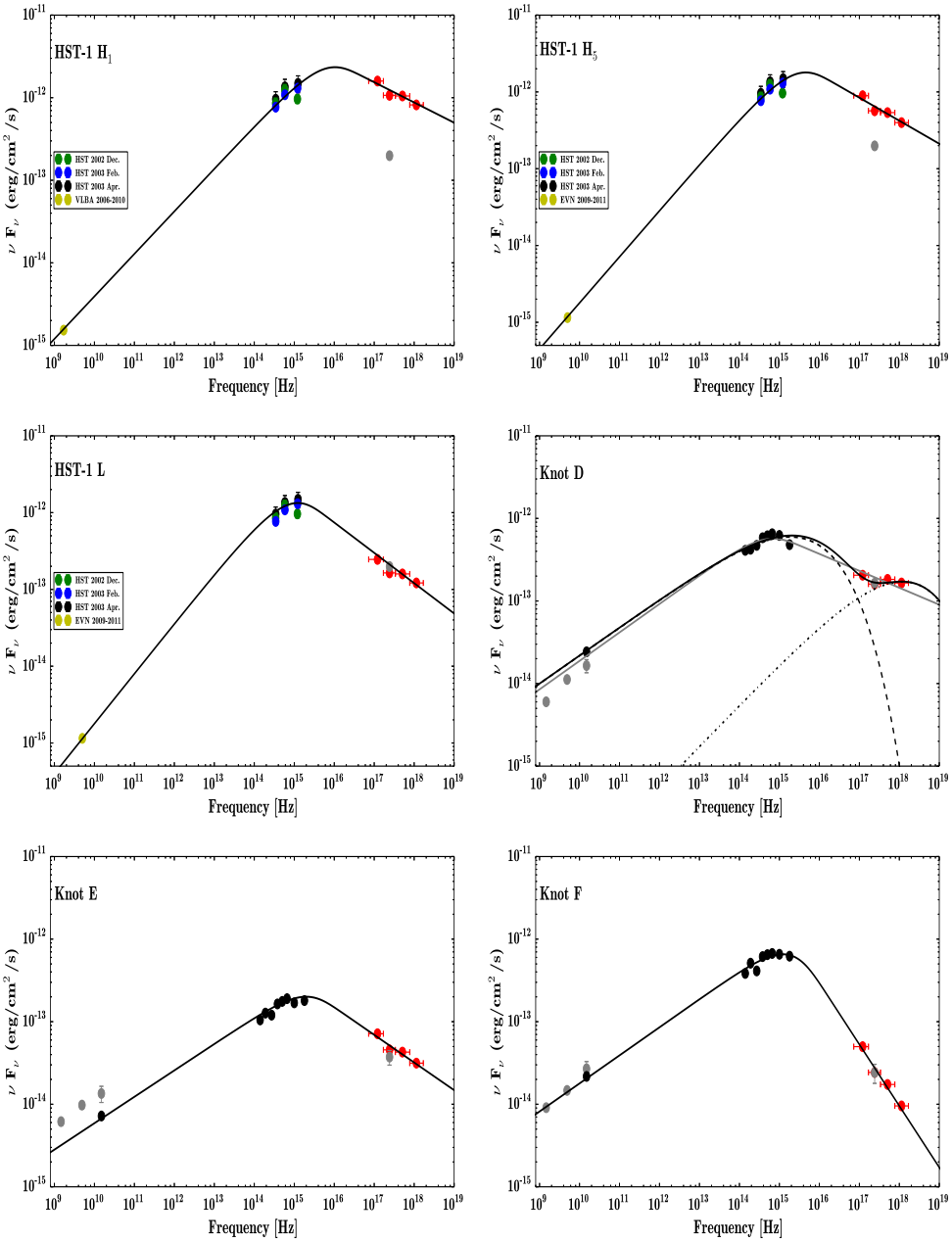

Figure 3.6: SEDs fitting results assuming a synchrotron origin of the X-ray emission. The curves represent the best fit models. For the knots D, B, and C both a broken power-law fit and a fit based on two exponential cutoff power-law components (dashed and dot-dashed curves, with superposition corresponding to the solid curve) assuming $\beta = 1$ are shown. The X-ray flux densities from Marshall et al. (2002) are also plotted with grey symbol for comparison.

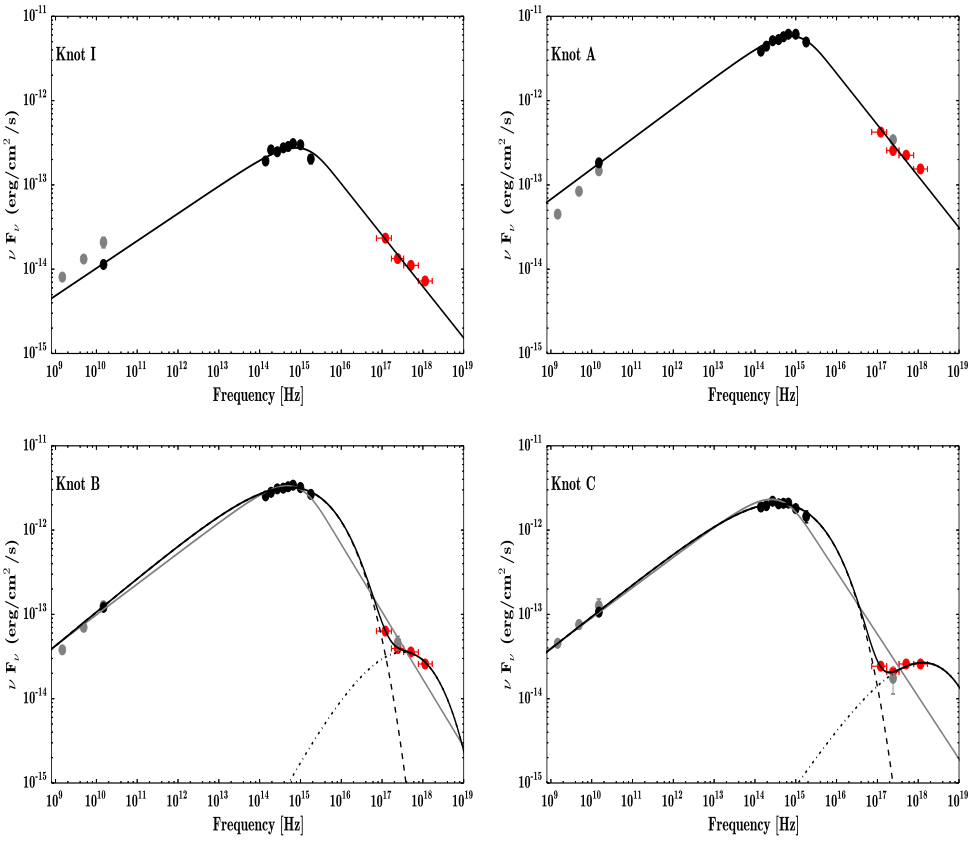

Figure 3.6 — continued

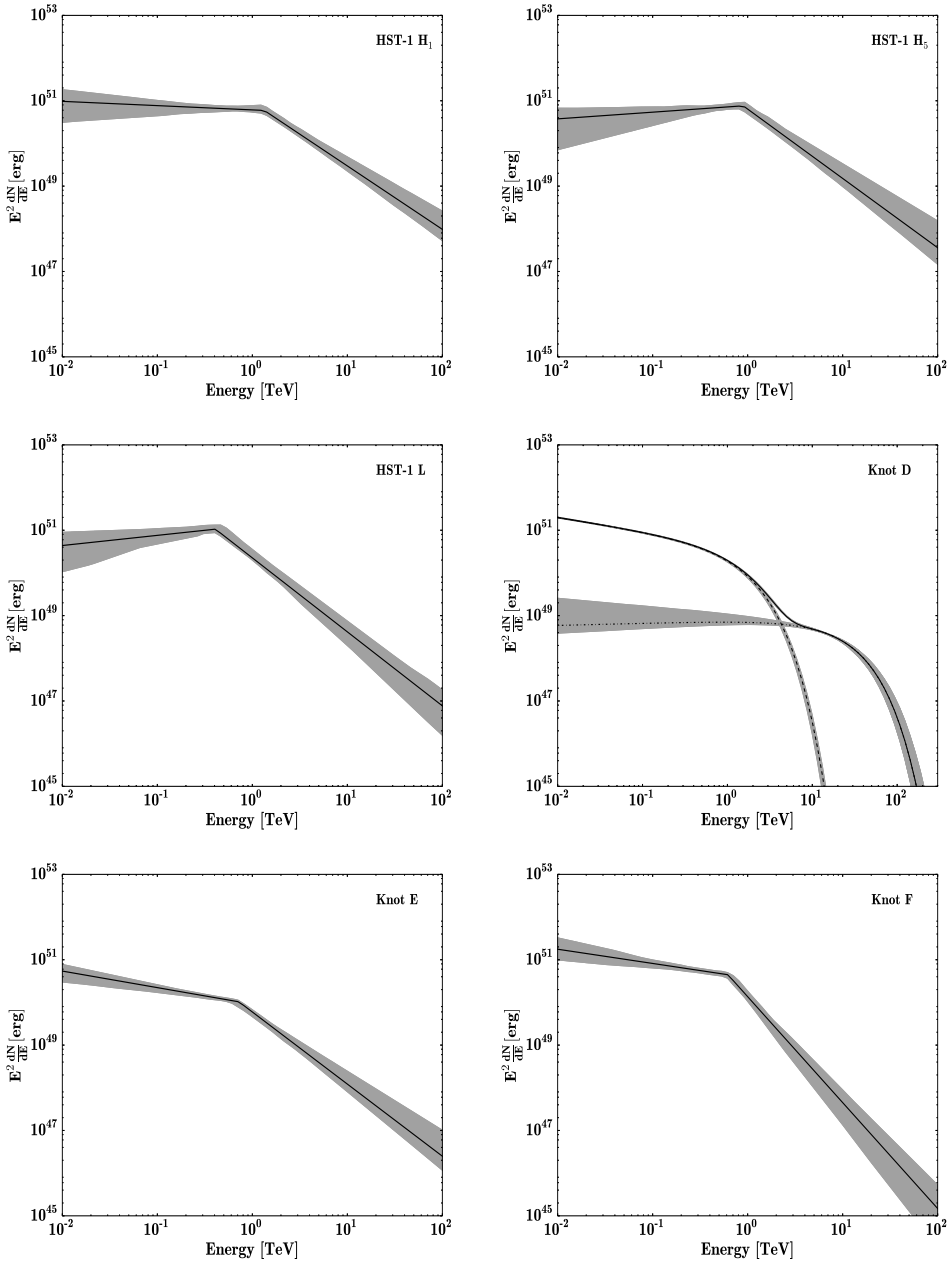

Figure 3.7: Parent electron distributions derived from the fitting in Fig. 3.6. For knots D, B, and C only the results of the two exponential cut-off power laws are shown. The grey shadow areas are corresponding to 2σ confidence level.

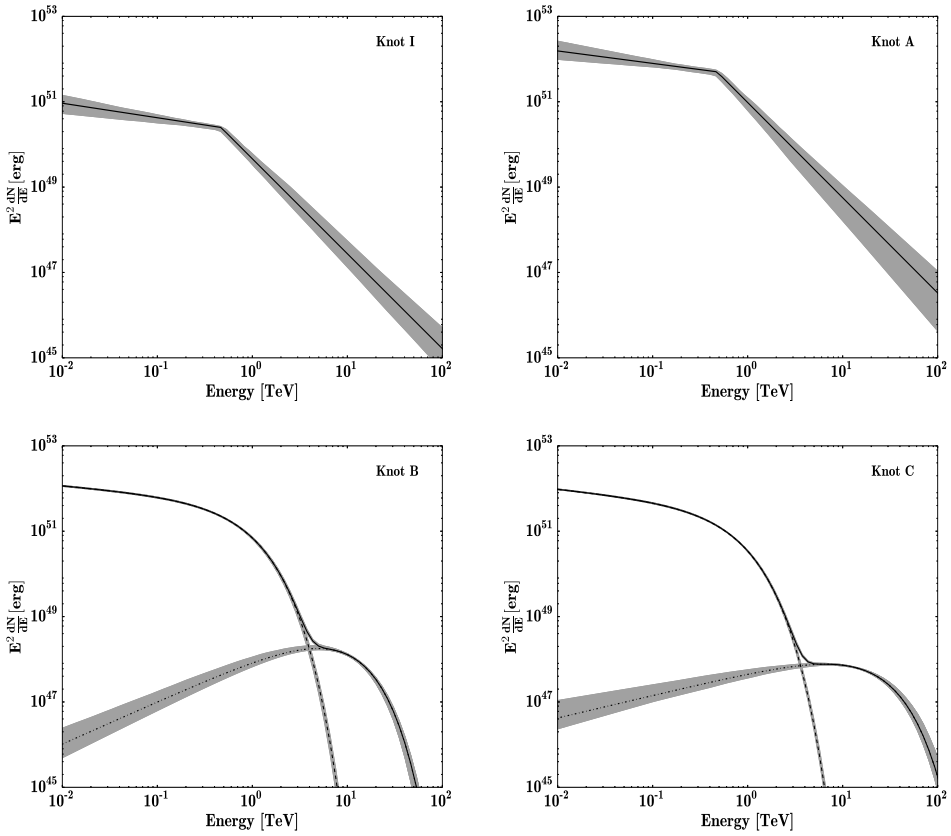

Figure 3.7 — continued

3.4 Conclusions

We have collected *Chandra* ACIS data for M87 between 2000 and 2016 with a total exposure time of about 1.5 Ms to perform a temporal and spectral analysis of its nucleus and knots. The extracted X-ray light curves of the nucleus and HST-1 reveal significant variability. We confirm indications for day-scale nuclear X-ray variability contemporaneous to the TeV flare in April 2010. HST-1 shows a decline in X-ray flux since 2007 compatible with its synchrotron origin.

The X-ray spectra of the nucleus and jet knots are all formally compatible with a single power-law. The resultant X-ray photon index reveal a trend, with index variations ranging from $\simeq$ 2.1 (e.g. in knot D) to $\simeq$ 2.4 – 2.6 (in the outer knots F, A, and B). When placed in a multi-band context, a more complex situation is arising. Modelling the radio to X-ray SEDs with a synchrotron model, a single broken power-law electron distribution with a break at around $E_b \sim 1$ TeV (assuming $B \sim 300\mu$G) seemingly allows a satisfactorily SED description for most knots. However, for the knots B, C

Table 3.6: SEDs fit results of the knots of M87. Results of the two-component fit are shown for knots D, B and C.

Component	$W_e(>1\text{GeV})$ ($\times10^{51}$ erg)	α_1	E_{break} (GeV)	α_2
HST-1 H_1	$6.5^{+1.3}_{-1.9}$	$2.08^{+0.06}_{-0.12}$	1300±60	3.49±0.07
HST-1 H_5	3.8±0.5	$1.85^{+0.06}_{-0.09}$	900^{+60}_{-80}	3.63±0.09
HST-1 L	$4.4^{+0.7}_{-0.5}$	1.77±0.07	460^{+20}_{-30}	3.83±0.08
E	$3.1^{+0.4}_{-0.6}$	$2.37^{+0.03}_{-0.06}$	680^{+40}_{-50}	3.65±0.07
F	10.1±1.4	2.33±0.04	630±30	4.52±0.10
I	5.2±0.8	$2.34^{+0.04}_{-0.03}$	470±20	4.23±0.08
A	90^{+14}_{-8}	$2.3^{+0.04}_{-0.03}$	480±20	$4.25^{+0.12}_{-0.08}$

	Component	$W_e(>1\text{GeV})$ ($\times10^{51}$ erg)	α_1	$E_{cutoff1}$ (GeV)	α_2	$E_{cutoff2}$ (GeV)
$\beta=1$	D	$11.3^{+0.13}_{-0.08}$	2.32±0.01	1130±40	2.0±0.10	19400^{2000}_{-1700}
	B	62.2±0.6	2.20±0.01	521±9	1.05±0.05	4900±200
	C	51.2±0.4	2.24±0.01	443±5	1.51±0.07	13100±1100
$\beta=2$	D	11.1±1.6	2.36±0.04	1110±50	2.14±0.07	16200±700
	B	58^{+9}_{-4}	2.33±0.03	1150^{+50}_{-60}	0.92±0.04	8000±400
	C	49±5	2.32±0.03	640±30	$1.75^{+0.04}_{-0.05}$	17200±800

All errors are 1σ confidence level.

and D an additional high energy component is needed to account for the broadband SEDs. This may be partly due to a blending of different (non-resolved) components and/or the occurrence of additional acceleration and emission processes.

A favorable interpretation for the origin of the X-ray emission is the synchrotron radiation of relativistic electrons. This requires electrons to be able to reach and sustain energies of $\gamma \sim 10^8\,(300\mu\text{G}/B)^{1/2}$ in the presence of losses, i.e. an in-situ acceleration of electrons in the jet and its knots. The necessary acceleration efficiency η, defined by $t_{\text{acc}} = \gamma m_e c/(\eta eB)$ (Aharonian et al., 2002), would be of the order of $\eta \gtrsim 3\times10^{-4}$ $(B/300\mu\text{G})$, and likely to be in the reach of stochastic acceleration scenarios (e.g., Rieger et al., 2007). Localized (first order Fermi) shock acceleration alone, however, would not be sufficient given the fact that here is little evidence for e.g. the inter-knot regions to have significantly steeper spectra than the adjacent knots.

The homogeneous broken power-law model exhibits a change in indices exceeding that induced by simple cooling effects. Assuming a continuous power-law injection Perlman & Wilson (2005) have suggested that an energy-dependent filling factor $f_{acc}(\gamma) \propto \gamma^{-\xi}$ of the acceleration regions (with $\xi \sim 0.3$, i.e. occupying a smaller fraction at higher energies), might account for these breaks. Alternative explanations could be a spatial varied propagation of the

relativistic electrons or a different particle injection spectrum in different energy band. However, to some extent, all of these assumptions are ad hoc and detailed modelling as well as an advanced morphological analysis in different energy bands would be required to further qualify them.

There are clear indications that in the case of knots B, C, and D, an additional electron contribution is needed to account for the X-ray emission in a multi-band context. We formally cannot rule out the possibility that the SEDs of other knots are also produced by a two (or more) component electron distribution, though the smoothness of the fits might seem to argue for the opposite, i.e. there is no evidence for the X-ray emission in these knots to consist of separate spectral components.

The additional electron component indicated in the case of knots B, C and D is consistent with a bump or a spike-like feature at high energy. This appears compatible with a scenario where electron acceleration occurs in a shear layer under the condition of efficient radiative losses (Ostrowski, 2000). The short cooling time of relativistic electrons generally requires that in addition to a (possible) localized shock-type scenario there must be some distributed in situ acceleration occurring along the jet. Stochastic or shear acceleration could present a natural explanation for this (e.g., Liu et al., 2017). There is circumstantial evidence for a decreased thermal gas emissivity along the jet that appears consistent with the dynamical effects of a cocoon dominated by cosmic rays (CR) accelerated at the shearing jet side boundary (Dainotti et al., 2012). The hint for a CR cocoon and the spectral shape of the relativistic electrons in these knots could indicate that efficient shear acceleration indeed takes place along the jet in M87, which seems to link well into the broader evidence for a stratified or spine-sheath flow (e.g., Perlman et al., 1999).

4 On the Energy Distribution of Relativistic Electrons in the Young Supernova Remnant G1.9+0.3

4.1 Introduction

SNRs are believed to be the sites where the bulk of GCRs are accelerated up to PeV energies (1 PeV = 10^{15} eV) (see, e.g., Hillas, 2013; Blasi, 2013). In recent years, significant progress has been achieved in the context of exploring the CR acceleration in SNRs, in particular using the γ-ray observations in the MeV/GeV and TeV energy bands (see, e.g., Aharonian, 2013). In particular, the detection of the so-called π^0-decay bump in the spectra of several mid-age SNRs (see, e.g., Abdo et al., 2010c,d; Aharonian, 2013; Ackermann et al., 2013), is considered as a substantial evidence of acceleration of protons and nuclei in SNRs. Moreover, the detection of more than ten young (a few thousand years old or younger) SNRs in TeV γ-rays (see, e.g., Zirakashvili & Aharonian, 2010; Inoue et al., 2012; Abdo et al., 2010a; Aharonian, 2013) highlights these objects as efficient particle accelerators, although the very origin of γ-rays (leptonic or hadronic?) is not yet firmly established. More disappointingly, so far all TeV emitting SNRs do not show energy spectra that would continue as a hard power-law beyond 10 TeV. For a hadronic origin of detected γ-rays, the "early" cutoffs in the energy spectra of γ-rays around or below 10 TeV imply a lack of protons inside the shells of SNRs with energies significantly larger than 100 TeV, and, consequently, SNRs do not operate as PeV accelerators (PeVatrons). However, there are two possibilities that would allow us to avoid such a dramatic conclusion for the current paradigm of Galactic CRs:

(i) The detected TeV gamma-rays are of leptonic (Inverse Compton) origin. Of course, alongside with the relativistic electrons, protons and nuclei can (should) be accelerated as well, but we do not see the related γ-radiation because of their ineffective interactions caused by the low density of ambient

gas;

(ii) SNRs do accelerate protons to PeV energies, however it occurs at early stages of evolution of SNRs when the shock speeds exceed 10,000 km/s; we do not see the corresponding radiation well above 10 TeV because the PeV protons have already left the remnant.

Both these scenarios significantly limit the potential of γ-ray observations for the search for CR PeVatrons. Fortunately, there is another radiation component which contains an independent and complementary information about these extreme accelerators. It is related to the synchrotron radiation of accelerated electrons, namely to the shape of the energy spectrum of radiation in the cutoff region, which can serve as a distinct signature of the acceleration mechanism and its efficiency. In the shock acceleration scheme, the maximum energy of accelerated particles, $E_0 \propto B\, v_{\rm sh}^2$ (Aharonian & Atoyan, 1999). Therefore, the epoch of the first several hundred years of evolution of a SNR, when the shock speed $v_{\rm sh}$ exceeds 10,000 km/s and the magnetic field is large $B \gg 10\,\mu$G could be an adequate stage for operation of a SNR as a PeVatron, provided, of course, that the shock acceleration proceeds close to the Bohm diffusion limit (see, e.g., Malkov & Drury, 2001). Remarkably, in this regime, the cutoff energy in the synchrotron radiation of the shock-accelerated electrons is determined by a single parameter, $v_{\rm sh}^2$ (Aharonian & Atoyan, 1999; Zirakashvili & Aharonian, 2007). Therefore, for the known shock speed, the position of the cutoff contains unambiguous information about the acceleration efficiency. For $v_{\rm sh} \simeq 10,000$ km/s, the synchrotron cutoff in the spectral energy distribution (SED) is expected around 10 keV. Thus, the study of synchrotron radiation in the hard X-ray band can shed light on the acceleration efficiency of electrons, and, consequently, provide an answer as to whether or not these objects can operate as CR PeVatrons, given that in the shock acceleration scheme the acceleration of electrons and protons is expected to be identical. In this regard, G1.9+0.3 (X-ray morphology $\sim 100''$ and radio morphology $\sim 84''$), the youngest known SNR in our Galaxy (Reynolds et al., 2008; Green et al., 2008), is a perfect object to explore this unique tool.

The X-ray observations with the *Chandra* and *NuSTAR* satellites (Reynolds et al., 2009; Zoglauer et al., 2015) cover a rather broad energy interval which is crucial for the study of the spectral shape of synchrotron radiation, in particular in the cutoff region. Such a study has been conducted by the team of the *NuSTAR* collaboration (Zoglauer et al., 2015).

In this chapter we present the results of our own analysis of the *NuSTAR* and Chandra data with an emphasis on the study of the SED of X-ray radiation over two decades, from 0.3 keV to 30 keV. Using the synchrotron

spectrum and the Markov Chain Monte Carlo (MCMC) technique, we derive the energy distribution of electrons responsible for X-rays, and discuss the astrophysical implications of the obtained results.

4.2 X-ray Observations

The recent hard X-ray observations of G1.9+0.3 by the *NuSTAR* satellite are uniquely useful for understanding acceleration and radiation processes of ultrarelativistic electrons in SNRs at the early stages of their evolution. Detailed study of the *NuSTAR* data, combined with the *Chandra* observations at lower energies, has been comprehensively carried out by Zoglauer et al. (2015). In particular, it was found that the source can be resolved into two bright limbs with similar spectral features. The combined Chandra and *NuSTAR* datasets have been claimed to be best described by the so-called *srcut* model (Reynolds, 2008) or by the power-law function with an exponential cutoff. The characteristic cutoff energies in these two fits have been found around 3 keV and 15 keV, respectively (Zoglauer et al., 2015).

To further investigate the features of the X-ray spectrum in the cutoff region we perform an independent study based on the publicly available Chandra and *NuSTAR* X-ray data. For *NuSTAR*, we use the set of three observations with ID 40001015003, 40001015005, and 40001015007, including both the focal plane A (FPMA) and B (FPMB) modules. The data have been analysed using the HEASoft version 6.16, which includes NuSTARDAS, the *NuSTAR* Data Analysis Software package (the version 1.7.1 with the *NuSTAR* CALDB version 20150123). For the Chandra data, we use the ACIS observations with ID 12691, 12692, and 12694. The Chandra data reduction is performed using the version 4.7 of the CIAO package.

In Figure 4.1 we show the X-ray sky map above 3 keV based on the *NuSTAR* 40001015007 data set. In order to benefit from the maximum possible statistics, for the spectral analysis we have chosen the entire remnant. The background regions are selected in a way to minimise the contamination caused by the PSF wings as well as from the stray light. The excess in the south of the FPMA image is the stray light from X-rays that hit the detector without impinging on the optics (Wik et al., 2014). We use the same source regions for Chandra observations. The results of our study of the spatial distribution of X-rays appear quite similar to those reported by (Zoglauer et al., 2015). Therefore, in this work we do not discuss the morphology of the source but focus on the study of spectral features of radiation.

The spectral shape of synchrotron radiation in the cutoff region is sensitive to the spectrum of highest energy electrons which, in turn, depends on

the electron acceleration and energy loss rates. To explore a broad class of spectra, we describe the spectrum of X-rays in the following general form:

$$\frac{\mathrm{d}N}{\mathrm{d}\epsilon} = AE^{-\Gamma}\exp[-(\epsilon/\epsilon_0)^{\beta}]\,. \tag{4.1}$$

The change of the index β in the second (exponential) term allows a broad range of spectral behaviour in the cutoff region. For example, $\beta = 0$ implies a pure power-law distribution, while $\beta = 1$ corresponds to a power-law with a simple exponential cutoff.

In the fitting procedure, in addition to the three parameters ϵ_0, Γ, and β, one should introduce one more parameter, the column density N_{H}, which takes into account the energy-dependent absorption of X-rays. We fix this parameter to the value found by Zoglauer et al. (2015) from the fit of data by their *srcut* spectral model. Strictly speaking, the best fit value of the column density should be different for different spectral models. To check the impact of different spectral models on the column density, we adopt different functions leaving the column density as a free parameter in the fitting procedure. We find that the difference of the best fit column density and the above fiducial value is less than several percent. Therefore, in order to keep the procedure simple and minimise the number of free parameters, we adopt the value 7.23×10^{22} cm^{-2} from the paper of Zoglauer et al. (2015).

The results of our fit of the *NuSTAR* and Chandra spectral points using the model "power-law with an exponential cutoff" in the general form of Eq. 4.1, that is, leaving β, Γ, and ϵ as free parameters, are shown in Table 4.1. One can see that the best fit gives a rather narrow range of the index β around 1/2. In Table 4.1 we also separately show the results of the fits with three fixed values of β: 0, 1/2, and 1. While the pure-power-law spectrum ($\beta = 0$) can be unambiguously excluded, the model of power-law with a simple exponential cutoff ($\beta = 1$) is not favourable either. It is excluded at the 3σ statistical significance level. In summary, the combined Chandra and *NuSTAR* data are best described by the index $\beta \approx 0.5$ and $\epsilon_0 \approx 1.5$ keV.

Whereas $\beta = 1/2$ seems to be a natural outcome (see below), the cutoff energy around 1.5 keV is a rather unexpected result. Namely, it implies that the acceleration of electrons in G1.9+0.3 proceeds significantly slower than one would anticipate given the very large, 14,000 km/s shock speed (Borkowski et al., 2010). This can be seen from the comparison of the SED of G1.9+0.3 with one of the most effective particle accelerators in our Galaxy, ≈1600 year old SNR RX J1713.4-3946 (see Figure 4.2). The cutoff energy in the synchrotron spectrum of shock-accelerated electrons is proportional to the square of shock speed v_{sh}^2 (Aharonian & Atoyan, 1999). Therefore, in order to exclude the difference in the cutoff energies caused by the difference in the shock speeds, we rescale the energies of the spectral points of

RX J1713.4-3946 by the factor $(v_{\rm sh}/14,000\ {\rm km/s})^2$, where the shock speed of RX J1713.4-3946 is about $v_{\rm sh} \simeq 4,000$ km/s (Uchiyama et al., 2007). After such a normalisation, the cutoff energy of RX J1713.4-3946 becomes an order of magnitude higher than the cutoff in G1.9+0.3. The acceleration of electrons in RX J1713.4-3946 proceeds close to the Bohm diffusion limit thus providing an acceleration rate close to the maximum value (Uchiyama et al., 2007; Zirakashvili & Aharonian, 2010). Consequently, we may conclude that the current acceleration rate of electrons in G1.9+0.3 is lower, by an order of magnitude, compared to the maximum possible rate.

It should be noted that the physical meaning of Eq.(4.1) doesn't be overestimated. Namely, it should be considered as a convenient analytical presentation of the given set of measured spectral points. Consequently, $\Gamma, \beta, \epsilon_0$ that enter into Eq.(4.1) should be treated as a combination of formal fit parameters rather than physical quantities. For example, ϵ_0 in the exponential term of Eq.(4.1) doesn't necessarily coincide with the cutoff energy (or maximum in the SED). Indeed, in different $(\Gamma, \beta, \epsilon_0)$ combinations describing the same spectral points, the parameter ϵ_0 could have significantly different values. Analogously, Γ should not be treated as a power-law index but rather a parameter which, in combination with Γ and β, determines the slope (the tangential) of the spectrum immediately before the cutoff region.

The maximum acceleration rate of particles is achieved when it proceeds in the Bohm diffusion limit. In the energy-loss-dominated regime, the spectra of synchrotron radiation can be expressed by simple analytical formulae (Zirakashvili & Aharonian, 2007). Because of compression of the magnetic field, the overall synchrotron flux of the remnant is dominated by the radiation from the downstream region (see Figure 4.3). The SED of the latter can be presented in the following form (Zirakashvili & Aharonian, 2007)

$$\epsilon^2 \frac{{\rm d}N}{{\rm d}\epsilon} \propto \epsilon^2 (\epsilon/\epsilon_0)^{-1} [1 + 0.38(\epsilon/\epsilon_0)^{0.5}]^{11/4} \exp[-(\epsilon/\epsilon_0)^{1/2}] \,. \tag{4.2}$$

with

$$\epsilon_0 = \hbar\omega_0 = \frac{2.2\ {\rm keV}}{\eta(1+\kappa^{1/2})^2} \left(\frac{u_1}{3000\ {\rm km}\ s^{-1}}\right)^2 \,, \tag{4.3}$$

where η takes into account the deviation of the diffusion coefficient from its minimum value (in the nominal Bohm diffusion limit $\eta = 1$). In the standard shock acceleration theory, the momentum index of accelerated electrons $\gamma_{\rm s} = 4$, and the ratio of the upstream and downstream magnetic fields, $\kappa = 1/\sqrt{11}$.

In Figure 4.3 the spectral points of G1.9+0.3 are compared with the theoretical predictions for synchrotron radiation in the upstream and downstream regions (Zirakashvili & Aharonian, 2007), the asymptotic forms of the electron spectra in the case of Bohm diffusion are given in Appendix C. The

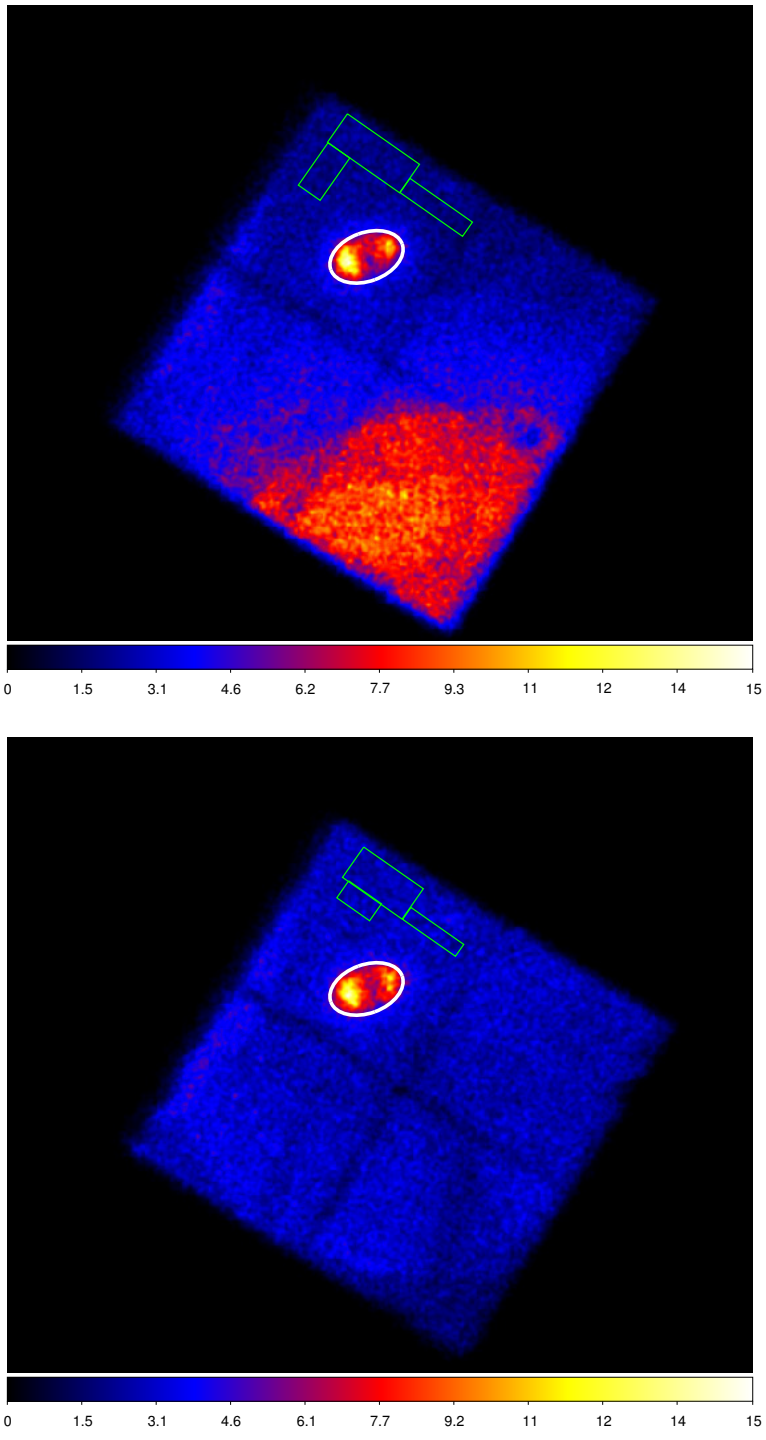

Figure 4.1: Images from the observation 40001015007 for the FPMA (top) and FPMB (bottom) modules. The source and background regions are indicated by the white and green contours, respectively.

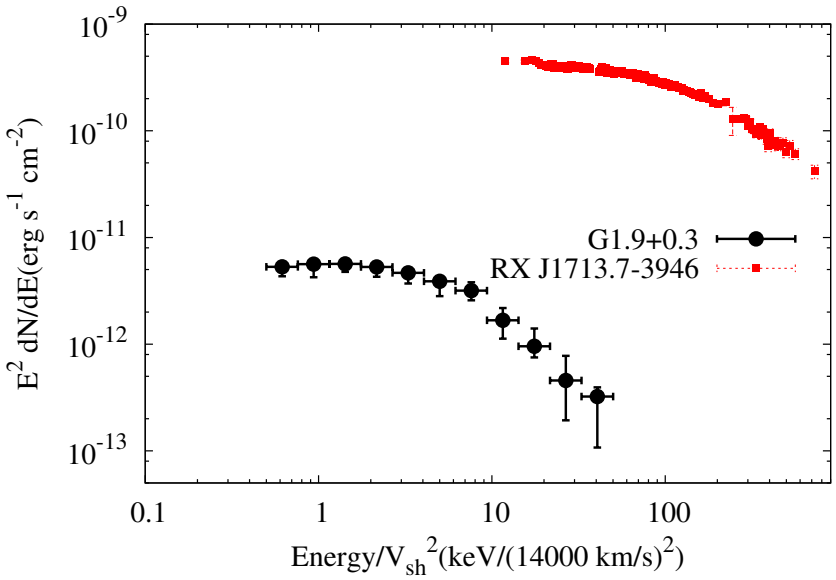

Figure 4.2: The spectral points of G1.9+0.3 (this work; black circles) and RX J1713.4-3946 (red square) from Tanaka et al. (2008). The energies of the points of RX J1713.4-3946 are rescaled by the factor of the square of the ratio of shock speeds of J1713.4-3946 and G1.9+0.3: $(14,000\ \mathrm{km/s}/4000\ \mathrm{km/s})^2 = 12.25$.

calculations are performed for two values of the parameter η characterising the acceleration efficiency: $\eta = 1$ (Bohm diffusion regime) and 20 times slower ($\eta = 20$). The good (better than 20 %) agreement of the spectral points with the theoretical curves for $\eta = 20$ tells us that in G1.9+0.3 electrons are accelerated only at the 5 % efficiency level.

Although in the paper of Zoglauer et al. (2015) the spectral points are not explicitly presented, thus the direct comparison with our results is not possible, the conclusions of our study on the energy spectrum of G1.9+0.3 seems to be in agreement with the results of Zoglauer et al. (2015).

Table 4.1: Spectral fitting results for G1.9+0.3

Model	PL index	Cutoff (keV)	β	$\chi^2/d.o.f.$
PL	2.54 (2.52 - 2.56)			1089.4/666
PL+ecut	2.04 (1.98 - 2.10)	11.8 (10.5 - 13.3)		697.7/665
PL+ecut (β=0.5)	1.65 (1.60 - 1.70)	1.68 (1.50 - 1.90)	0.5	686.2/665
PL+ecut (β free)	1.62(1.48 - 1.75)	1.41 (1.30-1.55)	0.48 (0.40-0.56)	685.8/664

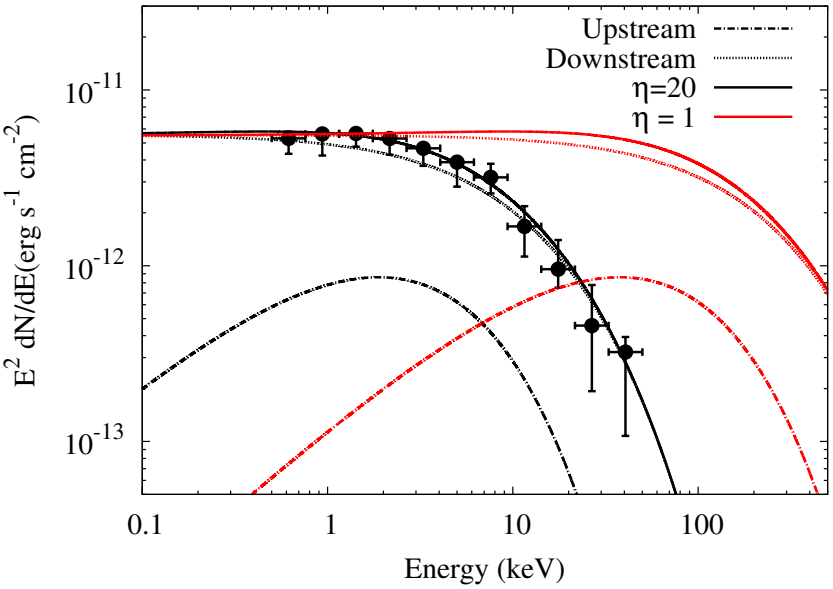

Figure 4.3: The spectral points of G1.9+0.3 (this work) compared to the predictions of synchrotron radiation of the shock accelerated electrons in the downstream and upstream regions (Zirakashvili & Aharonian, 2007) for two regimes of diffusion: (1) Bohm diffusion, $\eta = 1$ and (2) 20 times faster diffusion, that is, $\eta = 20$.

4.3 Relativistic Electrons and Magnetic Fields

The joint treatment of X-ray and γ-ray data, under the simplified assumption that the same electron population is responsible for the broad-band radiation through the synchrotron and inverse Compton channels, provides information about the magnetic field and the total energy budget in relativistic electrons. G1.9+0.3 has been observed in VHE γ-ray band with the H.E.S.S. Cherenkov telescope system. Although no positive signal has been detected (H.E.S.S. Collaboration et al., 2014), the γ-ray flux upper limits allow meaningful constraints on the average magnetic field in the X-ray and γ-ray production region. For calculations of the broad-band SED, we adopt the same background radiation fields used in the paper H.E.S.S. Collaboration et al. (2014): the infrared component with a temperature of 48 K and energy density of 1.5 eVcm^{-3}, and the optical component with a temperature of 4300 K and the energy density of 14.6 eVcm^{-3}. The comparison of model calculations with observations (see Figure 4.4) gives a lower limit of the magnetic field, $B \geq 17\mu$G.

Under certain assumptions, the magnetic field can be constrained also based only on the X-ray data. In the "standard" shock acceleration scenario, electrons are accelerated with the power-law index $\alpha = 2$. However because

of the short radiative cooling time, their spectrum of highest energy electrons (the X-ray producers) becomes steeper, $\alpha = 2 \rightarrow 3$. Consequently, in the downstream region, where the bulk of the synchrotron radiation is produced, X-rays have a photon index $\Gamma = 2$. The synchrotron cooling time can be expressed through the magnetic field and the X-ray photon energy: $t_{\rm synch} \simeq 50(B/100\mu{\rm G})^{-3/2}(\epsilon/1\,{\rm keV})^{-1/2}$ years. Thus for $\epsilon \sim 1$ keV and the age of the SNR ~ 150 yr, we find that the magnetic field should be larger than 50 μG.

The combined Chandra and *NuSTAR* data cover two decades in energy, from sub-keV to tens of keV. This allows derivation of the energy distribution of electrons, $W(E) = E^2 {\rm d}N_{\rm e}/{\rm d}E$ in the most interesting region around the cutoff. The results shown in Figure 4.5 are obtained using the Markov Chain Monte Carlo (MCMC) code *Naima* developed by V. Zabalza [1]. It is assumed that the magnetic field is homogeneous both in space and time. The results shown in Figure 4.5 are calculated for the fiducial value of the magnetic field $B = 100\,\mu$G, however they can be rescaled for any other value of the field. We note that while the shape of the spectrum does not depend on the strength of the magnetic field, the energies of individual electrons scale as $E \propto B^{-1/2}$, and the total energy contained in electrons scales as $\propto B^{-2}$. Since, in the "standard" diffusive shock acceleration (DSA) scenario the synchrotron X-ray flux is contributed mainly by the downstream region, the results in Figure 4.5 correspond to the range of the energy distribution of electrons for the same region. For comparison, the energy distribution of electrons calculated using the formalism of Zirakashvili & Aharonian (2007) is shown.

4.4 Conclusions

SNRs are believed to be the major contributors to the Galactic CRs. The recent detections of TeV emission from more than ten young SNRs (of the age of a few thousand years or younger), demonstrates the ability of these objects to accelerate particles, electrons and/or protons, to energies up to 100 TeV. Yet, we do not have observational evidence of the extension of hard γ-ray spectra well beyond 10 TeV. Therefore one cannot claim an acceleration of protons and nuclei by SNRs to PeV energies. On the other hand, one cannot claim the opposite either, given the possibility that the acceleration of PeV protons and nuclei could happen at the early stages of evolution of SNRs when the shock speeds exceed 10,000 km/s. Indeed, the theoretical studies of recent years show that the best candidates for accelerators operating as PeVatrons are very young (less than 100 years old) supernova remnants in dense environments (see e.g. (Schure & Bell, 2013)). Then, the escape of the

[1] https://github.com/zblz/naima

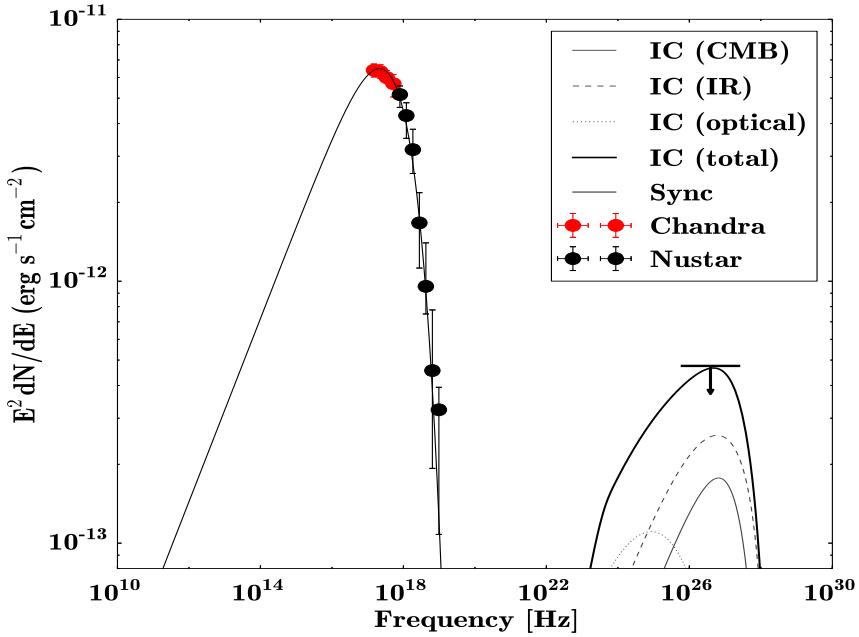

Figure 4.4: X-ray SED as well as the VHE upper limit from H.E.S.S. Collaboration et al. (2014). The curves are the synchrotron and IC emissions fitted to derive the lower limit of the magnetic field.

highest energy particles at later stages of evolution of SNRs can explain the spectral steepening of γ-ray spectra at multi-TeV energies from $\geq$ 1 thousand year old remnants.

In this regard, the youngest known SNR in our Galaxy, G1.9+0.3, with a measured shock speed of 14,000 km/s, seems to be a unique object in our Galaxy to explore the potential of SNRs for acceleration of protons and nuclei to PeV energies. Such measurements have been performed with the H.E.S.S. array of Cherenkov telescopes. Unfortunately, no positive signal has been detected. On the other hand, the recent observations of G1.9+0.3 in hard X-rays by *NuSTAR* provide unique information about the acceleration efficiency of electrons. Together with Chandra data at lower energies, these data allow model-independent conclusions. Although the general shape of the energy spectrum of X-rays is in a very good agreement with predications of the diffusive shock-acceleration theory, the acceleration rate appears an order of magnitude slower relative to the maximum acceleration rate achieved in the nominal Bohm diffusion limit.

It should be noted that the deviation from the Bohm diffusion concerns not only the larger absolute value of the diffusion coefficient, but also the energy dependence of the latter. The diffusion coefficient written in the con-

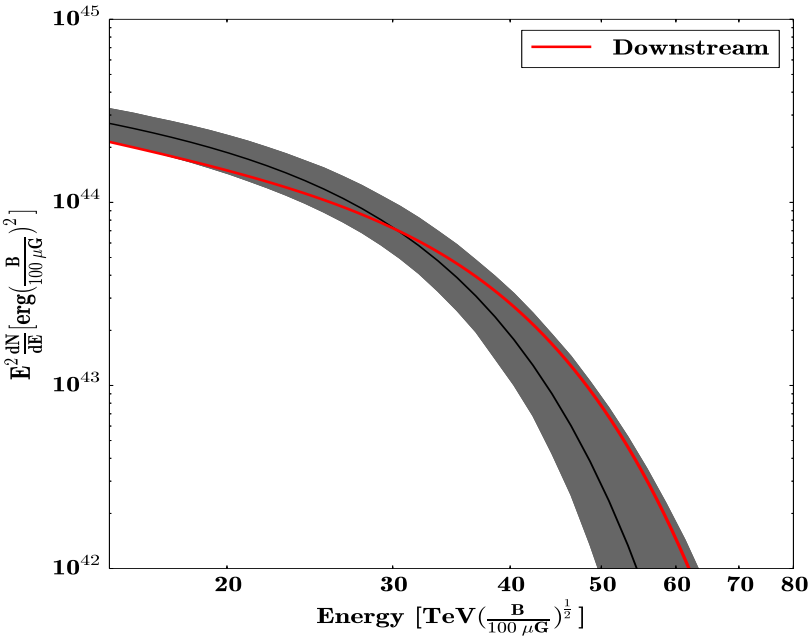

Figure 4.5: Electron spectrum from the X-ray data points (black curve and shaded area) and theoretically predicted integrated electron spectrum in young SNR (red curve) assuming a fast diffusion, i.e., $\eta = 20$ in Eq.1. Also shown is the contribution from the downstream region.

ventional form $D(E) \propto E^{\lambda}$, allows consideration of diffusion in a broad range of acceleration regimes. Then, in the synchrotron-loss-dominated regime, the energy distribution of electrons in the cutoff region has an exponential form, $N(E) \propto \exp[-(E/E_0)^{\beta_e}]$ with $\beta_e = \lambda + 1$ (see Eq.(19) from Zirakashvili & Aharonian (2007)). Correspondingly, the index β characterising the spectrum of synchrotron radiation in the cutoff region, is $\beta = (1+\lambda)/(3+\lambda)$. In particular, the values of λ =0, 1/3, and 1, which correspond to the energy-independent, Kolmogorov, and Bohm diffusion regimes, give β =1/3, 2/5, and 1/2, respectively. We note that the energy-independent diffusion in the synchrotron-loss-dominated regime results in a X-ray spectrum similar to the one formed in the case of the Bohm diffusion but in the age-limited regime. However, strictly speaking, because of the escape, the electrons in the age-limited regime of acceleration should have a steeper spectrum[2], that is, $\beta_e \geq 1$. Although the results of the current analysis give a preference to the

[2]This statement is correct for the epochs when the electrons start to escape the shell. The case of formation of the electron spectrum in the age-limited regime at the presence of particle escape has not been yet quantitatively explored in the literature. However, since the probability of the electron escape increases with energy, it is clear that the escape should make the spectrum of particles inside the accelerator steeper.

interval of $\beta = 0.4 - 0.56$, the value of 1/3 cannot be excluded (see Table 4.1).

To a certain extent, the relatively low acceleration rate of electrons in G1.9+0.3, in terms of the nominal rate of acceleration in the Bohm diffusion limit (for the given speed of the shock), is a surprise outcome, especially when compared with SNRs in which the acceleration of electrons proceeds in the regime close to the Bohm diffusion. For comparison, the detailed modelling of young SNRs Cas A (Zirakashvili et al., 2014) and RX J1713.4-3946 (Zirakashvili & Aharonian, 2010) shows that the η parameter characterising the acceleration efficiency cannot significantly deviate from $\eta = 1$. If the acceleration of protons and nuclei proceeds in the same manner as the electron acceleration, this result would imply inability of G1.9+0.3 to operate as a PeVatron. Apparently, the observations of G1.9+0.3 alone are not sufficient to decide whether this conclusion can be generalised for other SNRs.

5 Summary and Prospect

In this thesis I have investigated the non-thermal phenomena of three individual astrophysical objects: the radio galaxies Centaurus A and M87, and the SNR G1.9+0.3. I analysed the broadband observational data and studied the corresponding radiation mechanism and acceleration process.

In Chapter 2, we have analyzed the hundred kpc-scale giant lobes of the closest radio galaxy Cen A in the γ-ray band with *Fermi*-LAT, and in the radio band with *Planck*. The morphologies of the giant lobes at γ-ray and radio frequencies are different, the probable reasons are the effects of the magnetic field in the synchrotron radiation or the different electron populations that responsible for the two energy bands. We have divided each lobe into three regions, and extracted the corresponding spectra in γ-ray energy band. We find significant spectral variations between regions. In addition, we find that the power-law shape of the SED, which extends down to 100 MeV, couldn't be explained by hadronic origin of the emission. Combining *Planck* and *Fermi*-LAT data, the radiation mechanism of the SED in each region has been discussed. We find that the γ-ray emission for all regions, except for the outermost region of south lobe S1, can be fitted with IC scattering of electrons on the CMB photons and an non-negligible contribution from the EBL photons. The radiation characteristics of region S1 are quite different from the other regions. Although the SED of region S1 could also be explained within a simple leptonic model, a magnetic field $B \simeq 13\ \mu$G, an order of magnitude larger than the average field, is required, and the derived total energy of electrons is much smaller than that in the other regions. The p-p collisions followed by pion decay could account for the data at higher γ-ray energies for all regions, but the overall energy required in relativistic protons is huge. This could be reduced if the interactions takes place primarily in the filamentary structures of the lobes. The propagation length of the relativistic electrons is far less than the size of the lobe, so the electrons need to be accelerated in situ, e.g. by the stochastic acceleration in a turbulent

magnetic field. By far, the signals of the giant lobes of Cen A from radio to HE γ-ray energy band have been well detected and studied. However, for the VHE emission, the localization is still uncertain and only an upper limit can be given (Aharonian et al., 2005). On the other hand, the limited field of view (FOV) of Imaging Atmospheric Cherenkov Telescopes (IACTs) prevent the detection of such extended source in VHE band. The next-generation γ-ray observatory Cherenkov Telescope Array (CTA)[1], however, with wider FOV ($\sim 10°$), better angular and energy resolution, and better sensitivity from 20 GeV to 300 TeV, would allow us to resolve the extended sources in unprecedented details. CTA observations on the giant lobes of Cen A, combining with *Fermi*-LAT data, would contain important information on the spectra of IC emission in the cutoff region and provide unambiguous diagnosis on the particle acceleration in such an environment.

M87 is the second closest radio galaxies and its kpc-scale jet, which has been resolved by high-resolution *Chandra* telescope, carries important information on the distributions of relativistic electrons and magnetic fields. In Chapter 3, we have reanalyzed archival *Chandra* observations on the jet of M87 from 2000 to 2016 with a total exposure of 1460 kiloseconds to explore the X-ray emission characteristics along the jet. We investigate the variability behaviours of the nucleus and the inner jet component HST-1, and confirm the day-scale X-ray variability in the nucleus contemporaneous to the 2010 high TeV γ-ray state. HST-1 shows a general decline in X-ray flux over the last few years which is consistent with its synchrotron interpretation. We extract the X-ray spectra for the nucleus and all knots in the jet, showing that they are compatible with a single power-law within the X-ray band. The resultant X-ray photon indices reveal slight but significant index variations ranging from $\simeq 2.1$ (e.g. in knot D) to $\simeq 2.4-2.6$ (in the outer knots F, A, and B). When viewed in a multi-wavelength context, a more complex situation is arising. Fitting the radio to X-ray SEDs assuming a synchrotron origin, we show that a broken power-law electron spectrum with break energy E_b around $1\ (300\mu G/B)^{1/2}$ TeV allows a satisfactorily description of the multi-band SEDs for the knots HST-1, E, F, I, and A. The homogeneous broken power-law model exhibits a change in indices exceeding that induced by simple cooling effects. Perlman & Wilson (2005) have suggested that an energy-dependent filling factor $f_{acc}(\gamma) \propto \gamma^{-\xi}$ of the acceleration regions might account for these breaks. Alternative explanations could be a spatial varied propagation of the relativistic electrons or a different particle injection spectrum in different energy band. For the case of knots B, C, and D, we find indications of an additional electron contribution, in order to adequately reproduce the

[1] https://www.cta-observatory.org

multi-band SEDs. The additional electron component is consistent with a bump or a spike-like feature at high energy. We find that the stochastic or shear acceleration (e.g., Liu et al., 2017) could account for the spectral shape and short cooling time of the relativistic electrons. The existence of a cocoon structure at the jet boundary (Dainotti et al., 2012), combining the spectral shape of the relativistic electrons, could indicate that efficient shear acceleration indeed takes place along the jet in M87. Based on above implications, we suggest that a stratified or spine-sheath jet model (e.g., Perlman et al., 1999) may account for the differences. However, all of these explanations are ad hoc and detailed modelling as well as an advanced morphological analysis in different energy bands would be required to further qualify them.

In addition to the large scale outflows in AGNs, SNRs are also regarded as the site of particle acceleration. In recent years, several theoretical studies have suggested that the best candidates for accelerators operating as PeVatrons are very young SNRs in dense environments (Schure & Bell, 2013). The youngest known SNR in our Galaxy G1.9+0.3 seems to be a favoured source to investigate whether these objects are the sites of PeV Galactic CRs. Although H.E.S.S. hasn't detected a positive signal of G1.9+0.3 until now, recent observations in hard X-ray by NuSTAR can provide unique information about the acceleration efficiency of electrons. In Chapter 4, we have exploited the X-ray observations of NuSTAR and *Chandra* satellites to constrain the electrons distributions by assuming a synchrotron origin. We have found that the acceleration of electrons is an order of magnitude slower than the maximum rate provided by shock acceleration in the nominal Bohm diffusion regime. If the acceleration of protons and nuclei proceeds in the same manner as the electron acceleration, this result would then imply inability of G1.9+0.3 to operate as a PeVatron.

Bibliography

Abdo, A. A., Ackermann, M., Ajello, M., et al. 2010a, Fermi-Lat Discovery of GeV Gamma-Ray Emission from the Young Supernova Remnant Cassiopeia A, ApJ, 710, L92

Abdo, A. A., Ackermann, M., Ajello, M., et al. 2010b, Fermi Gamma-Ray Imaging of a Radio Galaxy, Science, 328, 725

Abdo, A. A., Ackermann, M., Ajello, M., et al. 2010c, Gamma-Ray Emission from the Shell of Supernova Remnant W44 Revealed by the Fermi LAT, Science, 327, 1103

Abdo, A. A., Ackermann, M., Ajello, M., et al. 2010d, Observation of Supernova Remnant IC 443 with the Fermi Large Area Telescope, ApJ, 712, 459

Abramowski, A., Acero, F., Aharonian, F., et al. 2012, The 2010 Very High Energy γ-Ray Flare and 10 Years of Multi-wavelength Observations of M 87, ApJ, 746, 151

Acero, F., Ackermann, M., Ajello, M., et al. 2015, Fermi Large Area Telescope Third Source Catalog, ApJS, 218, 23

Achterberg, A., Gallant, Y. A., Kirk, J. G., & Guthmann, A. W. 2001, Particle acceleration by ultrarelativistic shocks: theory and simulations, MNRAS, 328, 393

Ackermann, M., Ajello, M., Albert, A., et al. 2012, The Fermi Large Area Telescope on Orbit: Event Classification, Instrument Response Functions, and Calibration, ApJS, 203, 4

Ackermann, M., Ajello, M., Allafort, A., et al. 2013, Detection of the Characteristic Pion-Decay Signature in Supernova Remnants, Science, 339, 807

Ackermann, M., Albert, A., Atwood, W. B., et al. 2014, The Spectrum and Morphology of the Fermi Bubbles, ApJ, 793, 64

Aharonian, F., Akhperjanian, A., Barrio, J., et al. 2001, Evidence for TeV gamma ray emission from Cassiopeia A, A&A, 370, 112

Aharonian, F., Akhperjanian, A. G., Bazer-Bachi, A. R., et al. 2005, Observations of selected AGN with HESS, A&A, 441, 465

Aharonian, F., Akhperjanian, A. G., Bazer-Bachi, A. R., et al. 2006, Fast Variability of Tera-Electron Volt γ Rays from the Radio Galaxy M87, Science, 314, 1424

Aharonian, F. A. 2002, Proton-synchrotron radiation of large-scale jets in active galactic nuclei, MNRAS, 332, 215

Aharonian, F. A. 2013, Gamma rays from supernova remnants, Astroparticle Physics, 43, 71

Aharonian, F. A., Akhperjanian, A. G., Aye, K.-M., et al. 2004, High-energy particle acceleration in the shell of a supernova remnant, Nature, 432, 75

Aharonian, F. A. & Atoyan, A. M. 1981, Compton scattering of relativistic electrons in compact X-ray sources, Ap&SS, 79, 321

Aharonian, F. A. & Atoyan, A. M. 1999, On the origin of TeV radiation of SN 1006, A&A, 351, 330

Aharonian, F. A., Belyanin, A. A., Derishev, E. V., Kocharovsky, V. V., & Kocharovsky, V. V. 2002, Constraints on the extremely high-energy cosmic ray accelerators from classical electrodynamics, Phys. Rev. D, 66, 023005

Aharonian, F. A., Kelner, S. R., & Prosekin, A. Y. 2010, Angular, spectral, and time distributions of highest energy protons and associated secondary gamma rays and neutrinos propagating through extragalactic magnetic and radiation fields, Phys. Rev. D, 82, 043002

Aliu, E., Arlen, T., Aune, T., et al. 2012, VERITAS Observations of Day-scale Flaring of M 87 in 2010 April, ApJ, 746, 141

Alvarez, H., Aparici, J., May, J., & Reich, P. 2000, The radio continuum spectrum of Centaurus A's large-scale components, A&A, 355, 863

Anguelov, V. & Vankov, H. 1999, Electromagnetic showers in a strong magnetic field, Journal of Physics G Nuclear Physics, 25, 1755

Atoyan, A. M. & Dermer, C. D. 2003, Neutral Beams from Blazar Jets, ApJ, 586, 79

Atwood, W. B., Abdo, A. A., Ackermann, M., et al. 2009, The Large Area Telescope on the Fermi Gamma-Ray Space Telescope Mission, ApJ, 697, 1071

Avachat, S. S., Perlman, E. S., Adams, S. C., et al. 2016, Multi-wavelength Polarimetry and Spectral Study of the M87 Jet During 2002-2008, ApJ, 832, 3

Baring, M. G. & Harding, A. K. 2001, Photon Splitting and Pair Creation in Highly Magnetized Pulsars, ApJ, 547, 929

Beall, J. H. 2015, in XI Multifrequency Behaviour of High Energy Cosmic Sources Workshop (MULTIF15), 58

Bednarek, W. 1997, Gamma-rays from synchrotron pair cascades in blazars?, MNRAS, 285, 69

Begelman, M. C. & Kirk, J. G. 1990, Shock-drift particle acceleration in super-

luminal shocks - A model for hot spots in extragalactic radio sources, ApJ, 353, 66

Bell, A. R. 1978, The acceleration of cosmic rays in shock fronts. I, MNRAS, 182, 147

Berezinskii, V. S., Bulanov, S. V., Dogiel, V. A., & Ptuskin, V. S. 1990, Astrophysics of cosmic rays

Berezinskii, V. S. & Grigor'eva, S. I. 1988, A bump in the ultra-high energy cosmic ray spectrum, A&A, 199, 1

Bersanelli, M., Mandolesi, N., Butler, R. C., et al. 2010, Planck pre-launch status: Design and description of the Low Frequency Instrument, A&A, 520, A4

Biretta, J. A., Sparks, W. B., & Macchetto, F. 1999, Hubble Space Telescope Observations of Superluminal Motion in the M87 Jet, ApJ, 520, 621

Biretta, J. A., Stern, C. P., & Harris, D. E. 1991, The radio to X-ray spectrum of the M87 jet and nucleus, AJ, 101, 1632

Blakeslee, J. P., Jordán, A., Mei, S., et al. 2009, The ACS Fornax Cluster Survey. V. Measurement and Recalibration of Surface Brightness Fluctuations and a Precise Value of the Fornax-Virgo Relative Distance, ApJ, 694, 556

Blandford, R. & Eichler, D. 1987, Particle acceleration at astrophysical shocks: A theory of cosmic ray origin, Phys. Rep., 154, 1

Blandford, R. D. & Rees, M. J. 1974, A 'twin-exhaust' model for double radio sources, MNRAS, 169, 395

Blasi, P. 2013, The origin of galactic cosmic rays, A&A Rev., 21, 70

Blumenthal, G. R. 1970, Energy Loss of High-Energy Cosmic Rays in Pair-Producing Collisions with Ambient Photons, Phys. Rev. D, 1, 1596

Blumenthal, G. R. & Gould, R. J. 1970, Bremsstrahlung, Synchrotron Radiation, and Compton Scattering of High-Energy Electrons Traversing Dilute Gases, Reviews of Modern Physics, 42, 237

Borkowski, K. J., Reynolds, S. P., Green, D. A., et al. 2010, Radioactive Scandium in the Youngest Galactic Supernova Remnant G1.9+0.3, ApJ, 724, L161

Britzen, S., Fendt, C., Eckart, A., & Karas, V. 2017, A new view on the M 87 jet origin: Turbulent loading leading to large-scale episodic wiggling, A&A, 601, A52

Burns, J. O., Feigelson, E. D., & Schreier, E. J. 1983, The inner radio structure of Centaurus A - Clues to the origin of the jet X-ray emission, ApJ, 273, 128

Cappellari, M., Neumayer, N., Reunanen, J., et al. 2009, The mass of the black hole in Centaurus A from SINFONI AO-assisted integral-field observations of stellar kinematics, MNRAS, 394, 660

Cash, W. 1979, Parameter estimation in astronomy through application of the likelihood ratio, ApJ, 228, 939

Combi, J. A. & Romero, G. E. 1997, The large-scale radio spectral index distribution of Centaurus A, A&AS, 121

Compiègne, M., Verstraete, L., Jones, A., et al. 2011, The global dust SED: tracing the nature and evolution of dust with DustEM, A&A, 525, A103

Crocker, R. M., Bicknell, G. V., Carretti, E., Hill, A. S., & Sutherland, R. S. 2014, Steady-state Hadronic Gamma-Ray Emission from 100-Myr-Old Fermi Bubbles, ApJ, 791, L20

Dainotti, M. G., Ostrowski, M., Harris, D., Siemiginowska, A., & Siejkowski, H. 2012, A cosmic ray cocoon along the X-ray jet of M87?, MNRAS, 426, 218

Davis, J. E. 2001, Event Pileup in Charge-coupled Devices, ApJ, 562, 575

de Gasperin, F., Orrú, E., Murgia, M., et al. 2012, M 87 at metre wavelengths: the LOFAR picture, A&A, 547, A56

de Gouveia Dal Pino, E. M. 2005, Astrophysical jets and outflows, Advances in Space Research, 35, 908

Di Matteo, T., Allen, S. W., Fabian, A. C., Wilson, A. S., & Young, A. J. 2003, Accretion onto the Supermassive Black Hole in M87, ApJ, 582, 133

Doeleman, S. S., Fish, V. L., Schenck, D. E., et al. 2012, Jet-Launching Structure Resolved Near the Supermassive Black Hole in M87, Science, 338, 355

Draine, B. T. 2003, Interstellar Dust Grains, ARA&A, 41, 241

Draine, B. T. & Li, A. 2007, Infrared Emission from Interstellar Dust. IV. The Silicate-Graphite-PAH Model in the Post-Spitzer Era, ApJ, 657, 810

Drury, L. O., Ellison, D. E., Aharonian, F. A., et al. 2001, Test of galactic cosmic-ray source models - Working Group Report, Space Sci. Rev., 99, 329

Eilek, J. A. 2014, The dynamic age of Centaurus A, New Journal of Physics, 16, 045001

Feng, J. & Wu, Q. 2017, Constraint on the black-hole spin of M87 from the accretion-jet model, ArXiv e-prints [[arXiv]1705.07804]

Fermi, E. 1949, On the Origin of the Cosmic Radiation, Physical Review, 75, 1169

Fixsen, D. J. 2009, The Temperature of the Cosmic Microwave Background, ApJ, 707, 916

Fleishman, G. D. 2006, Diffusive synchrotron radiation from extragalactic jets, MNRAS, 365, L11

Foreman-Mackey, D., Hogg, D. W., Lang, D., & Goodman, J. 2013, emcee: The MCMC Hammer, PASP, 125, 306

Franceschini, A., Rodighiero, G., & Vaccari, M. 2008, Extragalactic optical-infrared background radiation, its time evolution and the cosmic photon-photon opacity, A&A, 487, 837

Fritz, K. D. 1989, Synchrotron emission spectra from shockwaves in active galactic nuclei - an energy and space dependent diffusion coefficient, A&A, 214, 14

Gebhardt, K., Adams, J., Richstone, D., et al. 2011, The Black Hole Mass in M87 from Gemini/NIFS Adaptive Optics Observations, ApJ, 729, 119

Geddes, J., Quinn, T. C., & Wald, R. M. 1996, On the Injection Energy Distribution of Ultra–High-Energy Cosmic Rays, ApJ, 459, 384

Georganopoulos, M., Meyer, E., & Perlman, E. 2016, Recent Progress in Understanding the Large Scale Jets of Powerful Quasars, Galaxies, 4, 65

Giroletti, M., Hada, K., Giovannini, G., et al. 2012, The kinematic of HST-1 in the jet of M 87, A&A, 538, L10

Górski, K. M., Hivon, E., Banday, A. J., et al. 2005, HEALPix: A Framework for High-Resolution Discretization and Fast Analysis of Data Distributed on the Sphere, ApJ, 622, 759

Green, D. A., Reynolds, S. P., Borkowski, K. J., et al. 2008, The radio expansion and brightening of the very young supernova remnant G1.9+0.3, MNRAS, 387, L54

Hada, K., Kino, M., Doi, A., et al. 2016, High-sensitivity 86 GHz (3.5 mm) VLBI Observations of M87: Deep Imaging of the Jet Base at a Resolution of 10 Schwarzschild Radii, ApJ, 817, 131

Halzen, F. & Hooper, D. 2002, High-energy neutrino astronomy: the cosmic ray connection, Reports on Progress in Physics, 65, 1025

Hardcastle, M. J., Cheung, C. C., Feain, I. J., & Stawarz, Ł. 2009, High-energy particle acceleration and production of ultra-high-energy cosmic rays in the giant lobes of Centaurus A, MNRAS, 393, 1041

Harris, D. E., Biretta, J. A., Junor, W., et al. 2003, Flaring X-Ray Emission from HST-1, a Knot in the M87 Jet, ApJ, 586, L41

Harris, D. E., Cheung, C. C., Stawarz, Ł., Biretta, J. A., & Perlman, E. S. 2009, Variability Timescales in the M87 Jet: Signatures of E^2 Losses, Discovery of a Quasi Period in HST-1, and the Site of TeV Flaring, ApJ, 699, 305

Harris, D. E. & Krawczynski, H. 2002, X-Ray Emission Processes in Radio Jets, ApJ, 565, 244

Harris, D. E. & Krawczynski, H. 2006, X-Ray Emission from Extragalactic Jets, ARA&A, 44, 463

Harris, D. E., Massaro, F., Cheung, C. C., et al. 2011, An Experiment to Locate the Site of TeV Flaring in M87, ApJ, 743, 177

Harris, G. L. H., Rejkuba, M., & Harris, W. E. 2010, The Distance to NGC 5128 (Centaurus A), PASA, 27, 457

Harrison, F. A., Craig, W. W., Christensen, F. E., et al. 2013, The Nuclear Spectroscopic Telescope Array (NuSTAR) High-energy X-Ray Mission, ApJ, 770, 103

Haslam, C. G. T., Salter, C. J., Stoffel, H., & Wilson, W. E. 1982, A 408 MHz all-sky continuum survey. II - The atlas of contour maps, A&AS, 47, 1

Heinz, S. & Begelman, M. C. 1997, Analysis of the Synchrotron Emission from

the M87 Jet, ApJ, 490, 653
Heitler, W. 1954, Quantum theory of radiation
H.E.S.S. Collaboration, Abramowski, A., Aharonian, F., et al. 2014, TeV γ-ray observations of the young synchrotron-dominated SNRs G1.9+0.3 and G330.2+1.0 with H.E.S.S., MNRAS, 441, 790
Hillas, A. M. 2013, Evolution of ground-based gamma-ray astronomy from the early days to the Cherenkov Telescope Arrays, Astroparticle Physics, 43, 19
Inoue, T., Yamazaki, R., Inutsuka, S.-i., & Fukui, Y. 2012, Toward Understanding the Cosmic-Ray Acceleration at Young Supernova Remnants Interacting with Interstellar Clouds: Possible Applications to RX J1713.7-3946, ApJ, 744, 71
Israel, F. P. 1998, Centaurus A - NGC 5128, A&A Rev., 8, 237
Ivanenko, D. D. 1968, The structure of matter and attempts to create a unified theory of matter, ed. V. V. Fedynskii, 21
Jones, F. C. 1968, Calculated Spectrum of Inverse-Compton-Scattered Photons, Physical Review, 167, 1159
Jordán, A., Côté, P., Blakeslee, J. P., et al. 2005, The ACS Virgo Cluster Survey. X. Half-Light Radii of Globular Clusters in Early-Type Galaxies: Environmental Dependencies and a Standard Ruler for Distance Estimation, ApJ, 634, 1002
Kafexhiu, E., Aharonian, F., Taylor, A. M., & Vila, G. S. 2014, Parametrization of gamma-ray production cross sections for p p interactions in a broad proton energy range from the kinematic threshold to PeV energies, Phys. Rev. D, 90, 123014
Karakula, S. & Tkaczyk, W. 1993, The formation of the cosmic ray energy spectrum by a photon field, Astroparticle Physics, 1, 229
Khangulyan, D., Aharonian, F. A., & Kelner, S. R. 2014, Simple Analytical Approximations for Treatment of Inverse Compton Scattering of Relativistic Electrons in the Blackbody Radiation Field, ApJ, 783, 100
Kroon, J. J., Becker, P. A., Finke, J. D., & Dermer, C. D. 2016, Electron Acceleration in Pulsar-wind Termination Shocks: An Application to the Crab Nebula Gamma-Ray Flares, ApJ, 833, 157
Lagage, P. O. & Cesarsky, C. J. 1983, The maximum energy of cosmic rays accelerated by supernova shocks, A&A, 125, 249
Lamarre, J.-M., Puget, J.-L., Ade, P. A. R., et al. 2010, Planck pre-launch status: The HFI instrument, from specification to actual performance, A&A, 520, A9
Levinson, A. & Globus, N. 2017, Reconfinement of highly magnetized jets: implications for HST-1 in M87, MNRAS, 465, 1608
Liu, R.-Y., Rieger, F. M., & Aharonian, F. A. 2017, Particle Acceleration in Mildly

Relativistic Shearing Flows: The Interplay of Systematic and Stochastic Effects, and the Origin of the Extended High-energy Emission in AGN Jets, ApJ, 842, 39

Liu, S., Petrosian, V., Melia, F., & Fryer, C. L. 2006, A Testable Stochastic Acceleration Model for Flares in Sagittarius A*, ApJ, 648, 1020

Liu, W.-P. & Shen, Z.-Q. 2007, A Modified Synchrotron Model for Knots in the M87 Jet, ApJ, 668, L23

Macchetto, F., Marconi, A., Axon, D. J., et al. 1997, The Supermassive Black Hole of M87 and the Kinematics of Its Associated Gaseous Disk, ApJ, 489, 579

Malkov, M. A. & Drury, L. O. 2001, Nonlinear theory of diffusive acceleration of particles by shock waves, Reports on Progress in Physics, 64, 429

Mandolesi, N., Bersanelli, M., Butler, R. C., et al. 2010, Planck pre-launch status: The Planck-LFI programme, A&A, 520, A3

Marshall, H. L., Miller, B. P., Davis, D. S., et al. 2002, A High-Resolution X-Ray Image of the Jet in M87, ApJ, 564, 683

Massaro, E., Perri, M., Giommi, P., & Nesci, R. 2004, Log-parabolic spectra and particle acceleration in the BL Lac object Mkn 421: Spectral analysis of the complete BeppoSAX wide band X-ray data set, A&A, 413, 489

Mattox, J. R., Bertsch, D. L., Chiang, J., et al. 1996, The Likelihood Analysis of EGRET Data, ApJ, 461, 396

McKinley, B., Briggs, F., Gaensler, B. M., et al. 2013, The giant lobes of Centaurus A observed at 118 MHz with the Murchison Widefield Array, MNRAS, 436, 1286

McKinley, B., Yang, R., López-Caniego, M., et al. 2015, Modelling of the spectral energy distribution of Fornax A: leptonic and hadronic production of high-energy emission from the radio lobes, MNRAS, 446, 3478

Meisenheimer, K., Roeser, H.-J., & Schloetelburg, M. 1996, The synchrotron spectrum of the jet in M87., A&A, 307, 61

Mennella, A., Bersanelli, M., Butler, R. C., et al. 2011, Planck early results. III. First assessment of the Low Frequency Instrument in-flight performance, A&A, 536, A3

Mertens, F., Lobanov, A. P., Walker, R. C., & Hardee, P. E. 2016, Kinematics of the jet in M 87 on scales of 100-1000 Schwarzschild radii, A&A, 595, A54

Meyer, E. T., Sparks, W. B., Biretta, J. A., et al. 2013, Optical Proper Motion Measurements of the M87 Jet: New Results from the Hubble Space Telescope, ApJ, 774, L21

Mościbrodzka, M., Falcke, H., & Shiokawa, H. 2016, General relativistic magnetohydrodynamical simulations of the jet in M 87, A&A, 586, A38

Murphy, R. J., Dermer, C. D., & Ramaty, R. 1987, High-energy processes in solar flares, ApJS, 63, 721

Nishimura, J. 1969, in Planetary Electrodynamics, Volume 2, ed. S. C. Coroniti & J. Hughes, 333

Osone, S. 2017, Study of an interaction between the jet and an interstellar medium of M87 by using Chandra, ArXiv e-prints [[arXiv]1706.00683]

Ostrowski, M. 2000, On possible 'cosmic ray cocoons' of relativistic jets, MNRAS, 312, 579

O'Sullivan, S. P., Feain, I. J., McClure-Griffiths, N. M., et al. 2013, Thermal Plasma in the Giant Lobes of the Radio Galaxy Centaurus A, ApJ, 764, 162

Pavlov, G. G., Teter, M. A., Kargaltsev, O., & Sanwal, D. 2003, The Variable Jet of the Vela Pulsar, ApJ, 591, 1157

Perlman, E. S., Adams, S. C., Cara, M., et al. 2011, Optical Polarization and Spectral Variability in the M87 Jet, ApJ, 743, 119

Perlman, E. S., Biretta, J. A., Sparks, W. B., Macchetto, F. D., & Leahy, J. P. 2001, The Optical-Near-Infrared Spectrum of the M87 Jet fromHubble Space Telescope Observations, ApJ, 551, 206

Perlman, E. S., Biretta, J. A., Zhou, F., Sparks, W. B., & Macchetto, F. D. 1999, Optical and Radio Polarimetry of the M87 Jet at 0.2" Resolution, AJ, 117, 2185

Perlman, E. S., Harris, D. E., Biretta, J. A., Sparks, W. B., & Macchetto, F. D. 2003, Month-Timescale Optical Variability in the M87 Jet, ApJ, 599, L65

Perlman, E. S. & Wilson, A. S. 2005, The X-Ray Emissions from the M87 Jet: Diagnostics and Physical Interpretation, ApJ, 627, 140

Piran, T. 2000, Gamma-ray bursts - a puzzle being resolved, Phys. Rep., 333, 529

Planck Collaboration, Abergel, A., Ade, P. A. R., et al. 2014a, Planck 2013 results. XI. All-sky model of thermal dust emission, A&A, 571, A11

Planck Collaboration, Adam, R., Ade, P. A. R., et al. 2016a, Planck 2015 results. I. Overview of products and scientific results, A&A, 594, A1

Planck Collaboration, Adam, R., Ade, P. A. R., et al. 2016b, Planck 2015 results. X. Diffuse component separation: Foreground maps, A&A, 594, A10

Planck Collaboration, Adam, R., Ade, P. A. R., et al. 2016c, Planck 2015 results. IX. Diffuse component separation: CMB maps, A&A, 594, A9

Planck Collaboration, Ade, P. A. R., Aghanim, N., et al. 2014b, Planck 2013 results. I. Overview of products and scientific results, A&A, 571, A1

Planck Collaboration, Ade, P. A. R., Aghanim, N., et al. 2011a, Planck early results. I. The Planck mission, A&A, 536, A1

Planck Collaboration, Ade, P. A. R., Aghanim, N., et al. 2011b, Planck early results. II. The thermal performance of Planck, A&A, 536, A2

Planck Collaboration, Arnaud, M., Ashdown, M., et al. 2016d, Planck intermediate results. XXXI. Microwave survey of Galactic supernova remnants, A&A, 586, A134

Planck HFI Core Team, Ade, P. A. R., Aghanim, N., et al. 2011, Planck early results. IV. First assessment of the High Frequency Instrument in-flight performance, A&A, 536, A4

Plyasheshnikov, A. V. & Aharonian, F. A. 2002, Characteristics of air showers produced by extremely high energy gamma-rays, Journal of Physics G Nuclear Physics, 28, 267

Pogge, R. W. 1997, in Astronomical Society of the Pacific Conference Series, Vol. 113, IAU Colloq. 159: Emission Lines in Active Galaxies: New Methods and Techniques, ed. B. M. Peterson, F.-Z. Cheng, & A. S. Wilson, 378

Reynolds, C. S., Di Matteo, T., Fabian, A. C., Hwang, U., & Canizares, C. R. 1996, The 'quiescent' black hole in M87, MNRAS, 283, L111

Reynolds, S. P. 2008, Supernova Remnants at High Energy, ARA&A, 46, 89

Reynolds, S. P., Borkowski, K. J., Green, D. A., et al. 2008, The Youngest Galactic Supernova Remnant: G1.9+0.3, ApJ, 680, L41

Reynolds, S. P., Borkowski, K. J., Green, D. A., et al. 2009, X-Ray Spectral Variations in the Youngest Galactic Supernova Remnant G1.9+0.3, ApJ, 695, L149

Rieger, F. M. & Aharonian, F. 2012, Probing the Central Black Hole in M87 with Gamma-Rays, Modern Physics Letters A, 27, 1230030

Rieger, F. M., Bosch-Ramon, V., & Duffy, P. 2007, Fermi acceleration in astrophysical jets, Ap&SS, 309, 119

Rieger, F. M. & Mannheim, K. 2002, Particle acceleration in rotating and shearing jets from AGN, A&A, 396, 833

Rossi, B. & Greisen, K. 1941, Cosmic-Ray Theory, Reviews of Modern Physics, 13, 240

Russell, H. R., Fabian, A. C., McNamara, B. R., & Broderick, A. E. 2015, Inside the Bondi radius of M87, MNRAS, 451, 588

Rybicki, G. B. & Lightman, A. P. 1979, Book-Review - Radiative Processes in Astrophysics, Astronomy Quarterly, 3, 199

Rybicki, G. B. & Lightman, A. P. 1986, Radiative Processes in Astrophysics, 400

Ryder, L. H. 1996, Quantum Field Theory, 507

Sahayanathan, S. 2008, A two-zone synchrotron model for the knots in the M87 jet, MNRAS, 388, L49

Schure, K. M. & Bell, A. R. 2013, Cosmic ray acceleration in young supernova remnants, MNRAS, 435, 1174

Shain, C. A. 1958, Tha radio emission fron Centaurus A and Fornax A., Australian Journal of Physics, 11

Sparks, W. B., Biretta, J. A., & Macchetto, F. 1996, The Jet of M87 at Tenth-Arcsecond Resolution: Optical, Ultraviolet, and Radio Observations, ApJ, 473, 254

Stecker, F. W. 1998, On the Origin of the Highest Energy Cosmic Rays, Physical Review Letters, 80, 1816

Stecker, F. W., Baring, M. G., & Summerlin, E. J. 2007, Blazar γ-Rays, Shock Acceleration, and the Extragalactic Background Light, ApJ, 667, L29

Stefan, I. I., Carilli, C. L., Green, D. A., et al. 2013, Imaging on PAPER: Centaurus A at 148 MHz, MNRAS, 432, 1285

Sturrock, P. A. 1971, A Model of Pulsars, ApJ, 164, 529

Su, M., Slatyer, T. R., & Finkbeiner, D. P. 2010, Giant Gamma-ray Bubbles from Fermi-LAT: Active Galactic Nucleus Activity or Bipolar Galactic Wind?, ApJ, 724, 1044

Tanaka, T., Uchiyama, Y., Aharonian, F. A., et al. 2008, Study of Nonthermal Emission from SNR RX J1713.7-3946 with Suzaku, ApJ, 685, 988

Tauber, J. A., Mandolesi, N., Puget, J.-L., et al. 2010, Planck pre-launch status: The Planck mission, A&A, 520, A1

Tramacere, A., Massaro, F., & Cavaliere, A. 2007, Signatures of synchrotron emission and of electron acceleration in the X-ray spectra of Mrk 421, A&A, 466, 521

Uchiyama, Y., Aharonian, F. A., Tanaka, T., Takahashi, T., & Maeda, Y. 2007, Extremely fast acceleration of cosmic rays in a supernova remnant, Nature, 449, 576

Vink, J. 2006, in ESA Special Publication, Vol. 604, The X-ray Universe 2005, ed. A. Wilson, 319

Walsh, J. L., Barth, A. J., Ho, L. C., & Sarzi, M. 2013, The M87 Black Hole Mass from Gas-dynamical Models of Space Telescope Imaging Spectrograph Observations, ApJ, 770, 86

Waters, C. Z. & Zepf, S. E. 2005, Ultraviolet Hubble Space Telescope Observations of the Jet in M87, ApJ, 624, 656

Waxman, E. 1995, Cosmological Origin for Cosmic Rays above 10 19 eV, ApJ, 452, L1

Webb, G. M., Axford, W. I., & Forman, M. A. 1985, Cosmic-ray acceleration at stellar wind terminal shocks, ApJ, 298, 684

Weisskopf, M. C., Brinkman, B., Canizares, C., et al. 2002, An Overview of the Performance and Scientific Results from the Chandra X-Ray Observatory, PASP, 114, 1

Weisskopf, M. C., Hester, J. J., Tennant, A. F., et al. 2000a, Discovery of Spatial and Spectral Structure in the X-Ray Emission from the Crab Nebula, ApJ, 536, L81

Weisskopf, M. C., Tananbaum, H. D., Van Speybroeck, L. P., & O'Dell, S. L. 2000b, in Proc. SPIE, Vol. 4012, X-Ray Optics, Instruments, and Missions III, ed. J. E. Truemper & B. Aschenbach, 2–16

Wik, D. R., Hornstrup, A., Molendi, S., et al. 2014, NuSTAR Observations of

the Bullet Cluster: Constraints on Inverse Compton Emission, ApJ, 792, 48
Wilson, A. S. & Yang, Y. 2002, Chandra X-Ray Imaging and Spectroscopy of the M87 Jet and Nucleus, ApJ, 568, 133
Wilson, A. S. & Yang, Y. 2004, Addendum: "Chandra X-Ray Imaging and Spectroscopy of the M87 Jet and Nucleus" (<A href="/abs/2002ApJ...568..133W">ApJ, 568, 133 [2002]</A>), ApJ, 610, 624
Wykes, S., Croston, J. H., Hardcastle, M. J., et al. 2013, Mass entrainment and turbulence-driven acceleration of ultra-high energy cosmic rays in Centaurus A, A&A, 558, A19
Wykes, S., Intema, H. T., Hardcastle, M. J., et al. 2014, Filaments in the southern giant lobe of Centaurus A: constraints on nature and origin from modelling and GMRT observations, MNRAS, 442, 2867
Yang, R.-z., Aharonian, F., & Crocker, R. 2014, The Fermi bubbles revisited, A&A, 567, A19
Yang, R.-Z., Sahakyan, N., de Ona Wilhelmi, E., Aharonian, F., & Rieger, F. 2012, Deep observation of the giant radio lobes of Centaurus A with the Fermi Large Area Telescope, A&A, 542, A19
Yuan, F. & Narayan, R. 2014, Hot Accretion Flows Around Black Holes, ARA&A, 52, 529
Zabalza, V. 2015, naima: a Python package for inference of relativistic particle energy distributions from observed nonthermal spectra, Proc. of International Cosmic Ray Conference 2015, in press
Zacchei, A., Maino, D., Baccigalupi, C., et al. 2011, Planck early results. V. The Low Frequency Instrument data processing, A&A, 536, A5
Zhang, J., Bai, J. M., Chen, L., & Liang, E. 2010, X-Ray Radiation Mechanisms and Beaming Effect of Hot Spots and Knots in Active Galactic Nuclear Jets, ApJ, 710, 1017
Zirakashvili, V. N. & Aharonian, F. 2007, Analytical solutions for energy spectra of electrons accelerated by nonrelativistic shock-waves in shell type supernova remnants, A&A, 465, 695
Zirakashvili, V. N. & Aharonian, F. A. 2010, Nonthermal Radiation of Young Supernova Remnants: The Case of RX J1713.7-3946, ApJ, 708, 965
Zirakashvili, V. N., Aharonian, F. A., Yang, R., Oña-Wilhelmi, E., & Tuffs, R. J. 2014, Nonthermal Radiation of Young Supernova Remnants: The Case of CAS A, ApJ, 785, 130
Zoglauer, A., Reynolds, S. P., An, H., et al. 2015, The Hard X-Ray View of the Young Supernova Remnant G1.9+0.3, ApJ, 798, 98
Zweibel, E. G. & Yamada, M. 2009, Magnetic Reconnection in Astrophysical and Laboratory Plasmas, ARA&A, 47, 291

A

Thermodynamic Temperature and MJy/sr to Jy/pix

We need to convert the *Planck* image to Jy/pix from the original units thermodynamic temperature T_thermo and MJy/sr. We will use the following physical constants:
$h = 6.62607004 \times 10^{-34}$ J $*$ s, the Plank's constant;
$k = 1.38064852 \times 10^{-23}$ J/K, the Boltzmann's constant;
$c = 2.99792458 \times 10^{8}$ m/s, the velocity of light;
$T_{\text{CMB}} = 2.7255$ K, the temperature of the CMB.

Blackbody radiation is the radiative field inside a cavity in thermodynamic equilibrium. Brightness temperature, T is defined as the temperature of a blackbody that emits the same radiance as measured. So for a blackbody, the brightness temperature T equals to thermodynamic (kinetic) temperature T_thermo. The spectral radiance emitted by a blackbody with a given temperature is expressed by the Planck function:

$$B(\nu) = \frac{2h\nu^3}{c^2}\left(\exp\left(\frac{h\nu}{kT}\right) - 1\right)^{-1} \tag{A.1}$$

Antenna temperature (T_A) is a parameter that describes how much noise an antenna produces in a given environment. For an antenna with a radiation blackbody pattern, the antenna temperature (T_A) is defined as:

$$T_A = \frac{1}{2k}\left(\frac{c}{\nu}\right)^2 B(\nu) \tag{A.2}$$

Differentiate it with respect to temperature:

$$\delta T_A = \frac{c^2}{(2k\nu^2)}\frac{dB_\nu}{dT} = \frac{(x^2e^x)}{(e^x-1)^2}\delta T \tag{A.3}$$

where $x = h\nu/kT = 1.7605556 \times 10^{-11} \times \nu$, ν is in unit of Hz. Therefore the conversion factor from T_thermo to T_A is

$$f = \frac{(x^2e^x)}{(e^x-1)^2} \tag{A.4}$$

The brightness of the source $B(\nu)$ is in unit of $\mathrm{W/sr/m^2/Hz} = 10^{20}$ MJy/sr, through Equation A.1, we can get the conversion factor from T_A to MJy/sr

$$f_1 = 0.03072387 \times \left(\frac{\nu}{10^9}\right)^2 \tag{A.5}$$

So the conversion factor from T_thermo to MJy/sr is

$$f_2 = f \times f_1 \tag{A.6}$$

We assume the size of the pixels in our image is x degrees per pixel, then the size in square degrees per pixel is

$$x\frac{\mathrm{deg}}{\mathrm{pix}} \times x\frac{\mathrm{deg}}{\mathrm{pix}} = x^2 \frac{\text{square deg}}{\text{(square) pix}} \tag{A.7}$$

1 square deg $= 3.0461184 \times 10^{-4}$ sr, so the size of the pixel in steradian is

$$x^2 \frac{\text{square deg}}{\text{(square) pix}} \times 3.0461184 \times 10^{-4} \frac{\mathrm{sr}}{\text{square deg}} = 3.0461184 \times 10^{-4} x^2 \frac{\mathrm{sr}}{\mathrm{pix}} \tag{A.8}$$

$$\frac{\mathrm{MJy}}{\mathrm{sr}} \times 3.0461184 \times 10^{-4} x^2 \frac{\mathrm{sr}}{\mathrm{pix}} = 304.61184 x^2 \frac{\mathrm{Jy}}{\mathrm{pix}} \tag{A.9}$$

So the conversion factor from $\frac{\mathrm{MJy}}{\mathrm{sr}}$ to $\frac{\mathrm{Jy}}{\mathrm{pix}}$ is

$$f_3 = 304.61184 \times x^2 \tag{A.10}$$

and the conversion factor from T_thermo to $\frac{\mathrm{Jy}}{\mathrm{pix}}$ is

$$f_4 = f_2 \times f_3 \tag{A.11}$$

β_e and β Relation

B

The cutoff region in the distribution of parent electrons $F(E)$ has a shape similar to the synchrotron spectrum given by Eq.(4.2), $F(E) \propto \exp[-(E/E_0)^{\beta_e}]$ with the following simple relation between β_e and β (Fritz, 1989):

$$\beta = \frac{\beta_e}{2+\beta_e} \,. \tag{B.1}$$

Thus the cutoff region in the spectrum of synchrotron radiation is much smoother than the cutoff region of the spectrum of parent electrons. For any electron distribution, the synchrotron cutoff cannot be sharper than the simple exponential decline ($\beta = 1$), which can only be witnessed in the case of an abrupt cutoff in the spectrum of parent electrons ($\beta_e \to \infty$). In the case of a simple exponential cutoff in the electron spectrum ($\beta_e = 1$), the corresponding synchrotron cutoff region is very shallow with $\beta = 1/3$. Formally, such spectra can be formed during the shock acceleration of electrons in the Bohm diffusion regime when the maximum energy of electrons is determined by the age of the source rather than by energy losses of electrons. However, in the particular case of young SNRs, when the electrons are accelerated up to 100 TeV and beyond (otherwise one cannot explain the observed X-ray data), with any reasonable set of parameters (magnetic field, age of the source, shock speed, *etc.*), the acceleration proceeds in the electron energy-loss regime, and the maximum energy is determined from the competition between the acceleration and energy loss rates. In this case, the spectrum of electrons exhibits a super exponential cutoff, namely $\beta_e = 2$ (Zirakashvili & Aharonian, 2007). Correspondingly, the synchrotron spectrum contains, in accordance with Eq.(4.3), a cutoff with $\beta = 1/2$.

The δ-functional approximation gives an incorrect relation between β_e and β, namely $\beta = \beta_e/2$. For example, within this approximation, the cutoff in the spectrum of synchrotron radiation with $\beta = 1$ can be interpreted as a result of the cutoff in the electron spectrum with $\beta_e = 2$. However, in reality,

such a synchrotron spectrum can be formed, in accordance with Eq.(4.2), in the case of an abrupt cutoff in the electron spectrum, that is, for $\beta_e \to \infty$.

C Asymptotic Forms of the Electron Spectra in the Bohm Diffusion Regime

Asymptotic spectra of electrons

The asymptotic spectra of shock-accelerated electrons in the Bohm diffusion regime are derived by Zirakashvili & Aharonian (2007) under the assumption that the energy losses of electrons are dominated by synchrotron radiation. The spectrum of the electrons in the high energy cut-off region has a "Gaussian" type behavior, $N_0 \propto \exp(-E^2/E_0^2)$, where

$$E_0 = \frac{2.86\times10^8 m_e c^2}{\gamma_s \eta^{1/2}(1+\kappa^{1/2})}\left(\frac{u_1}{3000\ \mathrm{km\ s^{-1}}}\right)\left(\frac{B}{100\,\mu\mathrm{G}}\right)^{-1/2} \tag{C.1}$$

In the case of standard shock acceleration in the Bohm diffusion regime, $\gamma_s = 4$. u_1 is the shock speed in the upstream. The factor $\eta \geq 1$ which is proportional to diffusion coefficient, in the case of Bohm diffusion $\eta = 1$. $\kappa = B_1/B_2$ is the ratio of the magnetic field upstream to the magnetic field downstream, for the young supernova remnants, the magnetic field downstream is stronger than magnetic field upstream, we use a practical number $\kappa = \frac{1}{\sqrt{11}}$. The analytical approximation for the electron distributions in the upstream region:

$$\mathrm{E}^2\frac{\mathrm{dN_1}}{\mathrm{dE}} = 0.7 l E E_0^3\left[1+1.7\left(\frac{E}{E_0}\right)^3\right]^{5/6}\exp\left(-\frac{E^2}{E_0^2}\right) \tag{C.2}$$

For the downstream, the integrated energy spectrum of electrons is

$$\mathrm{E}^2\frac{\mathrm{dN_2}}{\mathrm{dE}} = l E^{-1} E_0^5\left[1+0.523\left(\frac{E}{E_0}\right)^{\frac{9}{4}}\right]^2\exp\left(-\frac{E^2}{E_0^2}\right) - 0.09\times\mathrm{E}^2\frac{\mathrm{dN_1}}{\mathrm{dE}} \tag{C.3}$$

Here, l is just an adjustable parameter.

Synchrotron spectra

In the case of the above asymptotic electron distributions, the following spectra of synchrotron radiation produced by upstream and downstream regions is given:

$$J_1(\epsilon) \propto 0.58 \left[1 + 1.27 \left(\frac{\epsilon}{\epsilon_0}\right)^{3/4}\right]^{1/2} \exp\left(-\sqrt{3.32\frac{\epsilon}{\epsilon_0}}\right), \tag{C.4}$$

$$J_2(\epsilon) \propto \frac{\epsilon_0}{\epsilon}\left[1 + 0.38\sqrt{\frac{\epsilon}{\epsilon_0}}\right]^{11/4} \exp\left(-\sqrt{\frac{\epsilon}{\epsilon_0}}\right). \tag{C.5}$$

Where

$$\epsilon_0 = \frac{2.2\,\text{keV}}{\eta(1+\kappa^{1/2})^2}\left(\frac{u_1}{3000\,\text{km}\,s^{-1}}\right)^2 \frac{16}{\gamma_s^2}\,. \tag{C.6}$$

is the energy of synchrotron photons in the cut-off region.